UNIVERSITY OF CAPE TOWN
IYUNIVESITHI YASEKAPA • UNIVERSITEIT VAN KAAPSTAD

THE IMPACT OF THERMOPHYSICAL PROPERTIES ON NANOFLUID-BASED SOLAR COLLECTOR PERFORMANCE

By
GODFREY KABUNGO GAKINGO
GKNGOD001

SUPERVISOR: PROF. DAYA REDDY
CO-SUPERVISOR: DR. MICHELLE MACDEVETTE

A DISSERTATION SUBMITTED TO THE UNIVERSITY OF CAPE TOWN IN PARTIAL FULFILMENT OF THE REQUIREMENTS FOR THE DEGREE OF MASTER OF PHILOSOPHY IN MECHANICAL ENGINEERING

FEBRUARY 2016

Plagiarism declaration

I, GODFREY KABUNGO GAKINGO, hereby declare that the work on which this dissertation is based is my original work (except where acknowledgements indicate otherwise) and that neither the whole work nor any part of it has been, is being, or is to be submitted for another degree in this or any other university.

I authorise the University to reproduce for the purpose of research either the whole or any portion of the contents in any manner whatsoever.

Signature: Signed by candidate Date: 09/02/2016

Acknowledgements

All glory to God for His graces that have brought me thus far.

My deepest gratitude to Dr. Hussein Jama who set me on this journey and to the ARISE consortium for making the past 2 years possible via their funding. To the ARISE coordinators in the IAPO office, with particular mention of Ms Norma Derby, I thank you.

I would also like to extend my deepest gratitude to my supervisor, Prof. Daya Reddy, and my co-supervisor, Dr. Michelle MacDevette. I am grateful for your guidance and support throughout this project.

A big thank you to the CERECAM research group for providing a diverse, challenging and supportive research environment. Many thanks to Mrs Olivia Goodhind for ever being so welcoming, Dr. Andrew Mcbride for making C++ seem easy, Mr Mehdi Shirzadi for sushi and being a great deskmate, and the rest for scintillating lunchtime discussions.

I also acknowledge the support of friends and in particular the All Africa House fraternity that has provided a home away from home. To Mr Alfred Mitema, Mr Chris Zenim and Mr Vin Oderah, I'm glad to have counted you as friends, mentors and brothers.

Finally, to my family, I thank you for the endless support, good cheer and prayers. God bless you all.

Abstract

Nanofluids are a novel class of heat transfer fluids in which nanoparticles are dispersed in traditional heat transfer fluids. They offer enhanced thermophysical, rheological and radiative properties. These enhancements have resulted in recent research being centred on the application of nanofluids to various systems. An example of such systems is the solar volumetric flow receiver in which great efficiency improvements have been reported. To explain this efficiency increase, researchers have evaluated the impact of enhanced radiative properties of nanofluids while largely neglecting that of enhanced thermophysical properties.

This study looks at the impact of enhanced thermophysical properties on the performance of nanofluid-based solar volumetric receivers. Particular focus is drawn to the impact of temperature dependent conductivity and volumetric specific heat capacity. Copper oxide – water nanofluid is employed as its temperature dependent properties have been characterised. These are evaluated over a wavelength range $0.3 \leq \lambda \leq 1\,\mu m$ and a temperature range $308 \leq T < 380\,K$. The Schuster-Schwarzschild 2-flux approximation to the radiation transfer equation and a finite volume approximation to the energy and flow equations are employed to model the receiver.

The results obtained illustrate that temperature dependent conductivity impacts temperature development but not the receiver's efficiency. Measures observed for the former include the peak and the mean top wall temperatures as well as temperature gradients along the height of the receiver. It is seen that the presence of temperature dependent conductivity results in a decrease of the three measures due to greater diffusion of energy. The magnitude of this decrease is observed to be greater at higher concentrations ratios. For example, maximum drops in the peak and the mean top wall temperatures of $7.67\,K$ and $5.22\,K$ respectively are observed. These occur between cases with temperature independent versus temperature dependent conductivity at a concentration ratio of 150.

The impact of conductivity is also observed to depend on the choice of conductivity model. The use of two models; one conservative, and the other non-conservative, helps to establish a general trend in the observations reported. Minimal changes in the volumetric specific heat capacity occur ($\leq 3\%$). Consequently, there is insignificant impact on temperature development. The receiver's efficiency is, however, slightly impacted due to the presence of temperature linked density changes and subsequent flow acceleration. The efficiency is observed to decrease with increase in concentration ratio beyond an optimum point.

Table of contents

List of figures

List of tables

List of abbreviations

EE	Energy equation
NS	Navier-Stokes
RTE	Radiation transfer equation
RHS	Right hand side
LHS	Left hand side
LU	Lower Upper (matrix factorization)
SIMPLER	Semi-Implicit Method for Pressure Linked Equations – Revised
ODEs	Ordinary differential equations

List of symbols

Symbol	**Units (unless otherwise stated)**	**Description**
A	m^2	Collector's absorbing area
$\boldsymbol{A}$	–	Matrix of coefficients
C	–	Area concentration ratio
D	nm	Nanoparticle diameter
G	W/m^2	Incident solar flux
H	m	Height
I_λ	$W/(m^2\ \mu m\ sr)$	Spectral radiation flux
$I_{b,\lambda}$	$W/(m^2\ \mu m\ sr)$	Spectral blackbody emission flux
J_{DN}	W/m^2	Direct normal incident solar flux
$K_{a,\lambda}$	cm^{-1}	Spectral absorption coefficient
$K_{s,\lambda}$	cm^{-1}	Spectral scattering coefficient
$K_{e,\lambda}$	cm^{-1}	Spectral extinction coefficient
L	m	Length
$Q_{a,\lambda}$	–	Spectral absorption efficiency
$Q_{s,\lambda}$	–	Spectral scattering efficiency
$Q_{e,\lambda}$	–	Spectral extinction efficiency
T	K	Temperature
T_C	K	Sink temperature
T_H	K	Source temperature
$T_{in,\ out}$	K	Inlet/outlet temperature
$\overline{T}_{in,\ out}$	K	Mean Inlet/outlet temperature
T_{amb}	K	Ambient temperature
W	m	Width
c	m/s	Speed of light in medium
c_o	m/s	Speed of light in vacuum
c_p	J/(kg K)	Specific heat capacity
$\boldsymbol{f}$	–	Flux vector
h	$W/(m^2\ K)$	Convective heat loss coefficient
k	W/(m K)	Thermal conductivity
m	kg	Mass

$m = n + ik; i = \sqrt{-1}$	–	Complex refractive index
$\boldsymbol{m}$	–	Normalized complex refractive index
$\dot{m}$	kg/s	Mass flow rate
p	N/m^2	Pressure
$p_\lambda\left(\vec{\Omega}' \rightarrow \vec{\Omega}\right)$	–	Spectral phase function
q_r	W/m^2	Net radiative heat flux
$\frac{\partial q_r}{\partial y}$	W/m^3	Divergence of net radiative heat flux
$\boldsymbol{t}$	–	Variable vector
t_{exp}	s	Exposure time
$u/u(y)$	m/s	Velocity
α	–	Size parameter
ϵ	–	Emissivity
ϕ	–	Volume fraction
ρ	kg/m^3	Density
μ	kg/(m s)	Viscosity
$\mu = \cos\theta$	–	Directional cosine
$\tau = K_{e,\lambda} y$	–	Optical depth
$\tau(\mu)$	–	Glass transmissivity
λ	μm	Wavelength
η_{Carnot}	–	Carnot efficiency
$\eta_{collector}$	–	Collector efficiency
η_{system}	–	System efficiency

Subscripts/superscripts

nf	Nanofluid
bf	Basefluid
np	Nanoparticle

Chapter 1: Introduction

1.1 Background

The place of the sun as the primary source of the earth's energy has been known since the earliest days as evidenced by the early Egyptian civilization's sun worship (Kalogirou 2004). Furthermore, existing records indicate the intentional use of solar energy in the Greek era (Kalogirou 2004). Despite this knowledge, derived sources of energy such as oil and gas have continued to feature overwhelmingly in the earth's energy supply mix. This has been in part attributed to low efficiencies of solar harvesting technologies and limited storage capacity for the harvested energy (Lenert, Zuniga et al. 2010b).

With regards to solar harvesting, different technologies such as the solar thermal collectors (receivers/absorbers) have been proposed. These have been the outputs of research efforts that have been chronologically inconsistent with reactionary peaks such as that in the 1970s in response to the oil crisis (Kalogirou 2004). A current peak exists that is driven by environmental concerns (pollution and climate change) as well as the realisation of the exhaustibility of fossil fuels (Kalogirou 2004). As a result, a new frontier in solar thermal harvesting research has been opened in which this study situates itself.

Solar thermal collectors are based on either surface or volumetric absorption. In the former, a surface is employed to absorb incoming solar radiation energy and transfer it to a heat transfer fluid. In the latter, absorption occurs within the volume of the heat transfer fluid. Both processes lead to an increase in the internal energy of the fluid, seen as an increase in temperature, which can then be extracted as useful work in a heat engine.

Working backwards from the efficiency considerations of a heat engine and assigning it a Carnot efficiency (η_{Carnot}) defined as,

$$\eta_{Carnot} = 1 - \frac{T_C}{T_H}, \qquad (1.1)$$

it can be seen that greater efficiency is attained by an increase in the source temperature (T_H) for a given sink temperature (T_C). In a solar powered system, it is generally the case that the source temperature of the heat engine (T_H) will be given by the mean outlet temperature of the solar thermal collector ($\bar{T}_{out}$). The exception to this is when the heat transfer fluid undergoes some intervening process after exiting the collector and before entering the heat

engine. The sink temperature (T_C) will be the ambient temperature and is thus fixed. Consequently, higher efficiencies are obtained when the solar thermal collector is able to impart higher temperatures to the heat transfer fluid flowing through it.

The ability of a solar thermal collector to perform according to the needs set out above is quantified by the collector's efficiency ($\eta_{collector}$). This is defined as the ratio of energy absorbed by the heat transfer fluid within the collector to the total solar energy availed to the collector. It is given as,

$$\eta_{collector} = \frac{\dot{m}c_p(\bar{T}_{out} - \bar{T}_{in})}{ACG}, \tag{1.2}$$

where $\dot{m}$ is the fluid's mass flow rate and $c_p$is the fluid's specific heat capacity. $\bar{T}_{out}$ and $\bar{T}_{in}$ are respectively the fluid's mean outlet and inlet temperatures. ACG is the solar energy supplied which is a product of the absorbing area of the collector, A, the concentration ratio, C, and the incident solar radiation flux, G.

The collector's performance will depend on three main factors: the energy available, its ability to absorb and its ability to transfer the absorbed energy to the heat transfer fluid. Whereas the latter two factors are tackled differently by surface and volume collectors, the first is tackled by common strategies as illustrated in Table 1. These strategies are aimed at dealing with the diffuse nature of the solar resource and include motion tracking and concentration.

Table 1: Types of solar thermal collectors (Kalogirou 2004).

Motion	**Collector type**	**Absorber type**	**Concentration ratio**	**Indicative temperature range (°C)**
Stationary	Flat plate collector (FPC)	Flat	1	30 – 80
	Evacuated tube collector (ETC)	Flat	1	50 – 200
	Compound parabolic collector (CPC)	Tubular / Flat	1 – 5	60 – 240
	Compound parabolic collector (CPC)	Tubular / Flat	5 – 15	60 – 300

Single-axis tracking	Linear Fresnel reflector (LFR)	Tubular	10 – 40	60 – 250
	Parabolic trough collector (PTC)	Tubular	15 – 45	60 – 300
	Cylindrical trough collector (CTC)	Tubular	10 – 50	60 – 300
Two-axes tracking	Parabolic dish reflector (PDR)	Point	100 – 1000	100 – 500
	Heliostat field collector (HFC)	Point	100 – 1500	150 – 2000

Motion tracking employs a drive system to rotate the collector about either one axis or two axes. It is done to ensure that the collector's absorbing area is maintained in a direct line-of-sight with the sun throughout the day as it "travels across the sky". Consequently, the collector continuously receives the maximum amount of incident radiation flux throughout the day. Concentration of the incident flux is achieved by placing an optical device such as a reflector or refractor between the sun and the collector's absorbing area (Duffie, Beckman 2013). The area concentration ratio (C) is defined as the ratio of the optical device's aperture area to the collector's absorbing area (Duffie, Beckman 2013).

Considering surface absorbers, their ability to absorb is dictated by the surface's intrinsic properties: surface absorptivity, reflectivity and emissivity. Absorption surfaces are selected and treated to obtain high absorptivity in the short solar wavelength range and low emissivity in the long wavelength range (Duffie, Beckman 2013). This results in high absorption of the incident solar radiation and low thermal emission with the net being the absorbed energy (Duffie, Beckman 2013).

This absorbed energy results in an increase in internal energy translating to an initial development of higher temperatures at the surface as compared to those in the heat transfer fluid. This temperature gradient between the surface and the fluid drives heat transfer process to the fluid. The effectiveness of this process is, however, limited by the heat transfer characteristics of the fluid which are generally poor in comparison to those of solids. For example, water has a room temperature thermal conductivity of $0.613\ W/(m\ K)$ compared to silver with a conductivity of $429\ W/(m\ K)$ (Eastman, Phillpot et al. 2004).

A temperature gradient is also created with the ambient that drives thermal energy loss by radiation and convection. Energy loss is especially problematic in high temperature concentrating collectors. This is because radiation heat loss scales with the fourth power of surface temperature (Otanicar 2011a, Lenert, Wang 2012, Lenert 2010a).

Different solutions have been proposed to overcome these shortcomings of surface absorbers such as flow and geometry optimisation and the introduction of glazing to reduce surface emission losses (Thirugnanasambandam, Iniyan et al. 2010, Hunt 1978). Volumetric receivers, however, provide a paradigm shift in which “radiation is absorbed through a much longer path inside a volume rather than in a thin layer at the surface” (Zhu, Zhang 2012). This theoretically allows peak temperatures to form away from the surface resulting in lower heat loss. Figure 1 gives a conceptual illustration of such systems that would have either a fixed porous solid with gas flowing through it or a suspension of particles entrained in the motion of a gas or a liquid.

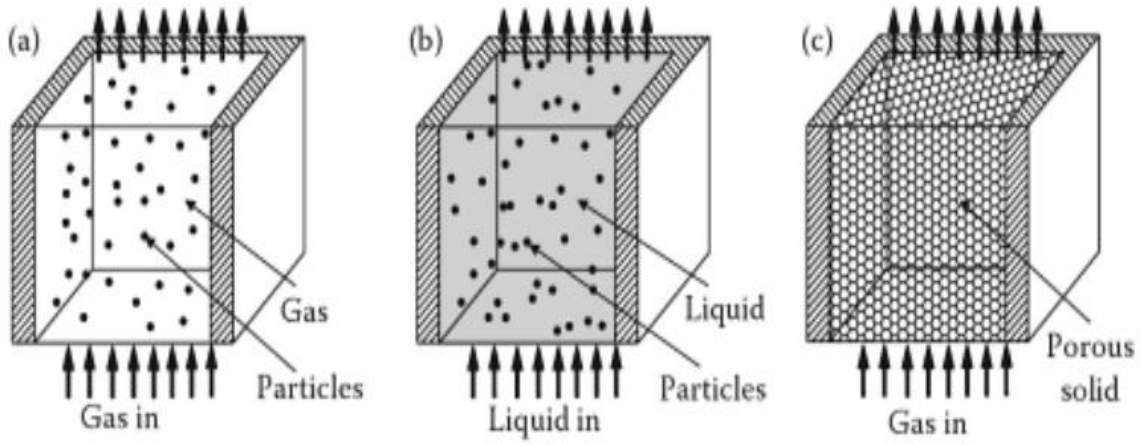

Figure 1: Volumetric receiver designs: particles suspended in gas (a), particles suspended in liquid (b) and porous solids (c) (Zhu, Zhang 2012).

In volumetric receivers, the absorbing areas (particles or porous solid in Figure 1) are located within the collector volume and peak temperatures may be set up away from the surface. This results in a reduction of surface thermal energy loss (Minardi, Chuang 1975). Furthermore, the heat transfer process to the fluid is enhanced by virtue of a greater total surface area for volumetric absorption which allows for greater contact between the fluid and the absorbing area (Minardi, Chuang 1975). The sum total of these is greater efficiency over surface collectors.

The use of particles suspended in a fluid offers an extra advantage over the use of a porous solid due to the larger surface area to volume ratio of the particles. This implies that thermal

equilibrium between the particles and the heat transfer fluid is attained almost instantaneously (Hunt 1978). The limit of such systems then becomes the size of the particles that can be achieved with the technology of the day. Thus, whereas in the 1970s – 1980s research was focused on the use of micro-sized particles (diameters, $D > 100\,nm$), current technology allows for the manufacture and use of nanoparticles ($1\,nm \leq D \leq 100\,nm$).

1.2 Problem statement

The use of nanoparticles in heat transfer fluids (alias nanofluids) and their application to solar thermal harvesting has opened a new field of research with initial results showing promise (Tyagi, Phelan et al. 2009). A review of literature illustrates that there have been few experimental studies. Most have been numerical in nature relying on available nanofluid property data. Consequently, two camps have emerged within the research community.

The first camp has focused on the enhancement of thermophysical properties of nanofluids (conductivity, density, specific heat capacity, etc.). Enhancements obtained have been applied to, for example, surface absorbers (Yousefi, Veisy et al. 2012b, Yousefi, Veysi et al. 2012, Tiwari, Ghosh et al. 2013, Faizal, Saidur et al. 2013) among other technologies. The second camp has focused on the radiative property enhancements in nanofluids, applying them to volumetric receivers (Javadi, Saidur et al. 2013, Mahian, Kianifar et al. 2013, Kasaeian, Eshghi et al. 2015, Verma, Tiwari 2015).

With regards to the performance of volumetric receivers, especially in high temperature applications, studies have largely failed to account for the impact of temperature dependent thermophysical property enhancements in nanofluids. This is despite earlier studies showing anomalous property enhancements such as a 40% enhancement of conductivity for copper – ethylene glycol nanofluids at volume fractions as low as 0.3% (Eastman, Choi et al. 2001). Given that only a single study (Khullar, Tyagi et al. 2013) has so far looked at the impact of temperature dependent thermophysical property enhancements, further investigation is required on this subject.

This study seeks to address this gap by initially identifying a nanofluid whose temperature dependent thermophysical properties have been modelled. The nanofluid is then employed in a numerical simulation of a 2D volumetric receiver with fixed geometry. Finally,

performance results obtained are compared with what has been previously reported in a bid to establish common trends or dissimilarities.

1.3 Justification

The need to understand temperature dependence of both thermophysical and radiative properties in nanofluid-based high flux receivers has been recognised by researchers. To this end, pioneering experimental work (Hordy, Rabilloud et al. 2014) has been conducted to investigate temperature dependence of radiative properties. Similar efforts are required to understand the impact of temperature dependent thermophysical property enhancements.

In the absence of experimental work, there exists earlier literature on thermophysical properties of nanofluids (Khanafer, Vafai 2011). This can be built upon to study the impact of these properties on the performance of volumetric receivers.

1.4 Objectives

The broad objective of this study is to deepen the understanding of the impact of temperature dependent thermophysical properties of nanofluids on the performance of solar volumetric receivers. This is tackled in terms of the following specifics:

- Identification of a sufficiently characterised nanofluid.
- A numerical study of the impact of temperature dependent thermal conductivity.
- A numerical study of the impact of temperature dependent volumetric specific heat capacity.
- A study of frequently cited design variables or parameters using temperature dependent properties to test previously reported trends.

1.5 Thesis overview

Chapter 1 introduces solar thermal harvesting and some of the technology employed including surface and volumetric collectors/receivers. It establishes the focus of this study which is on nanofluids-based volumetric receivers. Chapter 2 presents a chronological

development of volumetric receivers, an introduction to nanofluids as well as the current state of research in nanofluid-based receivers.

Property models for copper oxide – water nanofluid are presented in Chapter 3. In addition, the model of the volumetric receiver employed in the study is presented. Approximations to the volumetric receiver model as well as their implementation through the finite volume method are presented in Chapter 4. Chapter 5 provides the results of the study plus the ensuing discussion, followed by some concluding remarks in Chapter 6.

Chapter 2: Literature review

In this section, a chronological development of volumetric receivers is initially presented. This is followed by an introduction to nanofluids. Thereafter, the application of nanofluids to volumetric receivers is reviewed and a summary of the literature indicating the gaps in knowledge given. The summary also indicates how this study addresses these gaps.

2.1 Volumetric receivers

Volumetric receivers were proposed in the 1970s as an alternative to surface absorbers. They offered reduced heat loss as peak temperatures were located away from the surfaces. Additionally, there were fewer heat transfer steps from the sun's radiation energy to the fluid's internal energy (Minardi, Chuang 1975).

Minardi & Chuang (1975) published on the use of a black liquid flat plate solar collector in which solar radiation energy was absorbed directly by the liquid. Favourable performance was achieved in comparison to a conventional surface collector (Minardi, Chuang 1975). The black liquid employed, India ink, was a suspension of micro-sized carbonaceous particles in an ethylene glycol/water mixture (Zhu, Zhang 2012, Otanicar, Phelan et al. 2010a).

The use of a black ingredient or impurity in the basefluid was to improve its absorption in the solar spectrum. This was necessary as basefluids are generally transparent except in the infrared region of the solar spectrum which contains only about 15% of the solar energy (Lenert, Zuniga et al. 2010b, Sani, Dell'Oro 2014, Taylor, Phelan et al. 2011b, Otanicar, Phelan et al. 2009b). Hunt (1978) expected that the particles would retain the bulk absorption properties which were higher than those of the basefluid. Furthermore, it was expected that the particle's high surface area to volume ratio would ensure instantaneous heat transfer to the fluid (Hunt 1978).

This idea was then extended to solid-gas suspensions (Hunt 1978, Abdelrahman, Fumeaux et al. 1979). Air was employed as a non-absorbing heat transfer fluid thus allowing the study of the individual performance of particles. The results illustrated that particles could absorb solar radiation and do so selectively (depending on particles chosen) while having low emissivity in the infrared range (Abdelrahman, Fumeaux et al. 1979). In addition, the presence of glazing would minimize heat loss via volumetric emission (Hunt 1978). The

particle diameters were quoted in micrometres with Abdelrahman, Fumeaux et al. (1979) reporting diameters $D = 0.5\,\mu m$ and Hunt (1978) reporting diameters $D \leq 0.05\,\mu m$. The latter were within the nanoparticle size range ($< 100\,nm$ or $< 0.1\,\mu m$).

Other works published in this area included the volume heat-trap collectors (Arai, Itaya et al. 1984) and the use of molten salts (Anderson, Short et al. 1987, Bohn, Green et al. 1986a, Bohn, Wang 1986b, Kumar, Tien 1990). Recently, solid-gas suspensions were also investigated (Miller, Koenigsdorff 2000, Bertocchi, Karni et al. 2004) . These works involved the use of micro-sized particles with diameters in the range $0.1 \leq D \leq 0.6\,\mu m$.

The use of micro-sized particles, while successful, had its challenges. Among these were that the particles settled out of the fluid, clogged piping and corroded or fouled surfaces (Otanicar, Phelan et al. 2010a). In proposing the use of submicron particles, Hunt (1978) had foreseen that these would pass through mechanical equipment without corroding the surfaces. The use of submicron particles in volumetric absorption was, however, not revisited until the advent of nanofluids (Tyagi, Phelan et al. 2009, Choi 1995).

The term “nanofluid” was coined in reference to a novel class of heat transfer fluids in which nanoparticles are suspended in traditional heat transfer fluids (Choi 1995). Nanofluids offer greater stability since the size of nanoparticles allows them to remain suspended in the fluid for longer. Consequently, there is reduced clogging of piping and the fouling of surfaces. Nanofluids also offer greater property enhancement than “microfluids” due to the size effect of the nanoparticles; that is, they do not necessarily retain bulk material properties at nano-scale.

Since the pioneering work of Choi (1995), the next one and a half decades would be spent investigating the thermophysical and the rheological property enhancements in nanofluids. This was before they were tested in volumetric receivers by Tyagi, Phelan et al. (2009).

2.2 Nanofluids

The idea of solid-liquid suspensions has been around for over a century with initial theoretical work published by Maxwell in 1873 (cited in Eastman, Phillpot et al. (2004)). This was then extended by Hamilton & Crosser in 1962 (cited in Eastman, Phillpot et al. (2004)). These and subsequent studies were driven by the need to improve the thermophysical properties of engineering fluids since they are typically low-valued as illustrated in Table 2.

Table 2: Thermal conductivity values for various engineering materials at room temperature (Eastman, Phillpot et al. 2004).

Material		**Room temperature thermal conductivity (W m^{-1} K^{-1})**
Metallic solids	Silver	429
	Copper	401
	Aluminium	237
Non-metallic solids	Diamond	3300
	Carbon nanotubes	3000
	Silicon	148
	Alumina (Al_2O_3)	40
Metallic liquids	Sodium at 644K	72.3
Non-metallic liquids	Water	0.613
	Ethylene glycol	0.253
	Engine oil	0.145

Thermal conductivity enhancement was the major focus of early research. This was driven by the demand for greater cooling capacity than what could be provided by fins, micro-channels and other extended surfaces (Eastman, Phillpot et al. 2004, Wu, Zhao 2013). Few exceptional researchers focused on enhanced radiation absorption (Minardi, Chuang 1975).

The initial use of microfluids proved unsuitable because of particles settling out of the fluid. Subsequent effects such as clogging of channels (especially micro-channels), corrosion of surfaces and increased resistance to flow were undesirable. An alternative was thus required that solved the issue of stability of the suspended particles.

The introduction of nanofluids by Choi (1995) provided this alternative. Nanofluids were observed to give greater stability than microfluids. It was expected that below a certain minimum size, nanoparticles would “remain in suspension almost indefinitely” (Eastman, Phillpot et al. 2004). Mathematical arguments supporting their stability were also provided in terms of settling time for an ideal single particle in a stationary fluid (MacDevette 2013).

The stability of nanofluids was, however, observed to depend largely on the method of preparation (Eastman, Phillpot et al. 2004, Yu, Xie 2012, Haddad, Abid et al. 2014). Two methods of preparation are until now frequently employed – the two-step method and the one-step method.

In the two-step method, nanoparticles are firstly formed as dry powders by either chemical or physical means and then dispersed into a basefluid (Yu, Xie 2012). Dispersion is achieved by agitation provided by either ultrasonic or magnetic means (Yu, Xie 2012). In the one-step method, nanoparticles are generated while being simultaneously dispersed into a basefluid (Yu, Xie 2012).

The two-step method has been mainly employed to create non-metallic nanofluids (Haddad, Abid et al. 2014, Wang, Mujumdar 2007). Its key advantage is that it is economical since nanopowder production methods have been developed to industrial scales (Yu, Xie 2012). On the other hand, its key disadvantage is that dry nanopowders have a tendency to aggregate. Thus to obtain stable nanofluids, extra options have to be explored such as the use of surfactants, varying the pH value of the nanofluid (Haddad, Abid et al. 2014) or surface treatment of nanoparticles (Yu, Xie 2012).

The one-step method has been employed to create metallic nanofluids (Yu, Xie 2012). Its key advantage is that minimal aggregation of nanoparticles occurs. Consequently, nanofluids with greater stability are produced. It is, however, more expensive than the two-step method and is thus less commonly employed.

Beyond stability, the method of preparation was also observed to affect the properties of nanofluids (Wu, Zhao 2013). This was in addition to a large number of other parameters such as choice of materials, size and morphology of particles, volume fraction and temperature. The presence of such a large parametric space has resulted in varying and often contradicting results on property enhancements (Wu, Zhao 2013).

In reviewing nanofluid literature, the author of this study paid attention to those nanofluids whose thermophysical and radiative properties have been previously characterised. Few nanofluids were found to be so extensively characterised. For example, graphite – water nanofluid that has been frequently cited in solar harvesting literature has not been characterised for its thermophysical properties.

Of the characterised nanofluids found, it was noted that temperature dependent studies had been conducted for low temperatures only ($< 100^{o}C$). Two nanofluids of interest were found, namely, aluminium oxide – water and copper oxide – water nanofluids. The former was, however, rejected as it scatters radiation more than it absorbs it (Said, Saidur et al. 2014). Copper oxide – water nanofluid was adopted for the study. More on this is presented in Chapter 3.

2.3 Nanofluid-based volumetric receivers

The use of nanofluids in solar harvesting has received increasing attention from researchers in recent years as illustrated by the growing number of publications in this area. Several review papers are available on this topic (Javadi, Saidur et al. 2013, Mahian, Kianifar et al. 2013, Kasaeian, Eshghi et al. 2015, Verma, Tiwari 2015). A review of the literature is presented below with a focus on the modelling of parallel plate volumetric receivers and key results. To aid in the review, it is useful to consider volumetric receivers in terms of the flux (high or low) and geometry (parallel or cylindrical). These categories are employed in the following discussion starting with the low flux, parallel geometry volumetric flow receivers.

Tyagi, Phelan et al. (2009) were the first to apply nanofluids to volumetric absorption. Theirs was a theoretical study that was similar to work done by Hunt (1978) on solid-gas suspensions with submicron particles. Tyagi, Phelan et al. (2009) applied a Rayleigh scattering model to predict the optical properties of aluminium – water nanofluid. They illustrated that the Rayleigh model could be simplified by neglecting the scattering term since the scattering efficiency was a function of D^4, with D being the nanoparticle diameter ($D \leq 100\ nm$). The absorption efficiency was shown to be roughly a linear function of the diameter.

Tyagi, Phelan et al. (2009) investigated the performance of the receiver by modelling it using a unidirectional Beer – Lambert model for spectral intensity,

$$\frac{dI_\lambda}{dy} = -\left(K_{a,\lambda} + K_{s,\lambda}\right)I_\lambda = -K_{e,\lambda}I_\lambda\ , \tag{2.1}$$

where I_λ is the spectral radiation intensity. $K_{a,\lambda}$, $K_{s,\lambda}$ and $K_{e,\lambda}$ are the nanofluid's spectral absorption, scattering and extinction coefficients as given by the Rayleigh scattering model. The 2D steady state energy equation,

$$\rho_{nf} {c_p}_{nf} u \frac{\partial T}{\partial x} = k_{nf} \frac{\partial^2 T}{\partial y^2} - \frac{\partial q_r}{\partial y}\ , \tag{2.2}$$

was also employed in which T is the fluid's temperature, ρ is the nanofluid's density and c_p the nanofluid's specific heat capacity at constant pressure. k is the nanofluid's thermal conductivity, u the nanofluid's velocity and $\frac{\partial q_r}{\partial y}$ the divergence of the net radiative heat flux.

Approximating the spectral radiative properties with band averaged values, they illustrated that efficiency (equation (1.2)) increased with increasing volume fraction to an optimum value ($\phi = 2\%$). Thereafter, it levelled off as illustrated in Figure 2.

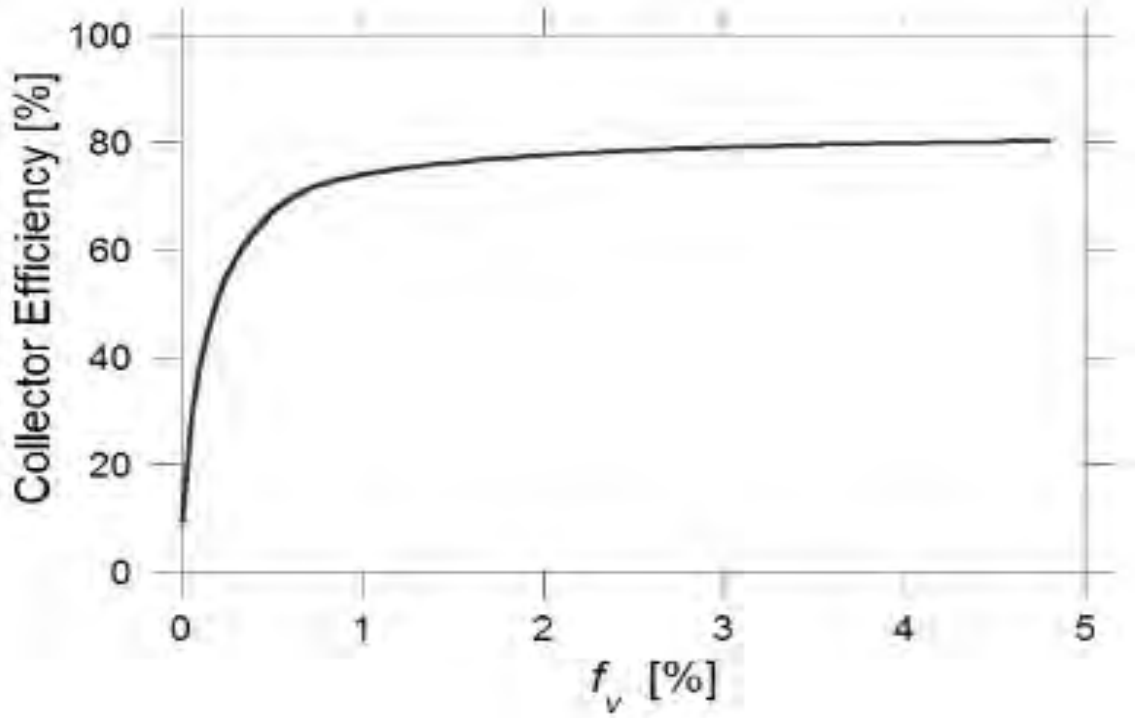

Figure 2: Volumetric collector efficiency versus volume fraction of the particles (Tyagi, Phelan et al. 2009).

Similar results were obtained for varying receiver height whereas the receiver length and the particle diameter were seen to have minimal effect on efficiency. Increasing the fluid inlet temperature above the ambient temperature was seen to cause a linear decrease in efficiency. It was also observed that the volumetric receiver was roughly 10% more efficient on an absolute basis than a conventional surface collector under similar working conditions (Tyagi, Phelan et al. 2009).

Tyagi, Phelan et al. (2009) went further to illustrate that peak temperatures developed at the surface similar to surface absorbers as shown in Figure 3. This would imply that thermal heat loss was concentrated at the surface.

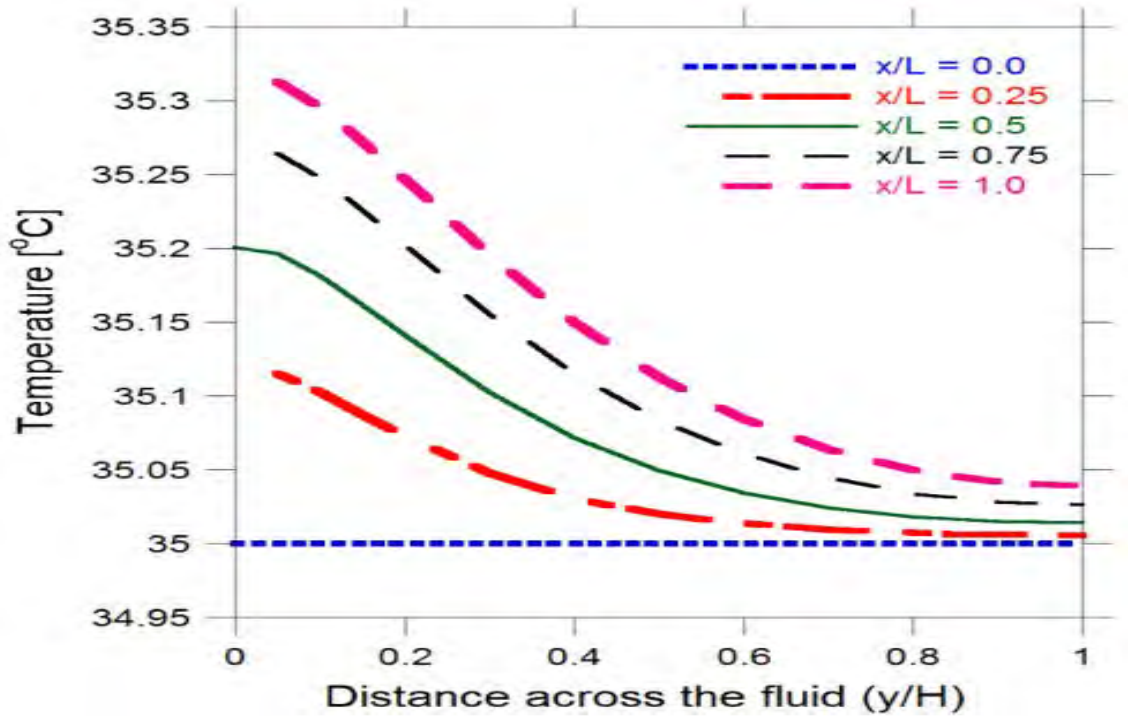

Figure 3: Temperature profiles within the volumetric collector for a volume fraction, $\phi = 0.8\%$ and diameter, $D = 5\ nm$ (Tyagi, Phelan et al. 2009).

The use of the independent single scattering assumption was valid for volume fractions $\phi \leq 0.6\%$. However, Tyagi, Phelan et al. (2009) conducted their work at volume fractions greater than this limit (up to $\phi = 5\%$) as seen in Figure 2. It was later illustrated that for small volume fractions, $\phi \leq 1\%$, the independent single scattering assumption was reasonably correct for diameters $D \leq 30\ nm$ (Otanicar, Taylor et al. 2009c). Beyond that, a model accounting for dependent and multiple scattering was required (Otanicar, Taylor et al. 2009c).

Using both assumptions, Otanicar, Taylor et al. (2009c) showed that the independent scattering assumption resulted in an under-prediction of efficiency. The magnitude of the under-prediction increased with increasing volume fraction (see Figure 4). These results were limited to micro-channels hence small optical depths, $\tau = K_e y < 10$. However, Tyagi, Phelan et al. (2009) had investigated mini-channels with larger optical depths. It is reasonable to expect that larger differences in prediction of the two models would be observed as efficiency had already been shown to vary with height (Tyagi, Phelan et al. 2009).

The results by Otanicar, Taylor et al. (2009c) also illustrated that the efficiency increased with volume fraction to a point ($\phi < 1\%$ as seen in Figure 4) and thereafter decreased. This was in contrast to what had been reported earlier (Tyagi, Phelan et al. 2009).

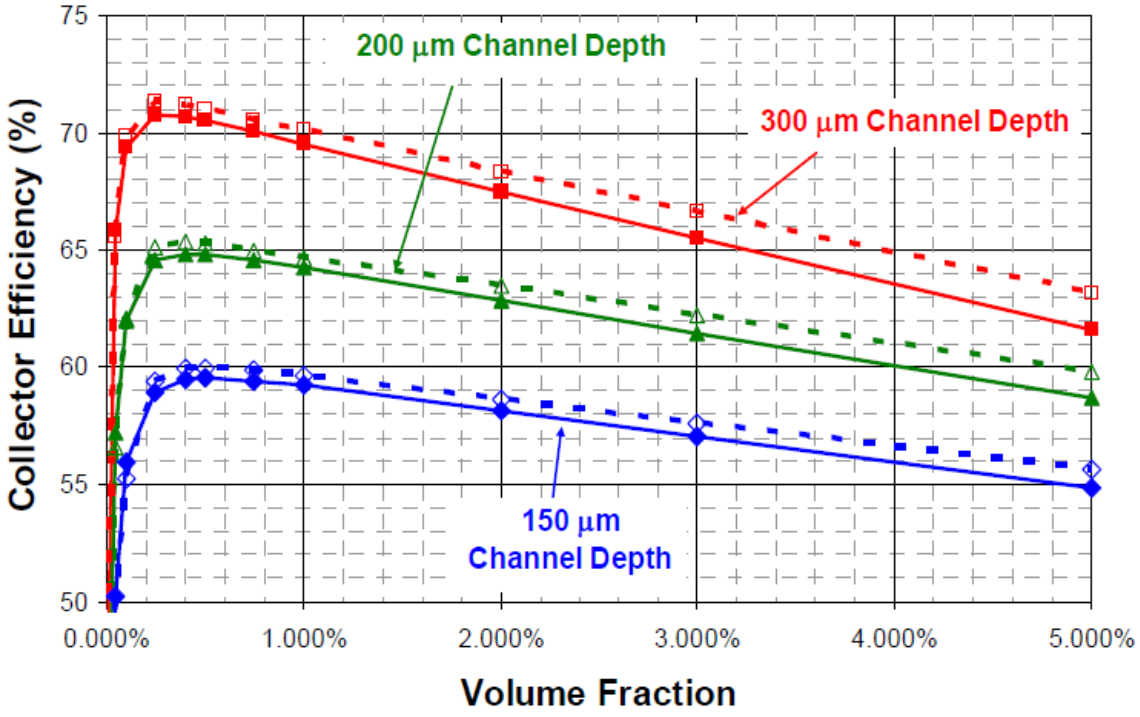

Figure 4: Volumetric collector efficiency versus volume fraction of graphite nanoparticles for different optical depths. The solid line represents independent scattering while the dashed line represents dependent and multiple scattering (Otanicar, Taylor et al. 2009c).

The model employed in Otanicar, Taylor et al. (2009c) was based on their previous work (Otanicar, Phelan et al. 2009a). The latter involved the experimental testing of a micro-solar collector and modelling it with a variant of the Beer – Lambert model as given below,

$$\frac{dI_{i,\lambda}}{dy} = K_{a,\lambda} I_{b,\lambda} - K_{e,\lambda} I_{i,\lambda}\,, \qquad (2.3)$$

where $I_{b,\lambda}$ is the spectral blackbody emitted radiation intensity and i represents the directional nature of intensity. $i = +1$ is in the direction of solar radiation and $i = -1$ in the opposite direction.

This model was modified to account for volumetric emission and specularly reflecting top and bottom boundaries resulting in a two-flux model for intensity (compare equation (2.1)). The model was verified against experimental values for graphite – water nanofluid ($D = 30\,nm$, $0.05\% \leq \phi \leq 1\%$). It was seen to give predictions within 5% with an under-prediction at low volume fraction ($\phi < 0.1\%$) and over-prediction at high volume fraction (Otanicar, Taylor et al. 2009c) .

The experimental work involved the testing of graphite – water ($D = 30\,nm,\ 0.05\% \leq \phi \leq 1\%$), carbon nanotubes – water ($6 \leq D \leq 20\,nm,\ 0.05\% \leq \phi \leq 1\%$) and silver – water ($0 < D < 60\,nm,\ 0.05\% \leq \phi \leq 0.25\%$) nanofluids (Otanicar, Phelan et al. 2010a, Otanicar, Phelan et al. 2009a). The results obtained were as illustrated in Figure 5 below.

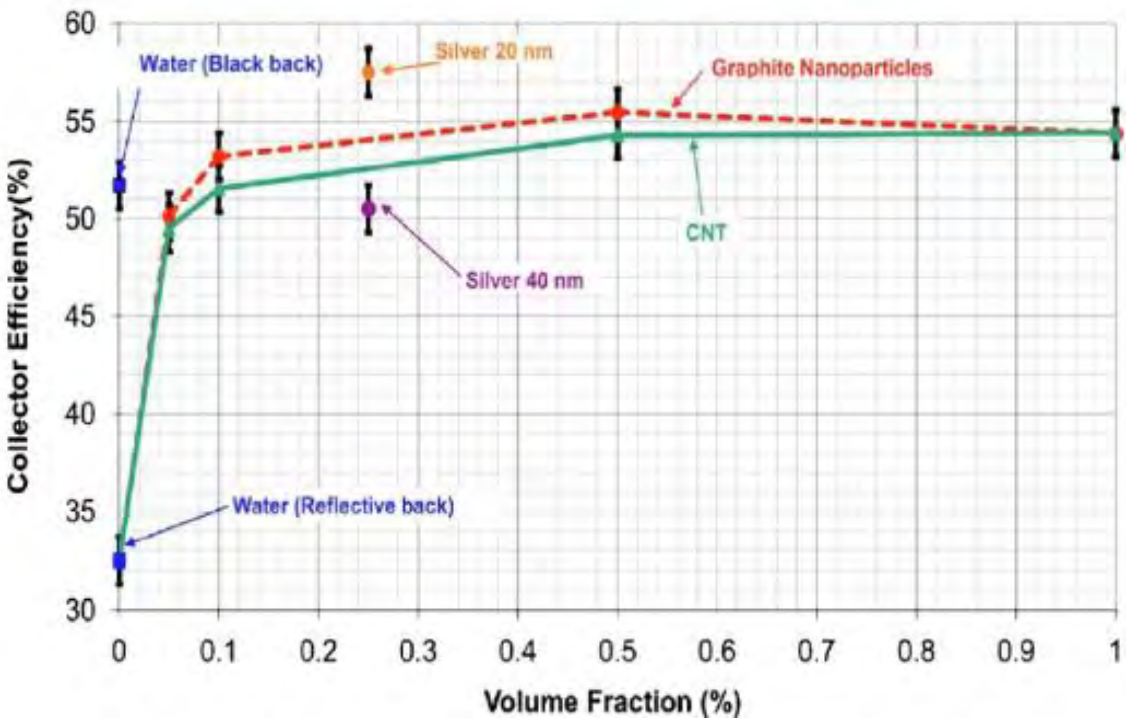

Figure 5: Experimental volumetric collector efficiency versus volume fraction of particles (Otanicar, Phelan et al. 2010a).

Key results included efficiency improvements of about 3% for spherical graphite nanoparticles over conventional flat surface absorbers. Similar efficiency improvements of about 5% were reported for spherical silver nanoparticles $(D = 20\,nm)$. A much larger improvement ($\cong 20\%$) was noted in the use of nanofluids over the use of water with a reflective surface (Otanicar, Phelan et al. 2010a, Otanicar, Phelan et al. 2009a).

The collector efficiency was seen to rise rapidly with increase in volume fraction up to approximately $\phi = 0.5\%$ beyond which it levelled off or decreased as observed for graphite – water nanofluid. Otanicar, Phelan et al. (2010a) reasoned that at extremely low volume fractions, the absorbing capacity of the nanofluid was similar to that of water. Consequently, there was little heating. However, as the volume fraction increased, the nanofluid was able to absorb more radiation leading to higher efficiencies. At even higher volume fractions, the nanofluid became opaque to radiation. This increased opacity resulted in radiation being absorbed in a small layer of fluid near the surface, locally increasing the temperatures. As a result, heat loss was experienced akin to surface absorbers (Otanicar, Phelan et al. 2010a).

The impact of choice of material for nanoparticles was seen with the results of graphite and carbon nanotubes as contrasted with those of silver nanoparticles. The first two had similar performance with their efficiency predictions being within 1% of each other (Otanicar, Phelan et al. 2010a). The results of silver illustrated either higher or lower efficiency depending on particle size (see Figure 5).

Efficiency increased with a decrease in size of silver nanoparticles. In Figure 5, at a volume fraction of $\phi \cong 0.25\%$, an efficiency increase of approximately 7% was observed when the nanoparticle size decreased from $40\,nm$ to $20\,nm$. It was also observed that the magnitude of efficiency increase was greater for higher volume fractions as seen in Figure 6. The efficiency increase for volume fraction of $\phi = 0.05\%$ was lower than that of volume fraction of $\phi = 0.1\%$ for the same decrease in nanoparticle size.

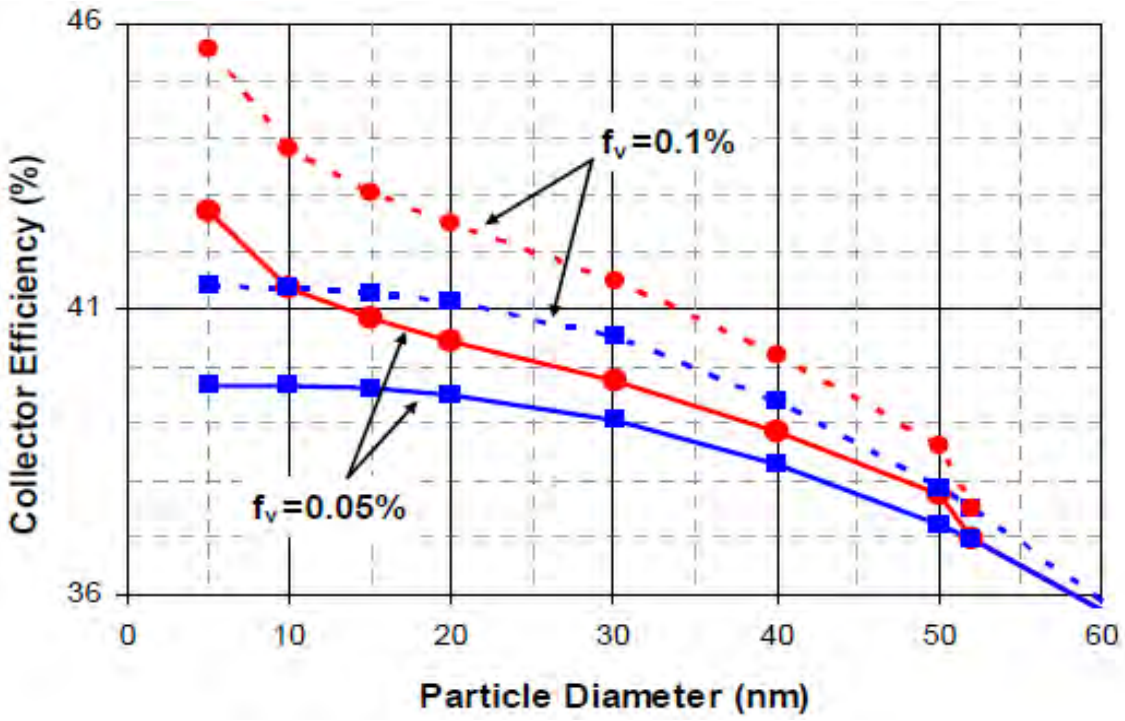

Figure 6: Volumetric collector efficiency versus diameter of silver nanoparticles. The square markers represent bulk properties while the circle markers represent size dependent properties (Otanicar, Taylor et al. 2009c).

Similar results were obtained for gold nanoparticles whereas graphite showed no size dependent properties. Otanicar, Phelan et al. (2010a) postulated that a decrease in size of a nanoparticle resulted in broadening of its absorption peak (if present) resulting in stronger absorption of the solar spectrum. Gold and silver were observed to have “strong peaks within the solar spectrum” unlike graphite which had “a well distributed absorption throughout the

spectrum" with a weak absorption peak thus exhibiting no size effects (Otanicar, Phelan et al. 2010a).

Subsequent studies investigated the influence of the spatially varying extinction coefficients on volumetric absorption given various bottom boundary conditions (Otanicar, Phelan et al. 2010b, Otanicar, Phelan et al. 2011). This was done by employing models previously used (equation (2.3)). In addition, the extinction coefficients were approximated as gray (constant with wavelength) and within ranges of what would be used as a solar harvesting nanofluid. The extinction coefficients were assumed to be homogeneous, linearly varying and exponentially varying.

Otanicar, Phelan et al. (2011) illustrated that differences in performance were observable for small optical depths only. The perfect absorbing bottom boundary gave higher receiver efficiencies as compared to the perfectly reflecting and the transparent bottom boundary for the various spatial distributions of the extinction coefficient and at small optical depths ($\tau < 5$). At some intermediate optical depth ($5 < \tau \leq 10$), the perfect reflecting bottom boundary achieved the maximum efficiency for the linearly increasing and exponentially increasing extinction coefficient profiles. The transparent bottom boundary gave the least efficiency in all cases.

In another study, Zhu, Li et al. (2010) reported on the use of metal oxides as nanoparticles in volumetric collectors. The philosophy behind the work was that metal nanoparticles previously used could be easily oxidised in water and hence using oxides provided chemically stable nanofluids. Numerical results were based on a Beer – Lambert model and a Rayleigh independent single scattering model for optical properties similar to previous work (Tyagi, Phelan et al. 2009). A parabolic flow profile was used in the energy equation unlike previous works that assumed a plug flow profile. It was later suggested that a plug flow profile overestimates the efficiencies (Karami, Raisee et al. 2014).

The study employed silicon oxide – water and titanium oxide – water nanofluids at diameters $D = 20\,nm$ and $D = 5\,nm$ respectively and a volume fraction $\phi = 0.3\%$ (Zhu, Li et al. 2010). Measured values of extinction coefficient for silicon oxide – water nanofluid differed from those of the Rayleigh model especially in the short wavelength region, $\lambda < 600\,nm$. Better agreement with results was obtained for titanium oxide – water nanofluid. Reasons suggested for this included possible presence of impurities in the experiments and assumptions in the optical property model.

Measured temperature profiles for both nanofluids were similar to those shown in Figure 3 illustrating peak temperatures developing at the surface. Using experimentally measured extinction coefficient values and solving the receiver model equations, temperature profiles were obtained that were in qualitative agreement with those measured earlier. However, quantitative errors of 22% and 12% were observed for silicon oxide – water and titanium oxide – water nanofluids respectively.

A recent study has reported on the performance of graphite – water nanofluids (Ladjevardi, Asnaghi et al. 2013). A model similar to that of Tyagi, Phelan et al. (2009) was employed. There were a few modifications with the most notable being the use of a realistic solar spectrum for the incident flux top boundary condition. Previous studies had employed the Planck's black body approximation. Spectral radiative properties of the nanofluid were also employed. The authors illustrated the advantage of using graphite – water nanofluid over pure water by computing outlet temperatures for both cases (Ladjevardi, Asnaghi et al. 2013).

The above studies concentrated on low flux collectors with incident radiation flux, $G \leq 1000\ W/m^2$. The results were applicable to low temperature systems, for example, domestic water heaters. Solar collectors are, however, also employed in high temperature systems like industrial process heating and power plants (Zhu, Zhang 2012). There was thus a need for studies on high flux collectors and these were also conducted (Lenert, Zuniga et al. 2010b, Lenert, Wang 2012, Lenert 2010a, Taylor, Phelan et al. 2011a, Taylor, Phelan et al. 2012, Taylor, Phelan et al. 2010).

Initial studies into high flux collectors focused on beamed down concentrated incident radiation flux, CG with concentration ratio $C < 100$ and incident flux $G = 1000\ W/m^2$ (Lenert, Zuniga et al. 2010b, Lenert, Zuniga et al. 2010b, Lenert 2010a). Stationary nanofluids were employed in which energy transfer was by transient conduction. This was unlike previous works in which the nanofluid was non-stationary and energy transfer was by forced convection. Nanofluids employed were graphite – Therminol VP1 and carbon coated cobalt – Therminol VP1 (Lenert 2010a).

The Beer – Lambert model was used with an ideal specular reflector at the bottom thus resulting in a two-flux model (equation (2.3)). The model was solved for in the spectral range $\lambda < 2\ \mu m$ and the nanofluid assumed to behave like a perfect absorber in the spectral range $\lambda > 2\ \mu m$. This allowed the treatment of thermal emission in $\lambda > 2\ \mu m$ as a top boundary condition in the energy equation. The emission term in $\lambda < 2\ \mu m$ was either approximated (Lenert 2010a) or ignored (Lenert, Zuniga et al. 2010b) . In both cases, it was assumed that

emission would not be significant as quantified in terms of the emitted power being less than 20% at wavelengths $\lambda < 2\ \mu m$ for temperatures, $T \leq 1200K$.

To validate the numerical model, experiments were conducted with an average incident radiation flux of $CG = 2620\ \pm 184\ W/m^2$ from a solar simulator with wavelength range, $0 < \lambda < 1.6\ \mu m$. Spectral radiative properties were employed based on empirical model fitting of experimental data obtained in a manner similar to previous work (Zhu, Li et al. 2010). The model captured the general shape of the temperature profile. However, it under-predicted surface temperatures while over-predicting temperatures towards the bottom. The discrepancies were attributed to experimental error dominated by heat loss to the sidewalls and a failure by the model to capture the divergence of the radiation source profile.

Lenert & Wang (2012) employed an improved radiation transport model that catered for the directional properties of radiation. The introduction of the directional dependence was necessary for the full treatment of emitted radiation as it travels in all directions in space. The model was given as,

$$\mu \frac{\partial I_\lambda}{\partial y} = K_{a\lambda} I_{b,\lambda} - K_{e\lambda} I_\lambda , \qquad (2.4)$$

where $\mu = \cos\theta$ is the directional cosine and other terms retain their previously defined meanings.

Equation (2.4) gave better predictions which were found to be within 20% of experimental results (Lenert, Wang 2012). Using this model, Lenert & Wang (2012) illustrated that temperature inversion could occur in the receiver with the surface temperature being lowered below that of the bulk fluid. This implied lower thermal heat loss occurred at the surface, confirming the observations of Hunt (1978). Previous works had failed to observe this (see Figure 3).

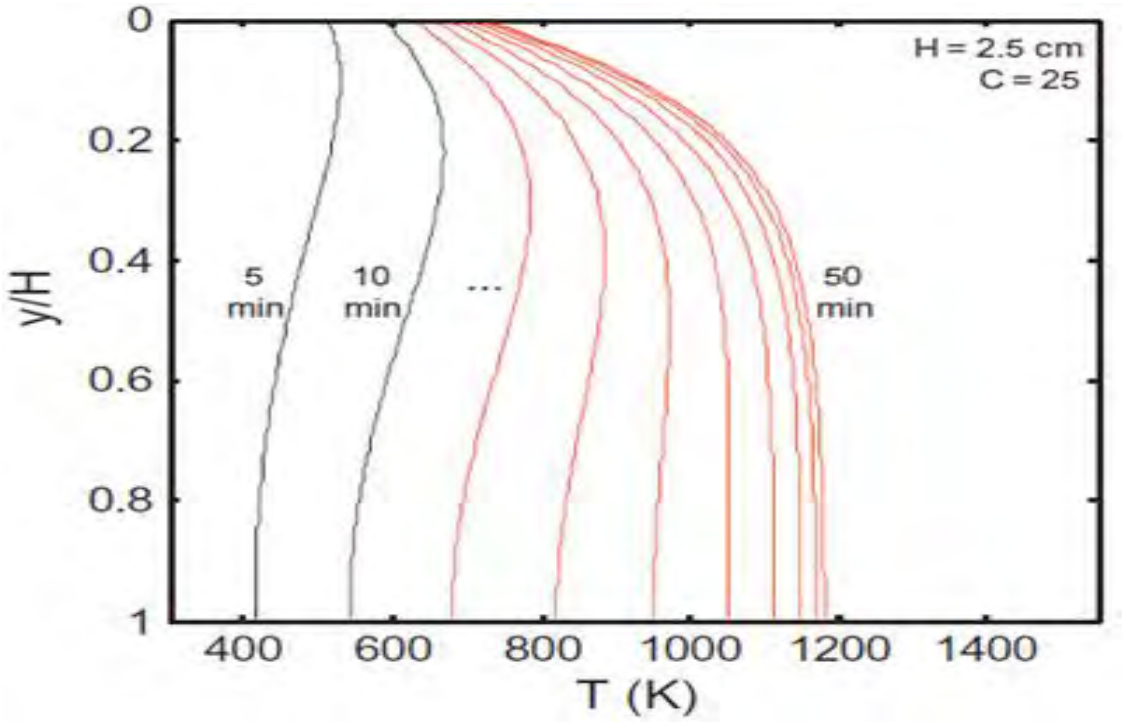

Figure 7: Temperature evolution with time within the volumetric collector for an optical depth, $\tau = 1.7$, a concentration ratio, $C = 25$ and height, $H = 2.5\ cm$ (Lenert, Wang 2012).

Temperature inversion profiles observed were more pronounced for higher concentration ratios and taller receivers. These profiles evolved with time and became near isothermal at high temperatures. At these temperatures, radiative exchange within the body was more effective than conduction at redistributing energy, both processes possessing a diffusive effect (Lenert, Wang 2012). This steady state was achieved in short times for great concentrations and shorter receivers, giving an indication as to design considerations for optimal exposure time.

The effects of height and concentration ratio on the receiver efficiency were also studied with efficiency defined as,

$$\eta_{collector} = \frac{mc_p(\bar{T}_{out} - \bar{T}_{in})}{ACGt_{exp}}\ , \qquad (2.5)$$

where m is the mass of the fluid, t_{exp} is the exposure time and other terms are as previously defined.

Lenert & Wang (2012) showed that efficiency increased with increasing concentration ratio for a given mean outlet temperature. This was due to shorter exposure times required to reach the given temperature. Equally, for a given receiver efficiency, increasing the

concentration ratio increased the mean fluid outlet temperature for a given exposure time. This was illustrated in Figure 8.

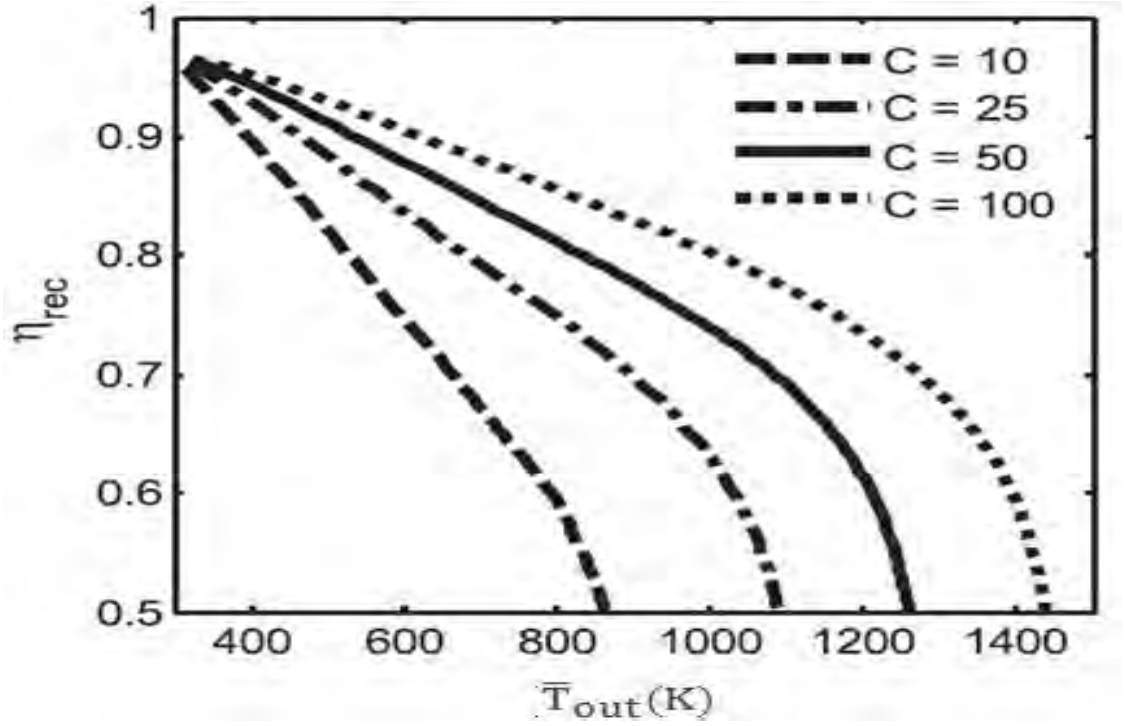

Figure 8: Volumetric receiver efficiency versus mean outlet temperature for various concentration ratios, $10 \leq C \leq 100$ (Lenert, Wang 2012).

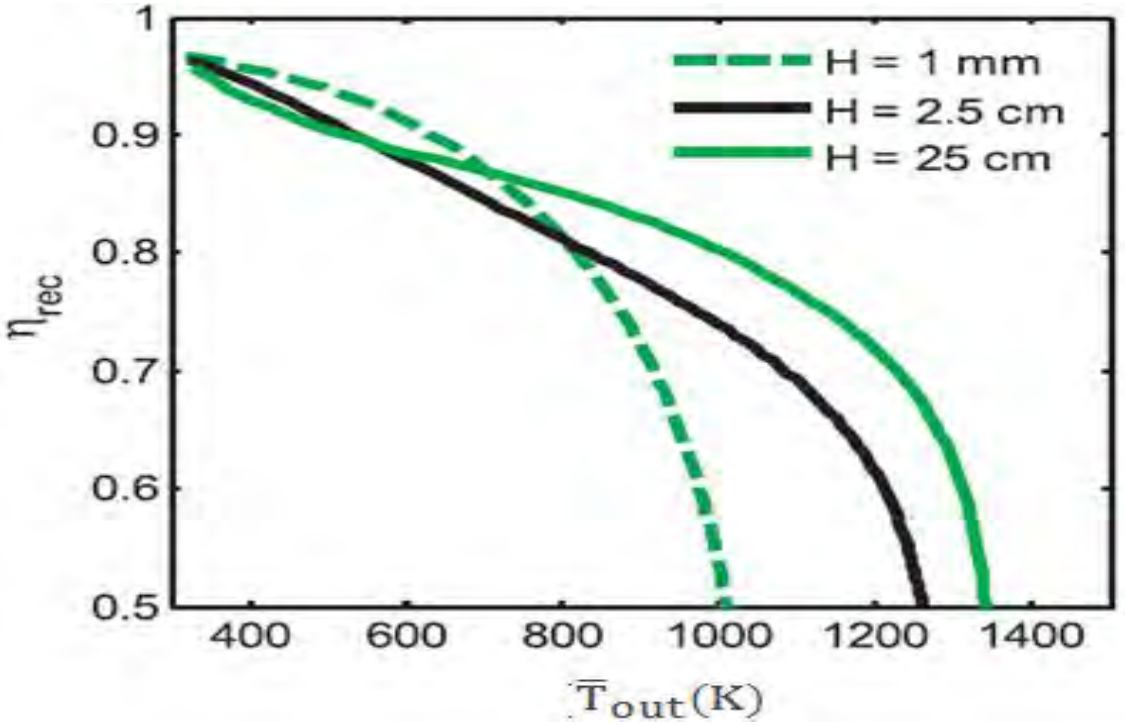

Figure 9: Volumetric receiver efficiency versus mean outlet temperature for various heights, $0.1 \leq H \leq 25\ cm$ (Lenert, Wang 2012).

The effect of height was reported as being twofold depending on temperature; below $700\,K$, efficiency decreased with increasing height whereas when temperature was in the range $800 - 1200\,K$ efficiency increased with increasing height (see Figure 9). The behaviour in both cases was linked to the fact that increasing height amplified the difference in the bulk fluid and the surface temperatures. In the former case ($< 700\,K$), surface temperature was higher whereas in the latter case, temperature profile inversion had occurred and bulk fluid temperature was higher.

A shortcoming of the work by Lenert & Wang (2012) was that the nanofluid was tested allowing high temperatures to be achieved with thermophysical properties of the nanofluid assumed constant. These were evaluated at room temperature. Predictions were also made for temperatures beyond the breakdown point of the basefluid ($\cong 650\,K$).

Taylor, Phelan et al. (2010, 2011a) investigated the performance of volumetric flow receivers with incident radiation flux, CG where $100 < C < 1000$ and $G = 1000\,W/m^2$. A spot focus concentrator (that forms an image of the sun on the collector's absorbing area) was used as opposed to linear focus concentrators previously studied. They, as a result, employed a short receiver.

Spectral optical properties were developed according to the independent single scattering Rayleigh model as detailed in a nanofluid characterisation study (Taylor, Phelan et al. 2011b). The bidirectional Beer – Lambert model (equation (2.3)) was coupled to the energy equation and employed to study the performance of the receiver. To validate the model, experiments were run for a dish collector ($C \cong 400$) with graphite – Therminol VP1 nanofluid. The model was found to predict accurately for low volume fraction of $\phi = 0.125\%$ but poorly for high volume fraction with quoted errors of $30\% - 40\%$ at volume fraction of $\phi = 0.25\%$.

The effect of solar concentration ratio on efficiency was studied for Therminol VP1 – copper nanofluid ($\phi = 0.001\%$, $D = 20\,nm$). They combined the heat engine and collector efficiencies (equations (1.1) and (1.2)) according to equation (2.6) in which a factor of 0.5 was introduced to cater for the heat engine running at 50% Carnot efficiency.

$$\eta_{system} = 0.5\,\eta_{Carnot}\eta_{collector}. \qquad (2.6)$$

The investigations were done at various outlet temperatures (200^0C, 300^0C, 400^0C) with the upper temperature limit imposed to maintain operations with Therminol VP1 as a liquid. Mass

flow rates were adjusted until the desired outlet temperatures were obtained. The flow was found to be turbulent due to the short receiver length.

Taylor, Phelan et al. (2011a) reported that efficiencies of up to 10% above conventional surface collectors were achievable by nanofluid-based receivers. Concentrations ratios of $100 - 1000$ were tested with maximum efficiency observed to occur at a ratio of approximately $275 - 300$. This was as illustrated in Figure 10 in which the maximum efficiency was also seen to shift to higher concentration ratios for higher outlet temperatures. This was in line with earlier results illustrated in Figure 8 (Lenert, Wang 2012).

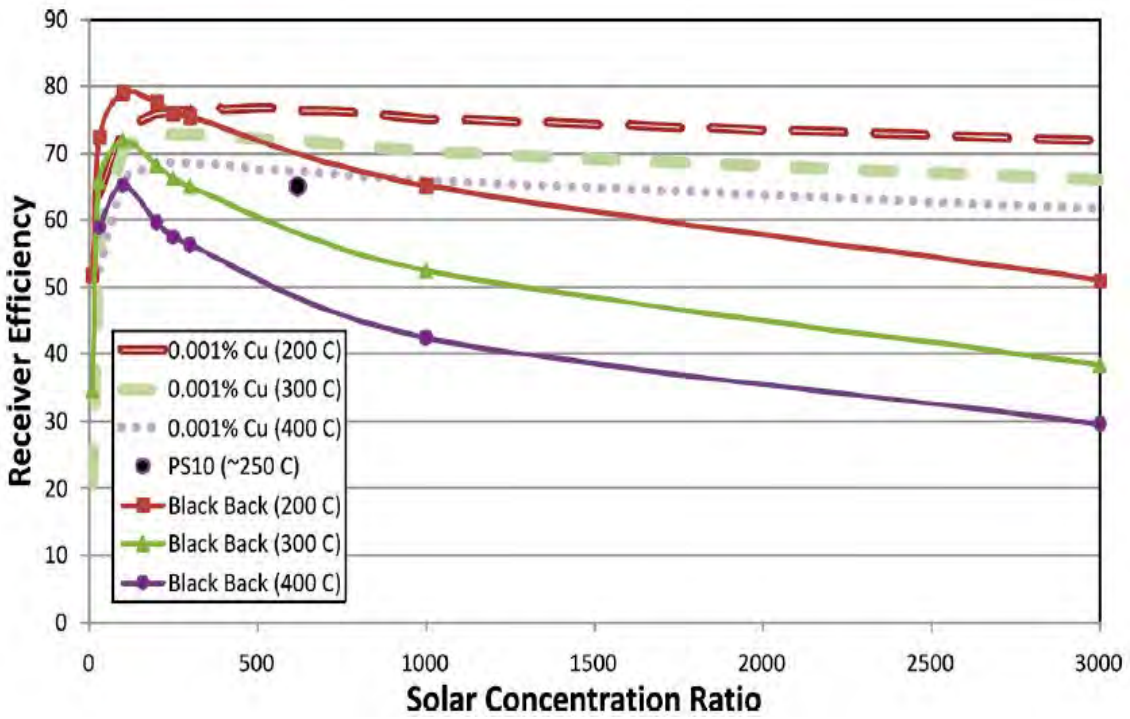

Figure 10: Volumetric collector efficiency versus solar concentration ratio for a volume fraction, $\phi = 0.001\%$ (Taylor, Phelan et al. 2011a).

Veeraragavan, Lenert et al. (2012) introduced an analytical method to solve the non-dimensionalised problem. They considered a receiver operating in the low to mid-temperature regime with incident flux, CG where $C < 30$ and $G = 1000\, W/m^2$. The unidirectional Beer – Lambert model (equation (2.1)) was employed. Radiative properties were taken as gray and corresponding to values of graphite and Therminol VP1 at $0.5\, \mu m$ (Veeraragavan, Lenert et al. 2012).

They illustrated that temperature inversion could be achieved at a point far from the inlet. Beyond this point, a steady state temperature profile could also be achieved when the heat lost equalled the heat gained. This corresponded to results by Lenert & Wang (2012). The

impact of such axial temperature development on Carnot and receiver efficiencies was a respective asymptotic increase and decrease with increase in length implying that beyond a certain length, temperature increase is minimal.

As an example of length optimisation, the authors used the total/system efficiency concept (a product of receiver efficiency and Carnot efficiency) and their analytical model to obtain a 35% maximum total efficiency at a dimensionless length of 0.86 (see Figure 11). The length was non-dimensionalised with respect to the flow's Peclet number and the receiver's height.

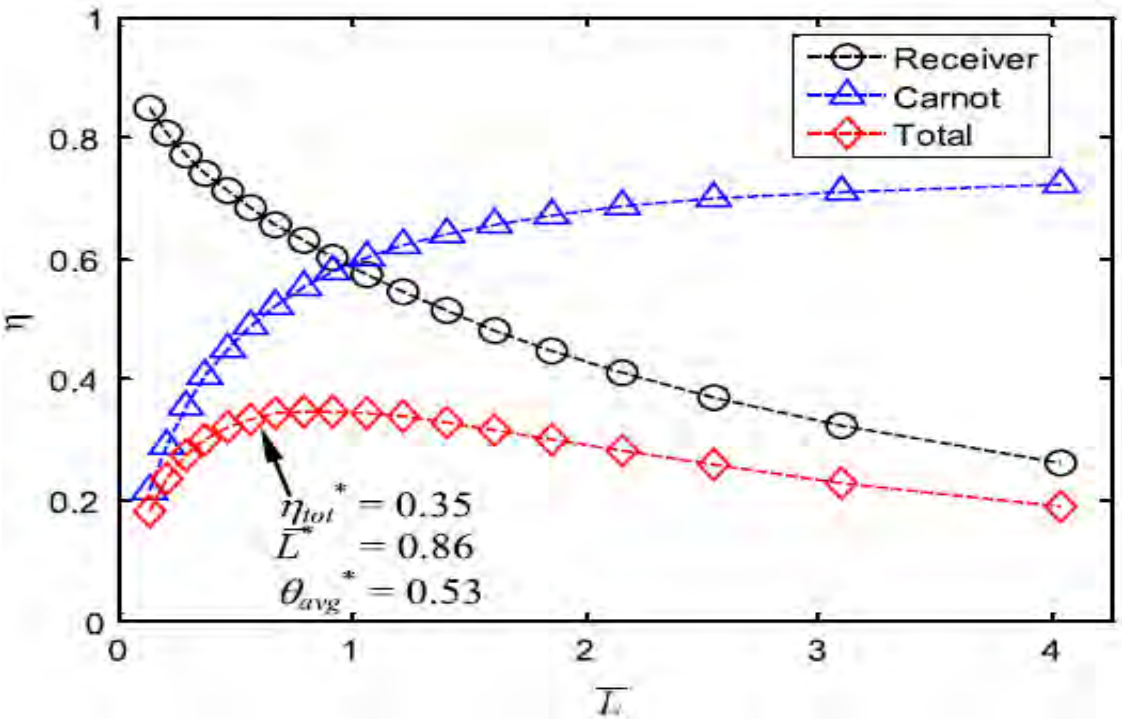

Figure 11: Volumetric receiver, Carnot and total system efficiencies versus the dimensionless length ($\bar{L}$) (Veeraragavan, Lenert et al. 2012).

In another study, a 3D volumetric receiver was simulated employing the full radiation transport equation with scattering neglected (Kaluri, Vijayaraghavan et al. 2015). The equation was solved using the conservative discrete ordinate method alongside the energy and momentum equations for turbulent flow. Similar to previous work (Taylor, Phelan et al. 2011a), a spot focus incident flux was considered. Two nanofluids were employed; graphite – water (considered gray) and copper sulphate (considered non-gray with 2 band spectral averaging). Studies were limited to the wavelength range $0.4 < \lambda < 1\,\mu m$. The model was validated against experiments and was reported to give results accurate to within 7% and 12% for graphite – water and copper sulphate nanofluids respectively.

Parametric studies by Kaluri, Vijayaraghavan et al. (2015) indicated that efficiency increased with increasing concentration ratio with the highest ratio simulated being $C = 683$. This increase was most significant when there was a large difference between inlet temperature and ambient temperature. Similarly, the increase was least significant when the difference approached zero. Earlier experimental work had reported comparable results (Vijayaraghavan, Ganapathisubbu et al. 2013). In the latter, it was illustrated that for small differences between the inlet and ambient temperatures, the receiver efficiency was largely independent of concentration ratio for a spot focus receiver.

It was further observed in both works that for a given concentration ratio, highest performance was achieved when there was minimal difference between inlet and ambient temperature. This was in line with results obtained for low flux line focus receivers (Tyagi, Phelan et al. 2009). Kaluri, Vijayaraghavan et al. (2015) also showed that efficiency was generally independent of the mass flow rate and this was in agreement with the findings of Vijayaraghavan, Ganapathisubbu et al. (2013).

Beyond the above reviewed applications in parallel plate volumetric receivers, other works were also published. These included those in cylindrical geometry receivers. Examples were the linear parabolic collectors (Khullar, Tyagi 2011, Khullar, Tyagi et al. 2013, Kasaeian, Daviran et al. 2015) and the tubular collectors reviewed elsewhere (Mahian, Kianifar et al. 2013).

Khullar, Tyagi et al. (2013) numerically investigated the performance of a "concentrating parabolic solar collector". Employing the radiation transfer equation with scattering neglected and the energy equation in cylindrical coordinates, they investigated the performance of aluminium – Therminol VP1 ($\phi = 0.05\%$, $D = 5\,nm$) nanofluid. They reported that the nanofluid-based collector had a higher efficiency than a conventional parabolic trough. This was due to higher sensible heat gain that resulted from enhanced radiation absorption of the nanofluid.

Khullar, Tyagi et al. (2013) also investigated the impact of temperature dependent thermophysical properties on the collector efficiency. They reasoned that the thermal diffusivity of the nanofluid would be dominated by that of the basefluid (Therminol VP1). Their results indicated that the collector efficiency did not vary significantly with changes in the basefluid's thermal diffusivity.

A recent study on parabolic collectors experimentally investigated the performance of MWCNT – mineral oil nanofluid (Kasaeian, Daviran et al. 2015). It illustrated that a $4\% - 7\%$

enhancement in efficiency could be achieved over the use of pure oil as the heat transfer fluid.

Advanced concepts have also been explored in literature with respect to volumetric absorption. Such concepts have included the use of non-spherical nanoparticles such as the single-walled and the multi-walled carbon nanotubes and nanohorns (Sani, Barison et al. 2010, Mercatelli, Sani et al. 2011, Mercatelli, Sani et al. 2012). There has also been the use of different combinations of core-shell nanoparticles in plasmonic nanofluids (Wu, Zhou et al. 2015). Additionally, the use of nanofluids in hybrid photovoltaic thermal (PV/T) collectors (Taylor, Otanicar et al. 2012) and in volumetric boiling (Taylor, Phelan et al. 2012) has been considered. In all these studies, greater efficiencies have been reported upon application of nanofluids illustrating their enormous potential in solar thermal harvesting.

2.4 Summary

From the foregoing discussion, it can be seen that few experiments have been performed on nanofluid-based volumetric receivers. From these, it has been established that the use of nanofluids improves the efficiency of volumetric flow receivers. This has mainly been attributed to the enhanced absorption properties.

This increase in efficiency has, however, been seen to be limited by a number of factors such as the volume fraction and boundary conditions. It has been shown that an increase in volume fraction beyond a certain maximum value results in a decrease in efficiency. Similar observations have been suggested for the concentration ratio. It has also been seen that maximum efficiency is attained when the inlet temperature equals the ambient temperature. Alternatively, preheating of the nanofluid does not translate to an enhanced efficiency .

To extend such studies to other parameters, there has been a dependence on numerical models. These models have increasingly grown in complexity to reflect the physics of the problem as illustrated in equation (2.1) versus equation (2.4). However, the presence of assumptions such as the approximation of spectral properties and the assumption a non-absorbing basefluid has resulted in poor performance of the models. This has been illustrated by the testing of models against experiments with predicted values being found to be anywhere within $5\% - 40\%$ of experimental values. Furthermore, the impact of temperature-dependent thermophysical properties (density, specific heat capacity, conductivity, etc.) on the receiver's performance has not been investigated. The singular

exception to this has been a study in which the thermal diffusivity of the basefluid was considered.

Hence, there exists a need to study the performance of volumetric flow receivers under more realistic models (radiative and thermophysical) and boundary conditions. This study addresses this need by building upon the existing radiation models for the volumetric flow receiver and simulating its performance by computational methods. A nanofluid whose temperature dependent thermophysical properties have been characterised is employed as the heat transfer fluid. As such, the study provides a systematic investigation into the impact of thermophysical properties on the performance of nanofluid-based volumetric flow receivers.

Chapter 3: Model development

In this section, the radiative and thermophysical properties of copper oxide – water nanofluid are presented. This is followed by a presentation of the volumetric flow receiver model.

3.1 Nanofluid property models

3.1.1 Radiative properties

To characterize the interaction of nanofluids with radiation, three radiative properties are required. These are the spectral scattering coefficient ($K_{s,\lambda}$), the spectral extinction coefficient ($K_{e,\lambda}$) and the spectral scattering phase function $\left(p_\lambda\left(\vec{\Omega}' \rightarrow \vec{\Omega}\right)\right)$ (Tien 1988). The coefficients represent the fraction of energy lost from a propagating wave per unit length of travel in direction $\vec{\Omega}$. The phase function specifies probability of scattering of rays into direction $\vec{\Omega}$ from any direction $\vec{\Omega}'$ resulting in energy gain by the wave. A fourth property, the absorption coefficient ($K_{a,\lambda}$) is obtained as the difference between the extinction coefficient and the scattering coefficient. It is thus sufficient to measure the first three.

Until the recent application of nanofluids to solar thermal harvesting (Tyagi, Phelan et al. 2009) little focus had gone into investigating the enhancement of radiative properties in nanofluids. Since 2010, however, a number of experiments have been performed to measure these properties through light transmittance measurements (Said, Sajid et al. 2013, Sajid, Saidur et al. 2015). Of these experiments, few have been aimed at providing characterisation data. Rather, they have been aimed at illustrating the applicability of different nanofluids to solar thermal harvesting. With limited data available, reliance has thus been on existing theoretical models to predict radiative properties. Such models have included those defined for packed and fluidized beds such as the scattering theory, the Maxwell-Garnett effective medium theory and the Discrete Dipole Approximation (DDA) approach (Sajid, Saidur et al. 2015).

The use of theoretical models requires knowledge of the optical properties of both the nanoparticles and the basefluid. These optical properties refer to the components of its complex refractive index, m, defined as

$$m = n + ik \text{ with } |m| = \sqrt{n^2 + k^2} = c_o/c \ , \qquad (3.1)$$

where c_o is the speed of light in a vacuum, c is the speed of light in the medium, n the real part of the refractive index, $i = \sqrt{-1}$ and k the imaginary part of the refractive index or the extinction index.

The optical properties of nanoparticles are derived from those of the bulk materials which are readily available in literature. However, the latter do not necessarily translate to the nano-scale. Since a nanoparticle is “smaller than the mean free path of the free electrons in the bulk material, the optical properties are modified due to boundary scattering” (Zhu, Zhang 2012, Otanicar, Taylor et al. 2009c).

The bulk optical properties can be numerically corrected for the size effect (Taylor, Otanicar et al. 2012). This is, however, not necessary for all materials as not all materials exhibit size dependent optical properties. As an example, silver (Otanicar, Phelan et al. 2010a, Taylor, Phelan et al. 2011b, Otanicar, Taylor et al. 2009c) and gold (Otanicar, Taylor et al. 2009c) have been experimentally observed to have size dependent properties. On the other hand, graphite has been observed to have no size dependence (Otanicar, Phelan et al. 2010a, Otanicar, Taylor et al. 2009c).

The optical properties of basefluids frequently employed in solar thermal harvesting such as water, Therminol VP-1, propylene glycol and ethylene glycol have been studied in the past (Brewster 1992, Hale, Querry 1973). They have also been recently investigated (Lenert, Zuniga et al. 2010b, Sani, Dell’Oro 2014, Taylor, Phelan et al. 2011b, Otanicar, Phelan et al. 2009b).

Of the several theoretical models in existence, the scattering theory has been frequently employed in nanofluids’ literature. It is based on the solutions to the electromagnetic field equations and their boundary conditions at interfaces. The solutions are defined for the absorption and scattering by a single particle in a non-participating medium under the assumptions of coherent, independent, single scattering (Hulst, Van De Hulst 1957).

Coherent scattering is defined as when the scattered light has the same frequency as the incident light (Hulst, Van De Hulst 1957). Independent scattering occurs when the scatter field from one particle forms without interaction (interference) from the scatter field of another particle (Hulst, Van De Hulst 1957). Lastly, single scattering occurs when the incident wave on each particle is that of the original beam only (Hulst, Van De Hulst 1957).

For particles with simple shapes such as spheres and cylinders, general solutions are obtained as functions of the normalized complex refractive index, $\boldsymbol{m}$ and the size parameter, α (Tien 1988). For a spherical particle, these are defined as:

$$\boldsymbol{m} = \frac{n_{np} + ik_{np}}{n_{bf}}, \tag{3.2}$$

$$\alpha = \frac{\pi D}{\lambda}, \tag{3.3}$$

where D is the particle's diameter, λ is the wavelength and the subscripts np and bf represent the nanoparticle and basefluid respectively.

In the limit $\alpha \ll 1$ and $|\boldsymbol{m}|\alpha \ll 1$, the Rayleigh limit, simplified solutions for scattering, absorption and extinction efficiencies and the phase function are obtained from the Mie approach as shown in equations (3.4) – (3.7) (Hulst, Van De Hulst 1957):

$$Q_{s,\lambda} = \frac{8}{3}\alpha^4 \left|\frac{\boldsymbol{m}^2-1}{\boldsymbol{m}^2+2}\right|^2, \tag{3.4}$$

$$Q_{a,\lambda} = 4\alpha \mathrm{Im}\left\{\frac{\boldsymbol{m}^2-1}{\boldsymbol{m}^2+2}\left[1 + \frac{\alpha^2}{15}\left(\frac{\boldsymbol{m}^2-1}{\boldsymbol{m}^2+2}\right)\frac{\boldsymbol{m}^4+27\boldsymbol{m}^2+38}{2\boldsymbol{m}^2+3}\right]\right\}, \tag{3.5}$$

$$Q_{e,\lambda} = Q_{a,\lambda} + Q_{s,\lambda}, \tag{3.6}$$

$$p_\lambda\left(\vec{\Omega}' \rightarrow \vec{\Omega}\right) = p_\lambda(\theta) = \frac{3}{4}\left(1 + cos^2\,\theta\right), \tag{3.7}$$

where θ is the polar angle, $Q_{s,\lambda}$ the spectral scattering efficiency, $Q_{e,\lambda}$ the spectral extinction efficiency and $Q_{a,\lambda}$ the spectral absorption efficiency.

Kerker (cited elsewhere (Said, Saidur et al. 2014)) quantified the limit $\alpha \ll 1$ as Rayleigh scattering equations being accurate to within 4% for $\alpha < 0.3$. For the smallest wavelength in the terrestrial solar wavelength range, $0.3\,\mu m$, this gives the maximum diameter of the spherical particle as:

$$D = \frac{\alpha\lambda}{\pi} \leq \frac{0.3(0.3*10^{-6})}{\pi} \cong 30\ nm\,. \tag{3.8}$$

As nanoparticles are defined for diameters, $D \in [0{,}100]\, nm$, the Rayleigh scattering equations can be applied. It is expected that prediction errors are dominant at short wavelengths with increase in diameter beyond $30\, nm$. Indeed, the equations have been shown to under-predict radiative properties in the short wavelength region for aluminium oxide – water and titanium oxide – water nanofluids (Said, Saidur et al. 2014, Said, Saidur et al. 2015). The presence of observed nanoparticle aggregates of sizes above $100\, nm$ was not discounted as a possible factor for the difference.

For particulate media such as the nanofluids, the absorption and scattering coefficients can be obtained from the absorption and scattering efficiencies of a single particle. This depends on the scattering regime of the system which is based on the size parameter, α and the volume fraction, ϕ. Figure 12 illustrates the independent scattering versus dependent scattering regimes.

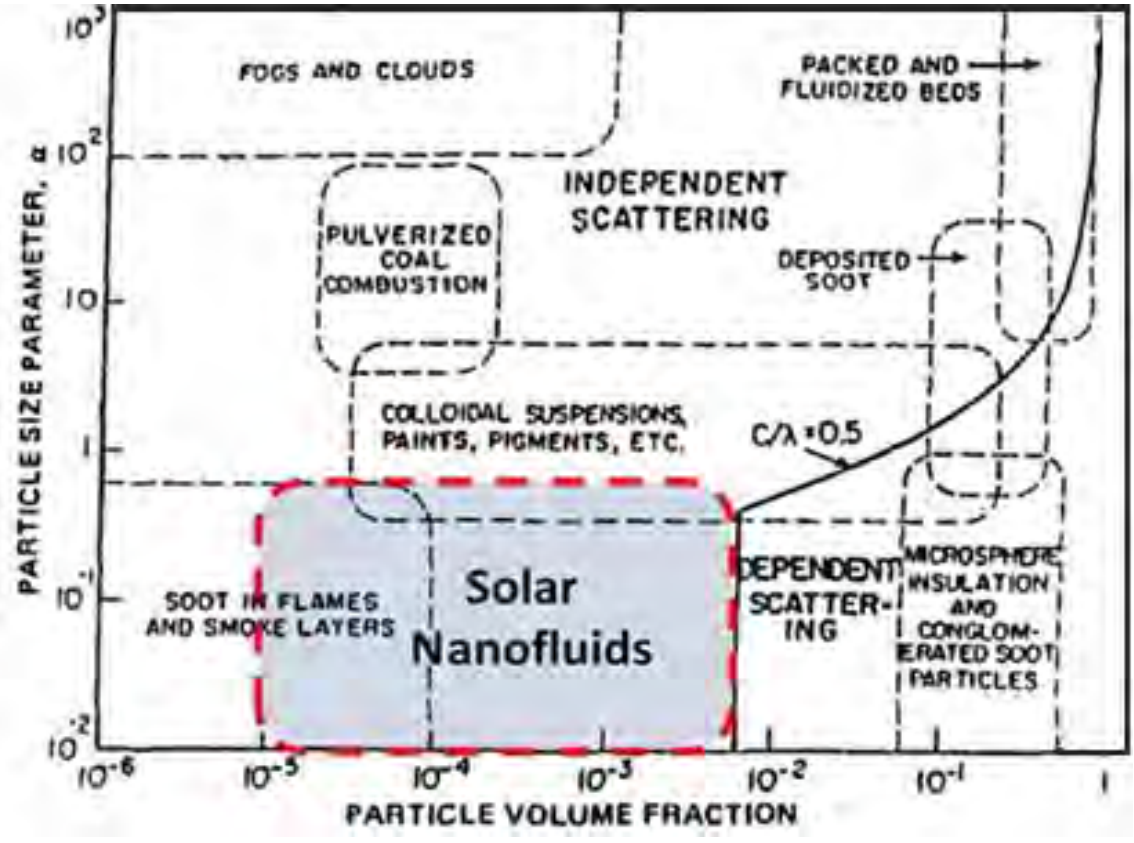

Figure 12: Illustration of independent versus dependent scattering on a scattering regime map (Taylor, Phelan et al. 2011b).

In the figure above, the demarcation line c/λ represents the ratio between the inter-particle distance, c and the wavelength, λ. As the ratio increases, the scatter field from a single particle is able to form without interference from the scatter fields of its neighbouring particles.

Dilute media can be treated as independent scattering when defined for volume fraction $\phi < 0.6\ \%$ or $c/\lambda > 0.5$ (Tien 1988). This allows for the system's energy extinction and scattering coefficients to be expressed by simple algebraic expressions of the energy extinction and scattering efficiencies of single particles as given in equation (3.9),

$$K_{i,\lambda} = \frac{3\phi Q_{i,\lambda}}{2D}\ ; \qquad (i = a, s, e), \tag{3.9}$$

where $K_{i,\lambda}$ are the energy coefficients and $Q_{i,\lambda}$ the energy efficiencies previously defined. Single scattering is also assumed to hold for low volume fractions. Otanicar, Phelan et al. (2009b) proposed the limit, $\phi < 1\%$.

Given that the basefluid absorbs, especially in the infrared region, its contribution is also incorporated. Since the basefluid is a homogeneous medium, absorption will be predominant. From its extinction index, k_{bf}, the basefluid's absorption coefficient is defined as,

$$K_{a,\lambda} = \frac{4\pi k_{bf}}{\lambda}\ . \tag{3.10}$$

Finally, a first order approximation of the extinction coefficient of the nanofluid is obtained by summing up the previously defined coefficients. This is illustrated in equation (3.11). It is valid for low volume fractions (Taylor, Phelan et al. 2011b).

$${K_{e,\lambda}}^{nf} = {K_{a,\lambda}}^{bf} + {K_{a,\lambda}}^{np} + {K_{s,\lambda}}^{np}. \tag{3.11}$$

The Rayleigh scattering model was adopted for the characterisation of copper oxide – water nanofluid. Optical properties were initially required. Those of copper oxide were available in the limited wavelength range, $0 \leq \lambda \leq 1\ \mu m$ (Palik 1998). These were assumed to be size independent. Those of water were available over the entire solar spectrum, $0.3 \leq \lambda \leq 3\ \mu m$ (Palik 1998). As such, the study was conducted in the limited wavelength range, $0.3 \leq \lambda \leq 1\ \mu m$. This range contains 72.15% of the direct normal terrestrial solar spectral flux based on the ASTM G173-03 standard (ASTM 2012).

As the wavelength interval specifications of the incident flux given by the standard and those of the optical properties from literature were different, interpolation of optical properties as a function of wavelength was done in MATLAB®. The Piecewise Cubic Hermite Interpolating Polynomial (pchip) function was used to generate shape-preserving functions from the data

obtained in the work of Palik (1988). These functions were then evaluated at the wavelength specifications of the incident flux using the MATLAB® "ppval" function that simply evaluates piecewise polynomials. The radiative properties of copper oxide – water nanofluid were thereafter obtained using the Rayleigh scattering model (equations (3.2) – (3.5) and equations (3.9) – (3.11)). These were as illustrated in Figures 13 – 15.

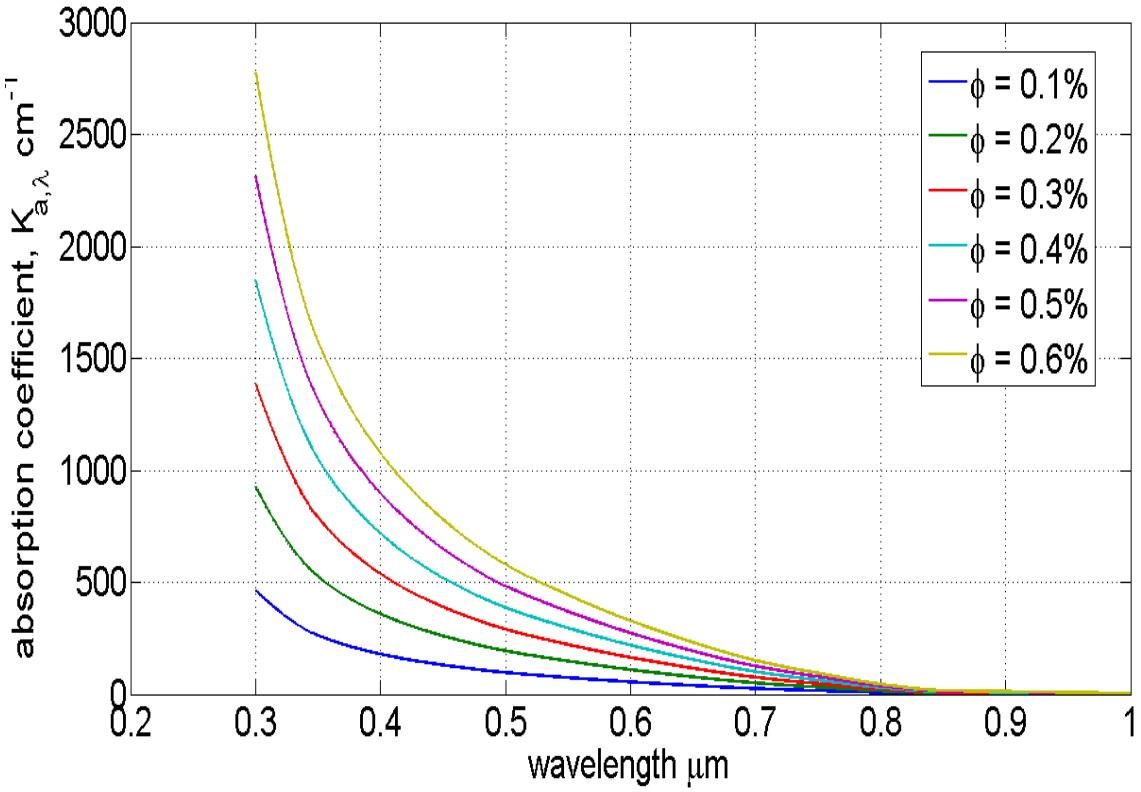

Figure 13: Absorption coefficient ($K_{a,\lambda}$) of copper oxide – water nanofluid at a fixed diameter, $D = 30\,nm$ and varying volume fractions.

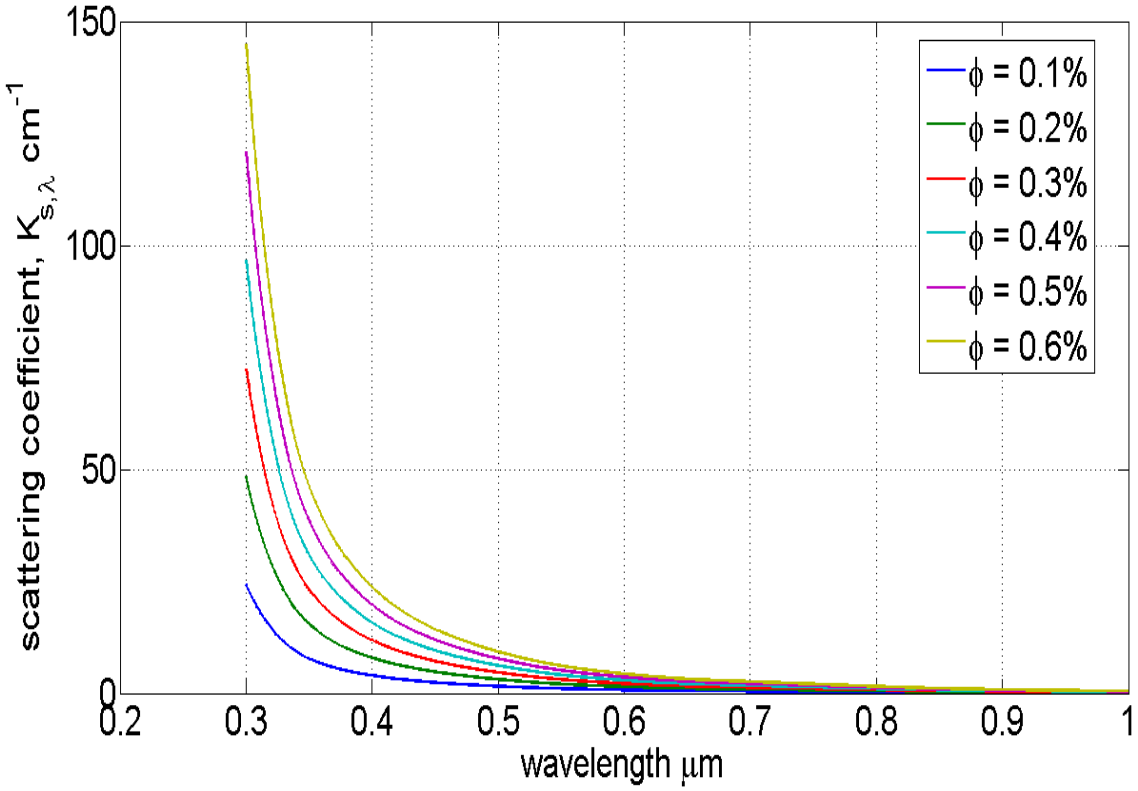

Figure 14: Scattering coefficient ($K_{s,\lambda}$) of copper oxide – water nanofluid at a fixed diameter, $D = 30\,nm$ and varying volume fractions.

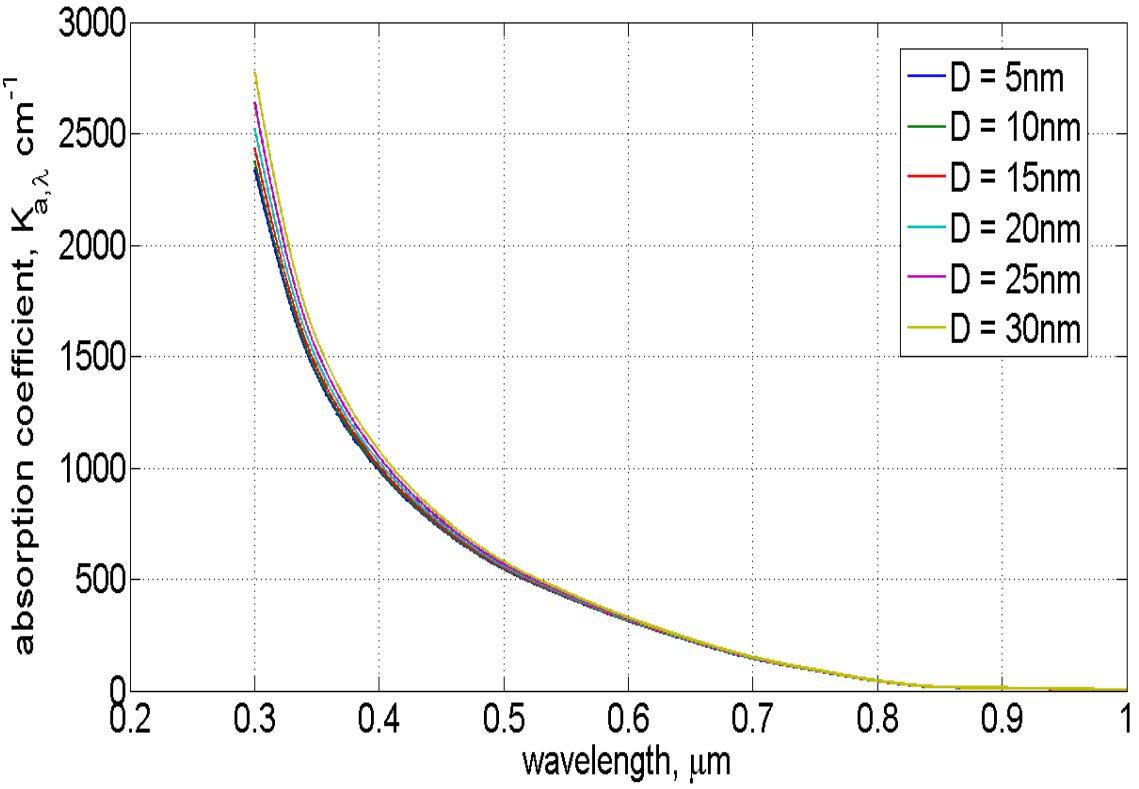

Figure 15: Absorption coefficient ($K_{a,\lambda}$) of copper oxide – water nanofluid at a fixed volume fraction, $\phi = 0.6\%$ and varying particle diameters.

It was observed from Figures 13 and 14 that copper oxide – water nanofluid had greater absorption than scattering with the former being one order of magnitude higher than the latter. In terms of the extinction coefficient (equation (3.11)), scattering contributed less than 10% of the total extinction coefficient and could thus be neglected.

It was also be observed that the nanofluid's absorption coefficient varied more with the volume fraction of nanoparticles (Figure 13) than it did with the diameter of the nanoparticles (Figure 15). In addition, peak absorption occurred at short wavelengths and thereafter reduced with increase in wavelength. This was in line with the solar spectrum distribution in which peak energies are concentrated at short wavelengths as illustrated in Figure 16. It served to confirm that copper oxide – water nanofluid is an ideal candidate for use in volumetric flow receivers.

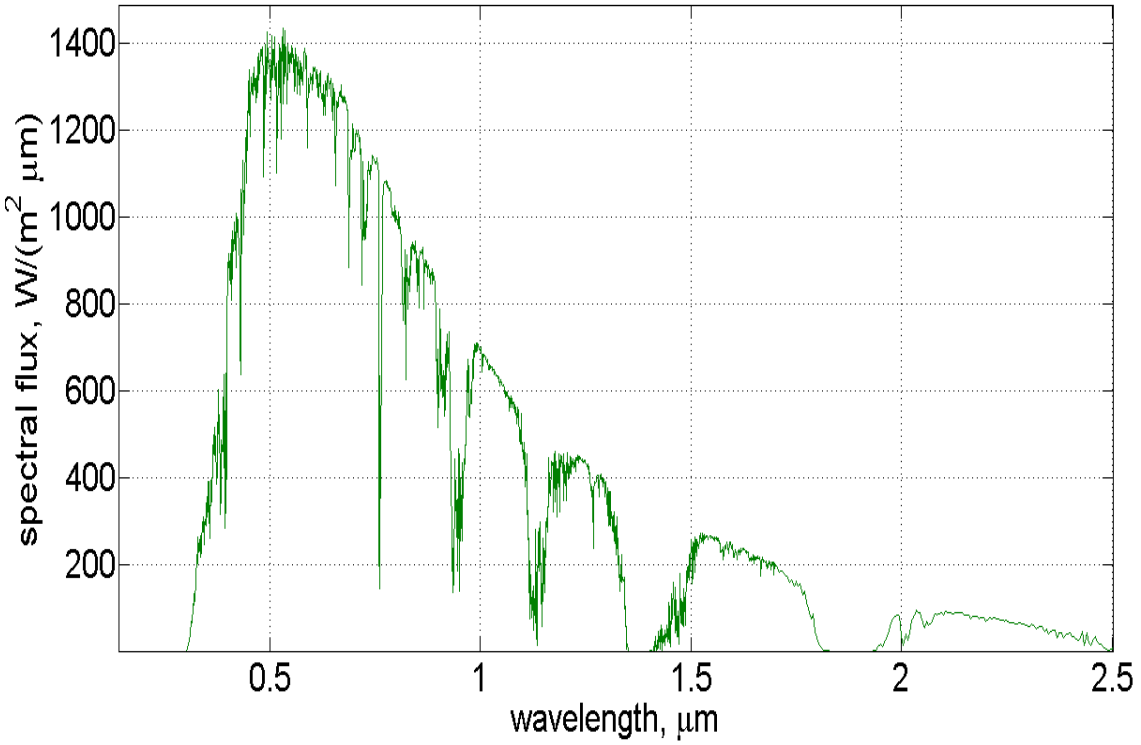

Figure 16: Direct normal terrestrial solar spectral flux (ASTM G173-03 2012, Gueymard 1995, Gueymard 2001).

3.1.2 Thermophysical properties

The thermophysical properties of a nanofluid affect the heat transfer performance of the system they are employed in. They include the density, the specific heat capacity and the thermal conductivity among others. The addition of nanoparticles into a basefluid has been seen to alter these properties to varying degrees.

Density has been observed to increase as a linear function of volume fraction at a given temperature according to the mixture rule given by equation (3.12) (Eastman, Phillpot et al. 2004, Khanafer, Vafai 2011),

$$\rho_{nf} = (1 - \phi)\rho_{bf} + \phi\rho_{np}\,, \qquad (3.12)$$

where ρ is the density and ϕ is the nanoparticle volume fraction. This mixture rule can be interpreted as a weighted average of the densities with volume fraction as the weighting factor.

Experimental validation of equation (3.12) has been done for aluminium oxide – water nanofluid (Pak, Cho 1998). Results obtained at room temperature were found to be accurate with a 0.6% maximum deviation reported at a volume fraction of 31.6%. A similar validation study was later carried out for aluminium oxide – ethylene glycol/water nanofluid with similar results obtained (Vajjha, Das et al. 2009a). The density of copper oxide – water nanofluid, employed in this study, was consequently assumed to vary according to this mixture rule.

To capture temperature dependence, a previously suggested position (Vajjha, Das 2012) was adopted; that is, density variation occurs due to the variation in density of the basefluid. Copper oxide was assumed to have a constant density of $6500\ kg/m^3$ (Vajjha, Das 2009c) while the temperature dependence of water's density was captured by an expression derived for the temperature range $0^0C \leq T \leq 150^0C$. This was given as (Popiel, Wojtkowiak 1998),

$$^1\,\rho_{bf} = 999.80 + 683.17 \times 10^{-4}\,(T - 273) - 107.40 \times 10^{-4}(T - 273)^2 + 821.41 \times 10^{-6}\,(T - 273)^{2.5} - 230.31 \times 10^{-7}\,(T - 273)^3, \qquad (3.13)$$

where T is the temperature in Kelvin and ρ_{bf} is the density of the basefluid.

[1] Equation (3.13) rounded off to 2 decimal places for display purposes.

Specific heat capacity has generally been observed to decrease with increase in volume fraction at a given temperature (Khanafer, Vafai 2011). This has been posited to be the case only when the specific heat of the nanoparticles is lower than that of the basefluid (He, Wang et al. 2012). Given that copper oxide has a lower specific heat capacity of $530\,J/\,kg\,K$ (Pantzali, Kanaris et al. 2009) as compared to that of water at room temperature ($\approx 4180\,J/\,kg\,K$), it was expected that this observation would hold.

There are several models that have been proposed to model the impact of volume fraction on specific heat capacity. These are reviewed by Shahrul, Mahbubul et al. (2014). Two are, however, frequently employed. These are,

$$(c_p)_{nf} = (1-\phi)(c_p)_{bf} + \phi(c_p)_{np}\,, \tag{3.14}$$

$$(c_p)_{nf} = \frac{(1-\phi)(\rho c_p)_{bf} + \phi(\rho c_p)_{np}}{\rho_{nf}}\,, \tag{3.15}$$

where c_p is the specific heat capacity and ρ_{nf} is defined according to equation (3.12). The first model (equation (3.14)), initially applied by Pak & Cho (1988), is based on the mixing theory. The second (equation (3.15)), proposed by Xuan & Roetzel (2000), is based on the assumption of thermal equilibrium between the basefluid and the nanoparticles (Khanafer, Vafai 2011, Shahrul, Mahbubul et al. 2014, Xuan, Roetzel 2000).

Experimental validation of the models has illustrated that the second model gives more accurate predictions. This observation was initially based on results derived for aluminium oxide – water nanofluid at 33^oC (Zhou, Ni 2008). Similar results were later reported for copper oxide – water nanofluids at 25^oC (Pantzali, Kanaris et al. 2009). Consequently, equation (3.15) was adopted for cases requiring temperature independent specific heat capacity.

Recent experimental and modelling work (Barbés, Páramo et al. 2014) has further illustrated that the temperature dependent specific heat capacity of copper oxide – water nanofluids can also be modelled by equation (3.15). It is, however, necessary to account for variation of the basefluid's specific heat capacity. The study by Barbes & co-authors was done in the temperature range, $23^0C < T \leq 64^0C$. An earlier study had reported similar results but was conducted at only three temperature points: $35^oC, 45^oC, 55^oC$ (O'Hanley, Buongiorno et al. 2012). Consequently, the thermal equilibrium model was also adopted for cases requiring temperature dependent specific heat capacity.

The specific heat capacity of the basefluid, water, was modelled by equation (3.16) below (Popiel, Wojtkowiak 1998) whereas that of copper oxide was taken as constant at $530\,J/\,kg\,K$ (Pantzali, Kanaris et al. 2009).

$$^{2}\left(c_p\right)_{bf} = 4.22 - 561.82 \times 10^{-5}(T-273) + 129.96 \times 10^{-5}\,(T-273)^{1.5} - 115.35 \times 10^{-6}\,(T-273)^2 + 4.15 \times 10^{-6}\,(T-273)^{2.5}, \qquad (3.16)$$

where T is the temperature in Kelvin and $c_{p_{bf}}$ is the specific heat capacity of the basefluid.

In subsequent sections, the variation of the density and the specific heat capacity of the nanofluid was investigated as the variation of a single parameter, the volumetric specific heat capacity $\left(\left(\rho c_p\right)_{nf}\right)$. The latter was obtained as a product of the density and the specific heat capacity of the nanofluid. It represented the amount of thermal energy required to raise the temperature of a unit volume of a substance by one Kelvin (Zhou, Wang et al. 2010). It was seen to decrease with increase in temperature and increase in volume fraction as illustrated in Figure 24.

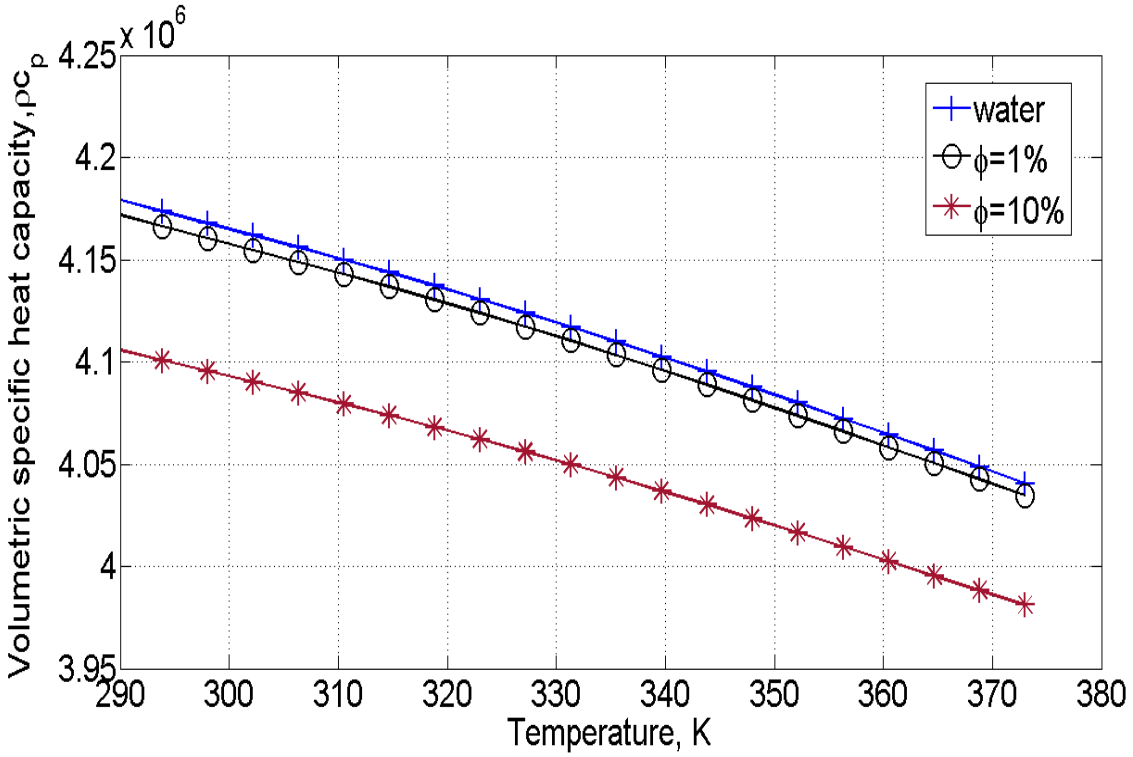

Figure 17: Volumetric specific heat versus temperature for water and copper oxide – water nanofluid at various volume fractions.

[2] Equation (3.16) rounded off to 2 decimal places for display purposes.

Thermal conductivity has received the largest share of research efforts among the properties of nanofluids given its centrality to heat transfer considerations (Wu, Zhao 2013, Lomascolo, Colangelo et al. 2015, Philip, Shima 2012). Initial interest was aroused by "anomalous enhancements of thermal conductivity" reported such as those by Eastman, Choi et al. (2001), Patel, Das et al. (2003) and Lee, Choi et al. (1999). In their study, Eastman, Choi et al. (2001) reported a 40% improvement in thermal conductivity for copper – ethylene glycol nanofluid for a volume fraction of $\phi \cong 0.3\%$ and mean diameter of $D < 10\,nm$. Patel, Das et al. (2003) reported $5\% - 21\%$ enhancement for gold – water nanofluid at an extremely low volume fraction of $\phi = 0.00026\%$ and in the temperature range $30^oC \leq T \leq 60^oC$. These were in comparison to a 20% enhancement for copper oxide – ethylene glycol nanofluid for a volume fraction of $\phi \cong 4\%$, and an area weighted mean diameter, $D \cong 23.6\,nm$ reported by Lee, Choi et al. (1999). Clearly, the anomalous enhancements made nanofluids an attractive option for heat transfer applications.

Coming out of these experiments and later ones (Murshed, Leong et al. 2005, Murshed, Leong et al. 2008) was another observation that thermal conductivity enhancements lay outside of the predictions of classical models. Such models included the Maxwell model and the Hamilton and Crosser model. These models, derived from the solution of energy equation for a stationary dilute dispersion of relatively large spheres (micro-scale), were generally seen to under-predict thermal conductivity (Khanafer, Vafai 2011). They were only slightly accurate at low volume fractions and sufficient for a first approximation.

The Maxwell model was adopted to give a conservative estimate of the thermal conductivity of copper oxide – water nanofluid. It was defined as,

$$k_{nf} = \frac{k_{np} + 2k_{bf} + 2\phi(k_{np} - k_{bf})}{k_{np} + 2k_{bf} - \phi(k_{np} - k_{bf})} k_{bf}, \qquad (3.17)$$

where k is the thermal conductivity and subscripts nf, np and bf refer to the nanofluid, nanoparticle and basefluid respectively. Temperature dependence was only slightly captured through the variation of the basefluid's conductivity given as equation (3.18) (Popiel, Wojtkowiak 1998),

$$^3\, k_{bf} = 565.03 \times 10^{-3} + 263.64 \times 10^{-5}\,(T - 273) - 125.17 \times 10^{-6}\,(T - 273)^{1.5} - 1.52 \times 10^{-6}\,(T - 273)^2 - 941.29 \times 10^{-6}\,(T - 273)^{0.5}, \qquad (3.18)$$

[3] Equation (3.18) rounded off to 2 decimal places for display purposes.

where k_{bf} is the thermal conductivity of the basefluid, ϕ is the volume fraction, and T is the temperature in Kelvin.

An experimental correlation was also adopted to give a more realistic estimate of conductivity. This correlation captured the effects of nanoparticle size, volume fraction and temperature directly and was proposed in (Koo, Kleinstreuer 2004, Koo, Kleinstreuer 2005). It was composed of two parts; a static contribution to thermal conductivity by the classical Maxwell model (equation (3.17)) and a dynamic part that considers the effect of micro-convection set up by nanoparticles moving under random Brownian motion. It was defined as,

$$k_{nf} = \frac{k_{np} + 2k_{bf} + 2\phi(k_{np} - k_{bf})}{k_{np} + 2k_{bf} - \phi(k_{np} - k_{bf})} k_{bf} + 5 \times 10^4 \beta \phi \rho_{bf} c_{p_{bf}} \sqrt{\frac{k_B T}{\rho_{np} D}}\, f(\phi, T), \tag{3.19}$$

where k is the thermal conductivity, ρ is the density, c_p is the specific heat capacity and the subscripts $bf,\ nf, np$ refer to the basefluid, the nanofluid and the nanoparticles. ϕ is the volume fraction, T is the temperature in Kelvin, D is the diameter of the nanoparticle and k_B is the Boltzmann's constant.

Functions β and $f(\phi, T)$ were based on curve fitting of experimental data. They were initially limited to the temperature range, $27^0C \leq T \leq 52^0C$ (Koo, Kleinstreuer 2004, Koo, Kleinstreuer 2005). Vajjha & Das (2009c) later modified these functions based on a larger experimental data set and extended their applicability to the temperature range, $27^0C \leq T \leq 90^0C$. These modifications were adopted for this study and can be found elsewhere (Vajjha, Das 2009c).

For equation (3.19), the temperature dependent thermal conductivity of the basefluid was given by equation (3.18). The thermal conductivity of copper oxide was taken as constant at $17.65\ W/m\,K$ (Vajjha, Das 2009c) for all cases.

The thermal conductivity of copper oxide – water nanofluid was seen to be higher than that of the basefluid, as observed from the conductivity enhancement ratio (k_{nf}/k_{bf}) in Figure 18. The Maxwell model predicted a conservative increase of about 3% while the improved Koo & Kleinstreuer correlation predicted an enhancement in the range of $7\% - 26\%$ depending on temperature. The enhancements were computed at a volume fraction of 1% and over temperature ranges for which the correlations were defined.

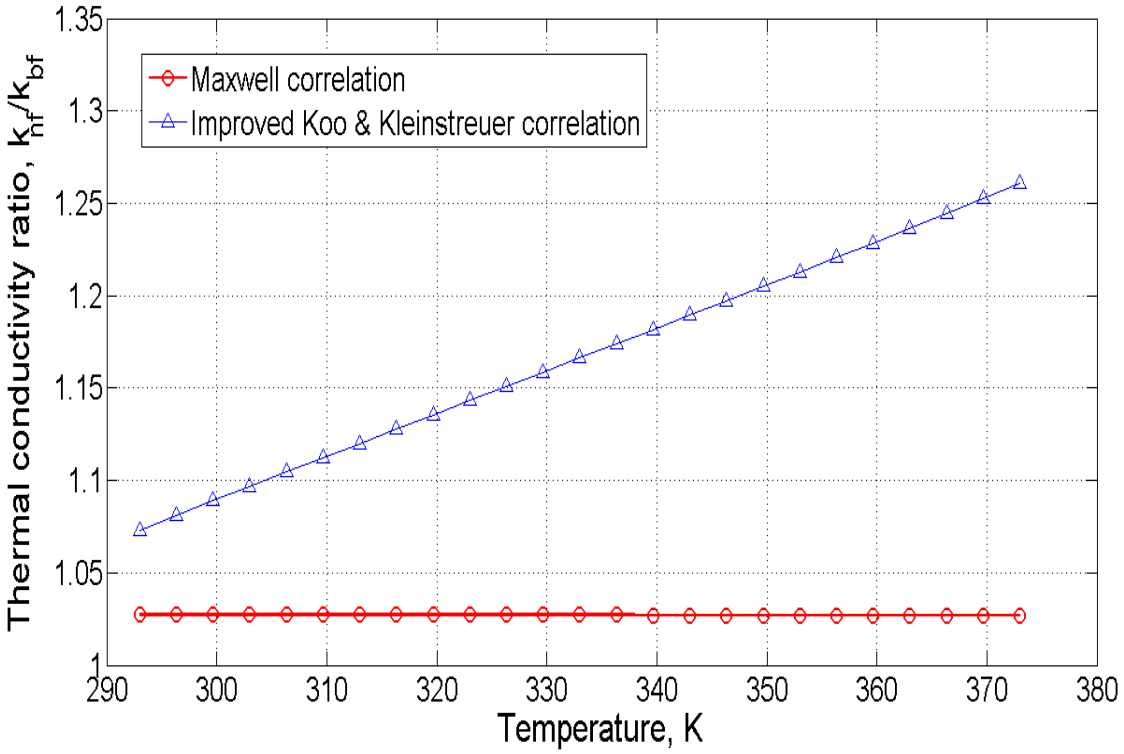

Figure 18: Comparison of thermal conductivity ratios given by the Maxwell and the Koo & Kleinstreuer correlations at a volume fraction of 1%.

The viscosity of copper oxide – water nanofluid was taken as temperature independent given the scope of the study. An experimental correlation (Nguyen, Desgranges et al. 2007) was adopted to model the variation of viscosity with nanoparticle volume fraction as given by equation (3.20),

$$\mu_{nf} = (1.475 - 0.319\phi + 0.051\phi^2 + 0.009\phi^3)\mu_{bf}\,, \qquad (3.20)$$

where ϕ is the volume fraction, μ_{nf} is the viscosity of the nanofluid and μ_{bf} is the viscosity of the basefluid.

The correlation was favoured over the classical Brinkman and Batchelor models of viscosity as Nguyen, Desgranges et al. (2007) illustrated that the classical models were insufficient for copper oxide – water nanofluid. Though defined for room temperatures, it was assumed that the correlation would hold for any inlet temperature. It was observed that at a volume fraction $\phi = 1\%$, equation (3.20) predicted a large viscosity enhancement of about 47%.

3.2 Volumetric flow receiver model

The volumetric flow receiver absorbs incident solar radiation and transfers it to a heat transfer fluid which then conducts and convects it away. A description of the model requires a description of the primary fields; intensity and temperature. The intensity of radiation is governed by the radiation transfer equation (RTE) (Ozisik 1973). The RTE caters for both the directional and the spectral properties of the intensity field, and its final form depends on the system being considered (or receiver in this case).

For this study, a parallel plate volumetric flow receiver with a linear focused concentrator was considered as shown in Figure 19. It was composed of dimensions $L \times W \times H$ (length × width × height) such that $(L, W) \gg H$. Azimuthal symmetry in the RTE boundary conditions was assumed. Additionally, negligible scattering was assumed as illustrated in section 3.1.1.

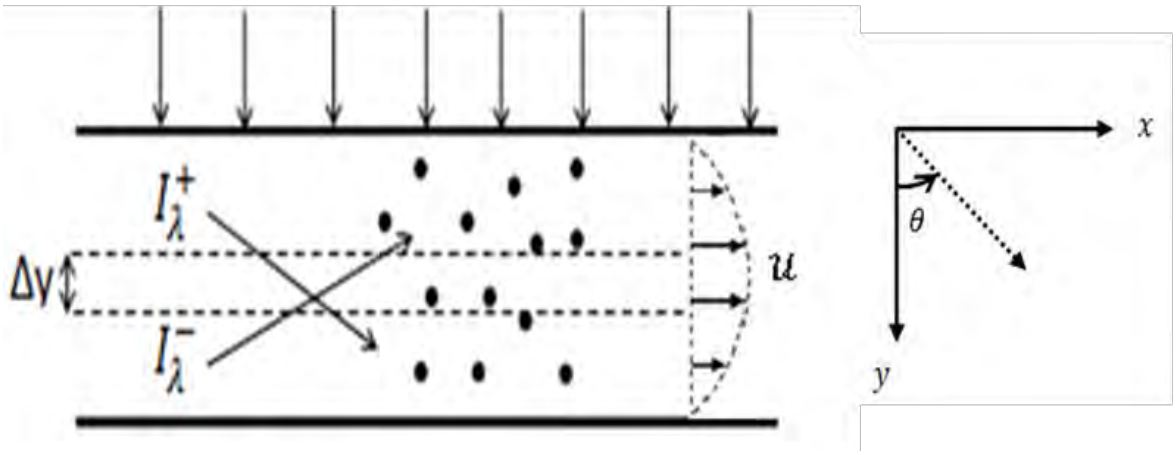

Figure 19: Volumetric flow receiver model with radiation intensity field illustrated.

The intensity field was two dimensional by virtue of the temperature field and hence its emission field being two dimensional (Kumar, Tien 1990). However, as the geometry of the model was such that the length was much larger than the height, a one dimensional approximation of the RTE was sufficient. This was because steeper intensity gradients occurred along the height than along the length (Kumar, Tien 1990). The RTE was thus defined as,

$$\mu \frac{\partial \mathrm{I}_\lambda(x,y,\mu)}{\partial y} = -K_{e,\lambda}\mathrm{I}_\lambda(x,y,\mu) + n^2 K_{a,\lambda}\mathrm{I}_{b,\lambda}\big(T(x,y)\big) \quad in\ 0 \le y \le H,$$
$$-1 \le \mu \le 1, \qquad (3.21)$$

where I_λ is the spectral intensity and $\mu = \cos\theta$ is the directional cosine. $K_{e,\lambda}$ is the nanofluid's spectral extinction coefficient, $K_{a,\lambda}$ the spectral absorption coefficient and n the real component of the spectral refractive index of the basefluid. Equation (3.21) was similar to equation (2.4) but the spectral blackbody emitted intensity $I_{b,\lambda}$ was adjusted to correct for emission into a medium other than air/vacuum (Kumar, Tien 1990).

The RTE was subject to two boundary conditions; a directly normal incident flux at the top (see Figure 16 for wavelength distribution), and either an emitting or transparent bottom boundary depending on the value of bottom wall emissivity, ϵ. These were defined as,

$$\mathrm{I}_\lambda(x,0,\mu) = \tau(\mu)\frac{J_{DN}}{2\pi}\delta(\mu-1) \qquad in\ \ \mu > 0, \tag{3.22}$$

$$\mathrm{I}_\lambda(x,H,\mu) = \epsilon n^2 \mathrm{I}_{b,\lambda}\big(T(x,H)\big) \qquad in\ \mu < 0, \tag{3.23}$$

where $\tau(\mu)$ is the glass transmissivity, J_{DN} is the top boundary spectral incident flux, $\delta(\mu-1)$ is the Kronecker delta function and other terms retain their previously defined meanings.

The energy equation (EE), governing the temperature field, was given as equation (3.24),

$$\frac{\partial(\rho_{nf}c_{p_{nf}}uT(x,y))}{\partial x} = \frac{\partial}{\partial x}\left(k_{nf}\frac{\partial T(x,y)}{\partial x}\right) + \frac{\partial}{\partial y}\left(k_{nf}\frac{\partial T(x,y)}{\partial y}\right) - \frac{\partial q_r(x,y)}{\partial y}$$
$$in\ 0 \le y \le H, \quad 0 \le x \le L, \tag{3.24}$$

where T is the temperature, k_{nf} is the nanofluid's thermal conductivity, ρ_{nf} is the nanofluid's density, $c_{p_{nf}}$ is the nanofluid's specific heat capacity and u is the nanofluid's velocity. q_r is the net radiation heat flux while $\frac{\partial q_r}{\partial y}$ is its divergence which accounts for the incoming solar radiation modeled as a volumetric heat source. These were given as equations (3.25) and (3.26) respectively,

$$q_r(x,y) = \int_\lambda 2\pi \int_{\mu=-1}^{1} \mathrm{I}_\lambda(x,y,\mu)\mu d\mu\, d\lambda, \tag{3.25}$$

$$\frac{\partial q_r(x,y)}{\partial y} = \int_\lambda K_{e,\lambda}\left[-2\pi \int_{\mu=-1}^{1} \mathrm{I}_\lambda(x,y,\mu)d\mu \ + 4\pi n^2 \mathrm{I}_{b,\lambda}\big(T(x,y)\big)\right] d\lambda\,, \tag{3.26}$$

with terms retaining their previously defined meanings.

The EE was subject to a Newton cooling boundary at the top ($y = 0$) and an adiabatic boundary at the bottom ($y = H$) defined respectively as,

$$k_{nf} \frac{\partial T(x,y)}{\partial y}\Big|_{y=0} = h(T(x,0) - T_{amb}), \tag{3.27}$$

$$k_{nf} \frac{\partial T(x,y)}{\partial y}\Big|_{y=H} = 0, \tag{3.28}$$

where h is the convective heat loss coefficient, T_{amb} is the ambient temperature and other terms retain their previously defined meanings. At the inlet ($x = 0$), a prescribed inlet temperature was assumed whereas at the outlet ($x = L$), the temperature was assumed to be fully developed. These were defined as;

$$T(x,y)|_{x=0} = T_{in}\ , \tag{3.29}$$

$$\frac{\partial T(x,y)}{\partial x}\Big|_{x=L} = 0. \tag{3.30}$$

Additionally, the velocity field was considered. It was assumed to be 1D and in the x-direction. This was in line with expectations that the highest temperatures would occur near the top of the receiver (see Figure 3) and hence density variations would not give rise to velocity in the y-direction. Thus the 1D Navier-Stokes (NS) equations were employed. These were defined as,

$$\frac{\partial(\rho_{nf} u)}{\partial x} = 0, \tag{3.31}$$

$$\frac{\partial(\rho_{nf} uu)}{\partial x} = \mu_{nf}\left(\frac{\partial^2 u}{\partial x^2} + \frac{\partial^2 u}{\partial y^2}\right) - \frac{\partial p}{\partial x}, \tag{3.32}$$

where ρ_{nf} is the nanofluid's density, u is the nanofluid's velocity, μ_{nf} is the nanofluid's viscosity and p is the pressure.

The boundary conditions of the NS were taken as a developed profile at inlet ($x = 0$), the no slip condition at top and bottom boundaries ($y = 0,\ y = H$) and a known reference outlet pressure. These were defined as,

$$u(x,y)|_{x=0} = u_{in}(y), \tag{3.33}$$

$$u(x,y)|_{y=0} = u(x,y)|_{y=H} = 0, \tag{3.34}$$

$$p(x,y)|_{x=L} = 0, \tag{3.35}$$

with terms retaining their previously defined meanings.

Chapter 4: Model implementation

In this section, the solution strategy employed to solve the volumetric flow receiver model and its implementation is presented. This is done by initially looking at the Schuster-Schwarzschild approximation to the radiation transfer equation followed by a look at the finite volume approximations to the energy and Navier Stokes equations. Thereafter, a case study from literature is simulated to validate the model and its implementation.

4.1 Approximations to the radiation transfer equation

A rigorous solution process for the model required that the RTE (equations (3.21) – (3.23)) be solved for over all directions (μ) and over all wavelengths (λ) at each point (x, y). Integration over the entire wavelength spectrum and directional space (equations (3.25) – (3.26)) would then be done to obtain total quantities that would be plugged into the EE (equation (3.24)) to solve for temperature. This implied a huge computational expense. To circumvent this, approximations to the RTE were considered (Ozisik 1973, Mengüç, Viskanta 1983).

Directionally averaged approximate models of the RTE were favoured over those that approximate the optical thickness of the medium. The idea behind the former was to break the radiation field into a number of discrete directional streams and convert the RTE into a system of differential equations. The two-flux methods were adopted. These give a first approximation and are formulated for a semi-isotropic field. They approximate the RTE with two differential equations that govern the forward and backward directional intensities.

The radiation field was decomposed into a directly transmitted component ($\mathrm{I}_{\mathrm{col},\lambda}$) resulting from the collimated incident radiation at the top, and a diffuse component ($\mathrm{I}_{\mathrm{diff},\lambda}$) resulting from emission within the nanofluid and at the bottom boundary. The directly transmitted component represented the portion of spectral intensity that penetrated the medium to a given optical depth without being attenuated by absorption. This component travelled in the downward direction only ($\mu^* > 0$). The decomposition led to a smooth angular distribution of intensity that could be approximated easily (Viskanta, Toor 1972, Viskanta, Toor 1973).

The resulting intensity field equation was given by:

$$\mathrm{I}_{\lambda}(x,y,\mu) = \mathrm{I}_{\mathrm{col},\lambda}(x,0,\mu^{*})\, e^{\left(-\frac{K_{e,\lambda}y}{\mu^{*}}\right)} + \mathrm{I}_{\mathrm{diff},\lambda}(x,y,\mu) \quad in \quad \mu^{*} > 0;\ -1 \le \mu \le 1, \tag{4.0}$$

with terms retaining their previously defined meanings. Substituting into equation (3.21) and modifying the boundary conditions gave the following:

$$\mu \frac{\partial \mathrm{I}_{\mathrm{diff},\lambda}(x,y,\mu)}{\partial y} = -K_{e,\lambda}\mathrm{I}_{\mathrm{diff},\lambda}(x,y,\mu) + n^{2}K_{e,\lambda}\mathrm{I}_{b,\lambda}\big(T(x,y)\big) \quad in\ 0 \le y \le H\ ;$$
$$-1 \le \mu \le 1, \tag{4.1}$$

$$\mathrm{I}_{\mathrm{diff},\lambda}(x,0,\mu) = 0 \quad in\ \ \mu > 0, \tag{4.2}$$

$$\mathrm{I}_{\mathrm{diff},\lambda}(x,H,\mu) = \epsilon n^{2}\mathrm{I}_{b,\lambda}\big(T(x,H)\big) \quad in\ \mu < 0, \tag{4.3}$$

with terms retaining their previously defined meanings. The diffuse field was assumed to be isotropic and was approximated by the Schuster-Schwarzschild 2-flux approximation (Ozisik 1973, Viskanta 1966). This was done by initially defining an integrated flux, j_{λ} as:

$$j_{\lambda}^{+} = \int_{0}^{1} \mathrm{I}_{\mathrm{diff},\lambda}(x,y,\mu)\ d\mu \quad in\ \ \mu > 0, \tag{4.4}$$

$$j_{\lambda}^{-} = \int_{-1}^{0} \mathrm{I}_{\mathrm{diff},\lambda}(x,y,\mu)\ d\mu \quad in\ \ \mu < 0, \tag{4.5}$$

and

$$\frac{1}{2}j_{\lambda}^{+} \approx \int_{0}^{1} \mathrm{I}_{\mathrm{diff},\lambda}(x,y,\mu)\,\mu\ d\mu \quad in\ \ \mu > 0, \tag{4.6}$$

$$-\frac{1}{2}j_{\lambda}^{-} \approx \int_{-1}^{0} \mathrm{I}_{\mathrm{diff},\lambda}(x,y,\mu)\,\mu\ d\mu \quad in\ \ \mu > 0, \tag{4.7}$$

where the factor $\frac{1}{2}$ accounts for the obliquity of the intensity.

This was followed by an integration of the diffuse field RTE over μ to obtain the following set of uncoupled linear ODEs:

$$\frac{1}{2}\frac{dj_\lambda^+(x,y)}{dy} = -K_{e,\lambda}j_\lambda^+(x,y) + n^2K_{e,\lambda}\mathrm{I}_{b,\lambda}\big(T(x,y)\big), \tag{4.8}$$

$$-\frac{1}{2}\frac{dj_\lambda^-(x,y)}{dy} = -K_{e,\lambda}j_\lambda^-(x,y) + n^2K_{e,\lambda}\mathrm{I}_{b,\lambda}\big(T(x,y)\big), \tag{4.9}$$

with boundary conditions:

$$j_\lambda^+(x,0) = 0, \tag{4.10}$$

$$j_\lambda^-(x,H) = \epsilon n^2\mathrm{I}_{b,\lambda}\big(T(x,H)\big). \tag{4.11}$$

Also, the net radiative heat flux and divergence of the net radiative heat flux were redefined as:

$$q_r = \int_\lambda \pi\big(j_\lambda^+(x,y) - j_\lambda^-(x,y)\big) + \tau(1)\,J_{DN}e^{(-K_{e,\lambda}y)}\,d\lambda, \tag{4.12}$$

$$\frac{\partial q_r(x,y)}{\partial y} = \int_\lambda K_e\big[-2\pi\left(j_\lambda^+(x,y) + j_\lambda^-(x,y)\right) - \tau(1)\,J_{DN}e^{(-K_{e,\lambda}y)} + 4\pi n^2\mathrm{I}_{b,\lambda}\big(T(x,y)\big)\big]d\lambda, \tag{4.13}$$

with terms retaining their previously defined meanings.

4.2 Finite volume method

The finite volume method was employed to approximate the EE and NS equations chiefly because it ensures conservation in the resulting weak form, as required by the strong form (Versteeg, Malalasekera 2007). The method entailed the following steps:

1. Construction of weak forms for the equations to be solved.
2. Discretisation of the domain into nodal points and their control volumes.
3. Approximation of the weak forms with nodal values.
4. Solution of the systems of equations for nodal values of the unknown variables.

The steps are now outlined with reference to a sample discretised domain as illustrated in Figure 20. The figure shows a nodal point P and its neighbouring nodal points (E, W, N, S). A control volume (dotted lines) is constructed around the nodal point P and its surfaces are also labelled (e, w, n, s).

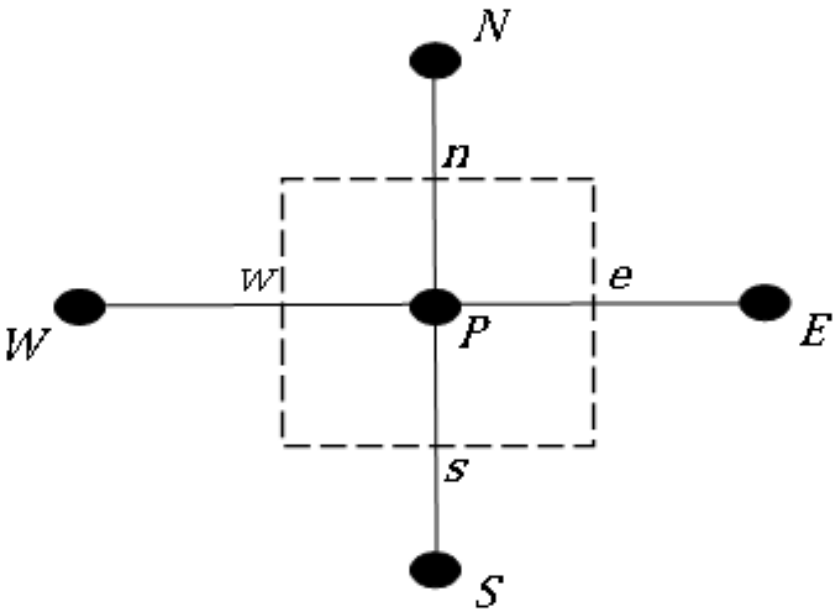

Figure 20: Sample discretised domain for the finite volume method.

The weak form of the EE was obtained by taking the integral over a control volume,

$$\frac{1}{V}\int \frac{\partial(\rho_{nf} c_{p_{nf}} uT(x,y))}{\partial x} dV = \frac{1}{V}\int \frac{\partial}{\partial x}\left(k_{nf}\frac{\partial T(x,y)}{\partial x}\right) dV + \frac{1}{V}\int \frac{\partial}{\partial y}\left(k_{nf}\frac{\partial T(x,y)}{\partial y}\right) dV - \frac{1}{V}\int \frac{\partial q_r(x,y)}{\partial y}\, dV, \tag{4.14}$$

where V is the volume of a finite control volume and other terms are as previously defined. This was followed by employing the divergence theorem and averaging the source term over the control volume to obtain,

$$\oint \rho_{nf} c_{p_{nf}} uTdA_x = \oint k_{nf} \frac{\partial T(x,y)}{\partial x} dA_x + \oint k_{nf} \frac{\partial T(x,y)}{\partial y} dA_y - \overline{\frac{\partial q_r(x,y)}{\partial y}} \Delta V, \quad (4.15)$$

where A_x and A_y are the surface areas of the control volume in the x and y directions respectively and other terms retain their usual meanings.

Similarly, the weak forms of the NS equations were obtained as:

$$\oint \rho_{nf} udA_x = 0, \quad (4.16)$$

$$\oint \rho_{nf} uudA_x = \oint \mu_{nf} \frac{\partial u}{\partial x} dA_x + \oint \mu_{nf} \frac{\partial u}{\partial y} dA_y - \overline{\frac{\partial p}{\partial x}} \Delta V, \quad (4.17)$$

where terms retain their previously defined meanings.

The integral equations (equations (4.15) – (4.17)) represented balance equations for energy, mass and momentum over a control volume. To convert them into systems of algebraic equations, the receiver domain was discretised in terms of control volumes and their nodal points following a vertex-centred approach. This provided a mesh on which to compute scalar variables. A second, forward staggered mesh was employed for the velocity discretisation. The equations were then expressed in terms of the nodal points.

To achieve this, the averaged source terms were approximated as being equal to the value at the control volume's nodal point. Surface quantities were evaluated as the average of values at neighbouring nodal points. Diffusive gradients were approximated by the central differencing method which is second order accurate. Finally, the convective terms were approximated by a bounded second order convection scheme (min-mod) with first order upwinding at the boundaries (Versteeg, Malalasekera 2007, Darwish 1993).

For a representative nodal point P on either mesh, the discretised weak forms of the EE and momentum equations took the form:

$$F_e t_P - F_w t_W = D_s(t_S - t_P) - D_n(t_P - t_N) + D_e(t_E - t_P) - D_w(t_P - t_W) + f, \quad (4.18)$$

where the subscripts e, w, n, s refer to the East, West, North and South control volume's surfaces respectively (see Figure 20). The subscripts E, W, N, S refer to the East, West, North and South neighbouring nodal points respectively (see Figure 20). F and D refer to the convective and diffusive contributions respectively with their definitions given elsewhere (Versteeg, Malalasekera 2007). t refers to the primary variables, temperature and velocity. f refers to the source terms of the EE and momentum equations, given respectively as,

$$f = -\left(\overline{\frac{\partial q_r(x,y)}{\partial y}}\right)_P \Delta V + S_{DC}, \tag{4.19}$$

$$f = -\left(\frac{\overline{\partial p}}{\partial x}\right)_P \Delta V + S_{DC}, \tag{4.20}$$

where S_{DC} is the deferred correction contribution which is defined elsewhere (Versteeg, Malalasekera 2007). Other terms retain their usual meanings.

Gathering the coefficients of the primary variable in equation (4.18), a final form of the equation was obtained as,

$$A_P t_P - A_E t_E - A_W t_W - A_N t_N - A_S t_S = f, \tag{4.21}$$

where A represents sum of coefficients from equation (4.18). Equation (4.21) was written out for each interior nodal point. For boundary nodal points, the equation was adjusted to reflect the boundary conditions given by equations (3.27) – (3.30) and (3.33) – (3.35). Some of the boundary terms were shifted to the RHS of equation (4.21) to maintain the structure of its LHS. Such terms included the contributions of the ambient temperature in equation (3.27).
Systems of algebraic equations were consequently obtained. These were expressed as matrix equations of the form $\boldsymbol{At} = \boldsymbol{f}$ with the matrix of coefficients $\boldsymbol{A}$, the variable vector $\boldsymbol{t}$, and source term flux vector $\boldsymbol{f}$. The matrices of coefficients were found to be square, sparse, non-symmetric and containing a positive diagonal.

To proceed with the solution, the coupling between pressure and velocity in the NS equations and that between the NS equations and the EE due to temperature dependent density had to be considered. Furthermore, the nonlinearities in the EE also had to be considered. These arose from temperature dependent thermophysical properties and the flux vector being temperature dependent and coupled to the solution of the RTE. The SIMPLER

algorithm (Versteeg, Malalasekera 2007) was employed in an iterative fashion as given below:

1. An initial guess was assumed for temperature (inlet temperature), velocity and pressure.
2. Using the guess/new temperature field, temperature dependent thermophysical properties were evaluated.
3. Pseudo-velocities were computed.
4. A pressure equation formulated from the discretised continuity equation and using the pseudo-velocities was solved. This gave a new pressure field.
5. The discretised momentum equation was solved using the new pressure field. This gave a new velocity field. The equation was solved iteratively due to deferred correction and convergence of inner iteration RMS residuals was taken to have occurred at a limit of 1e-4.
6. A pressure correction equation from the discretised continuity equation and using the new velocity field was solved.
7. The new velocity field was corrected to satisfy continuity.
8. The discretised energy equation was solved to obtain a new temperature field using the continuity satisfying velocity field as follows:
    8.1 The matrix of coefficients was assembled.
    8.2 The linear ODEs of the RTE (equations (4.8) – (4.11)) were evaluated exactly at each point for each wavelength. The divergence of the net radiative heat flux was then evaluated through numerical integration. In addition, the deferred correction contributions were evaluated. These gave the source term flux vector.
    8.3 The matrix equation was solved.
    8.4 Both the temperature and the EE residuals were tested for convergence. The RMS values were compared to a limit of 1e-6. If converged, the inner iterations were exited, else the program went back to step 8.2 utilising the new temperature field as the new guess.
9. The outer iteration RMS residuals for the discretised EE and NS equations were tested for convergence to a limit of 1e-6. If converged, the outer iterations were exited, else the program went back to step 2 utilising the new fields.

The implementation was done by writing code in C++. The Eigen library (Guennebaud, Jacob 2010) was used to handle sparse linear algebra. It provided an iterative stabilized bi-conjugate gradient solver with incomplete LU factorization for preconditioning. The solver was serialised; however, other aspects of the coded algorithm were parallelised using

OpenMP® (OpenMP Architecture Review Board 2011). Pre-processing was done in Trelis Pro software while post-processing was done in MATLAB® and Paraview (Ahrens, Geveci et al. 2005).

4.3 Validation

To validate the model, the work by Tyagi, Phelan et al. (2009) for aluminium – water nanofluid at volume fraction of 0.8%, a particle diameter of $5\ nm$ and a wavelength range $0 < \lambda \leq\ 3\ \mu m$ was simulated. Further specifications of the work are provided in the Appendix.

A mesh independence study was performed with five meshes generated in Trelis Pro software. The mesh specifications are given in Table 3.

Table 3: Mesh specifications for mesh independence study

Mesh number	Nodes in x-direction	Nodes in y-direction	Total nodes
1	26	151	3,926
2	51	301	15,351
3	101	601	60,701
4	201	1,201	241,401
5	281	1681	472,361

Tyagi, Phelan et al. (2009) reported an efficiency of about 74% whereas the above model gave an efficiency of 75.59% with efficiency defined according to equation (1.2). These results were those obtained from the fifth mesh as illustrated in Figure 21. The difference between this model's results and those of Tyagi, Phelan et al. (2009) was reasoned to be chiefly due to the approximation done using the MATLAB® "pchip" function. In their work, Tyagi, Phelan et al. (2009) did not specify how they approximated the optical properties to match the wavelength interval of the top boundary incident flux. As well, they did not explicitly specify what mixture rules they used for the temperature independent thermophysical models of the nanofluid. As illustrated in the Appendix, the classical models were used for this validation.

From Figure 21, it was also observed that between the fourth and the fifth mesh, an approximately 96% increase in the number of nodes (and consequently computational effort) resulted in a small efficiency decrease of 0.23%. This translated to a mean outlet temperature difference of $4 \times 10^{-4}\ K$ which was taken as insignificant for the purposes of this

study. The fourth mesh was thus taken to give mesh independent results and used for further computations.

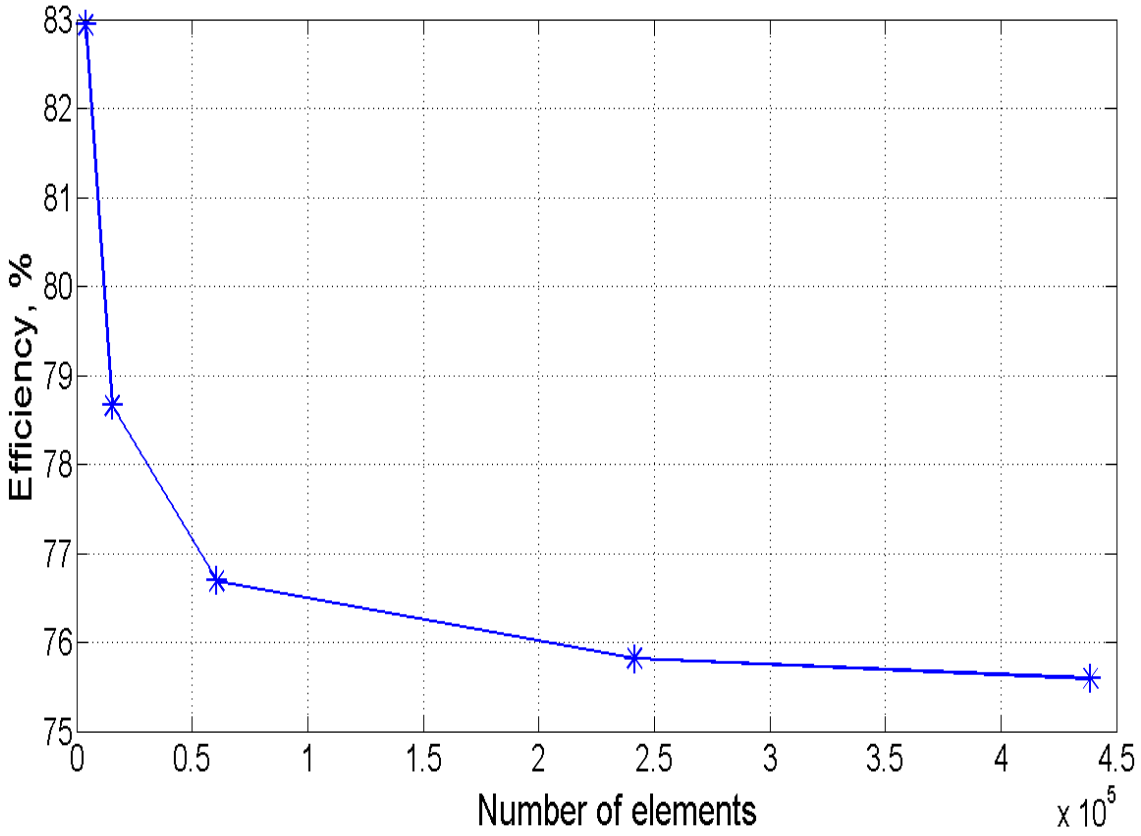

Figure 21: Mesh independence study for efficiency values predicted by the developed model.

Chapter 5: Results and discussion

In this section, the results obtained from running simulations using the models given previously are presented. This is done by initially presenting the testing regime employed and thereafter the results and a discussion of the same.

5.1 Testing regime

The influence of thermophysical properties on the performance of a volumetric flow receiver was studied by employing four testing regimes as follows:

1. Thermophysical properties constant with respect to temperature and set to the inlet temperature according to equations (3.12), (3.15) and (3.17).
2. Thermal conductivity varied with temperature while volumetric specific heat capacity was set to the inlet temperature.
3. Volumetric specific heat capacity varied with temperature while thermal conductivity was set to the inlet temperature.
4. All thermophysical properties varied with respect to temperature.

In each regime numerical experiments were performed at different concentration ratios, that is, $C = [1,\ 5,\ 10,\ 20,\ 30,\ 40,\ 50,\ 100,\ 150]$. This was done to obtain the performance of the receiver at different temperatures. The first regime was based on an assumption commonly employed in literature (Lenert, Wang 2012, Tyagi, Phelan et al. 2009) whereas the other regimes have not been previously investigated. The nine experiments run in the first regime served as control experiments, providing a basis to compare results obtained in the other regimes.

In the second regime, a total of eighteen numerical experiments were run to test the receiver performance with the different temperature dependent conductivity models. Nine experiments were run for each of the conductivity correlations. An equally huge number of numerical experiments were run in the fourth regime. In the third regime, nine numerical experiments were run to test the influence of the single parameter.

The nanofluid employed was copper oxide – water nanofluid at a volume fraction, $\phi = 1\%$, a diameter, $D = 29\ nm$ and a temperature range, $308 \leq T < 380\ K$. The study was conducted in the limited wavelength range, $0.3 \leq \lambda \leq\ 1\ \mu m$. These limitations were in accordance to

data obtained in literature and presented in section 3.1. The top incident flux was given by the terrestrial solar spectrum (Figure 16). Other specifications were as given in Table 4 below.

Table 4: Specifications for testing regime.

Item	**Value**
Mean inlet velocity (parabolic profile), u	0.5 m/s
Inlet mass flow rate, $\dot{m}$	0.629 kg/s
Inlet temperature, T_{in}	308 K
Ambient temperature, T_{amb}	298 K
Length, L	1 m
Width, W	1 m
Height, H	1.2 mm
Convective heat loss coefficient, h	20 W/(m^2 K)
Incident solar flux, G	649.43 W/m^2
Concentration ratios, C	1 – 150
Glass transmissivity, τ	0.8
Bottom wall emissivity, ϵ	0

The receiver performance was monitored in terms of efficiency and temperature development with the former defined according to equation (1.2). The impact of thermophysical properties on these measures of performance was investigated. In addition, a parametric study was later conducted to evaluate the impact of parameters such as the inlet temperature, mass flow rate and bottom wall emissivity.

5.2 Volumetric heat release profile

The volumetric heat release profile refers to the spatial distribution of the source term to the energy equation as given by equation (4.13). It was obtained by solving the radiation transfer equation and is illustrated in Figure 22, derived from data obtained at the outlet of the receiver. Similar values and figures were obtained elsewhere within the volume of the receiver. It was reasoned that the temperature dependent emission terms in equation (4.13) were not significant in comparison to the incident flux term for the temperature range and the wavelength range considered.

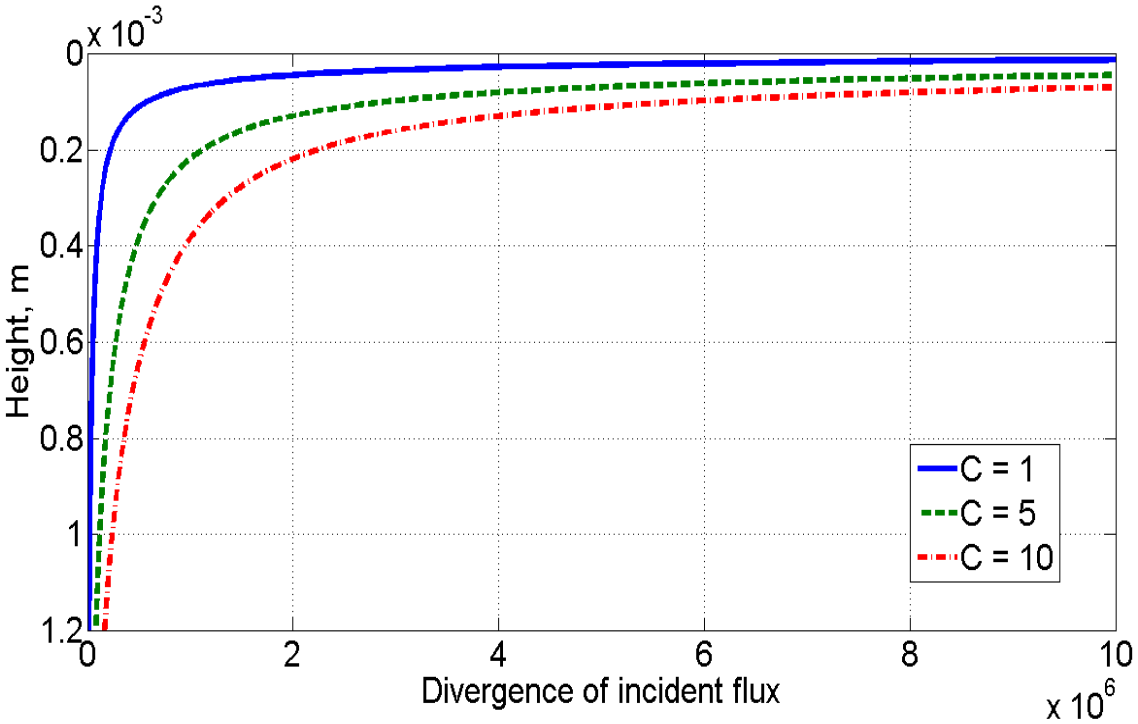

Figure 22: Divergence of incident flux across the height of the receiver for different concentration ratios.

Figure 22 illustrated an exponential decrease in the divergence of incident flux with increase in height from the top wall. A greater portion of the energy was concentrated in the top layers of the fluid as compared to the bottom layers. At a volume fraction of $\phi = 1\%$ and a diameter of $D = 29\,nm$, the nanofluid was largely opaque to solar radiation with absorption of the same occurring within the top layers.

It was also observed that an increase in concentration ratio resulted in an increase of energy availed at any given height. Again, the impact of this was greater in the top layers of the receiver as compared to the bottom layers. It was thus generally expected that greater temperatures would be attained for higher concentration ratios and peak temperatures would develop at the top of the receiver.

5.3 Impact of temperature dependent conductivity

The thermal conductivity of copper oxide – water nanofluid was predicted to be higher than that of the basefluid, as observed in Figure 18. The Maxwell model (equation (3.17)) predicted a conservative increase of about 3% whereas the improved Koo & Kleinstreuer correlation (equation (3.19)) predicted an increase in the range of $7\% - 26\%$. A sample

spatial distribution of thermal conductivity was obtained as illustrated in Figure 23 for the improved Koo & Kleinstreuer correlation at a concentration ratio $C = 150$.

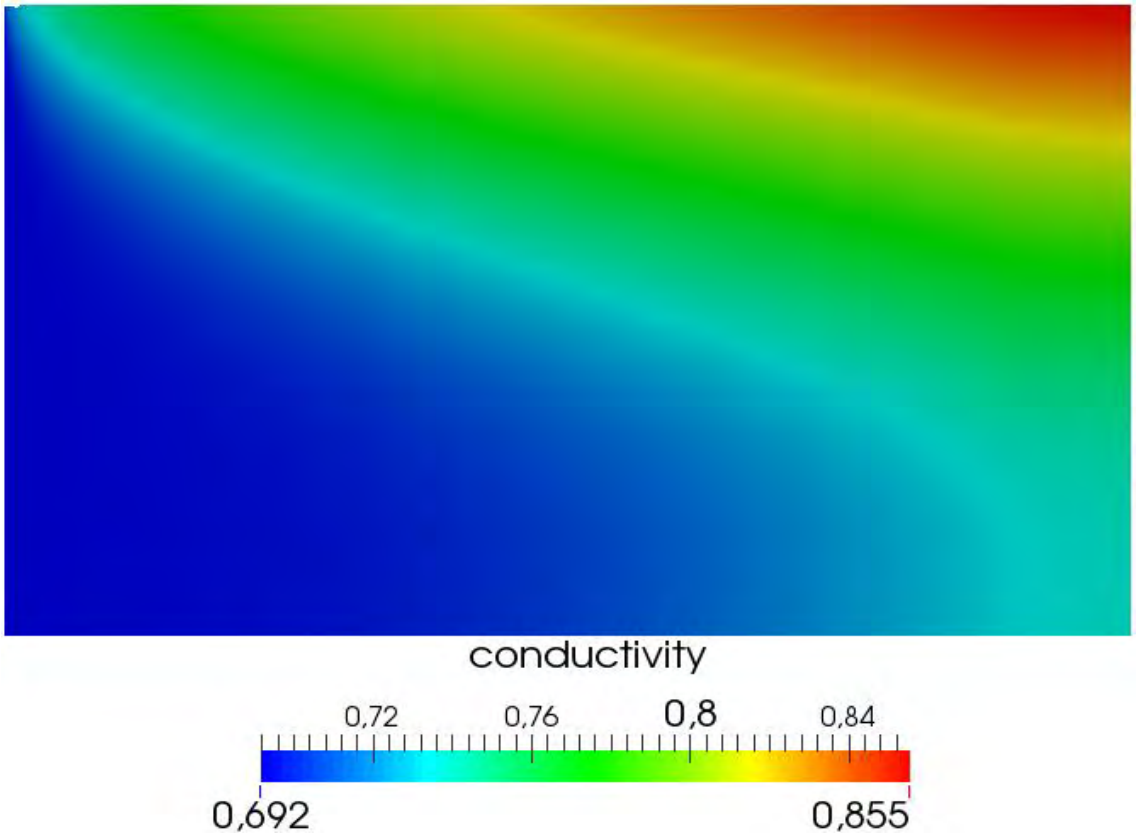

[4]Figure 23: Spatial distribution of thermal conductivity within the receiver for the improved Koo & Kleinstreur correlation at a concentration ratio, $C = 150$.

Higher values of thermal conductivity were obtained in the top layers of the receiver as compared to the bottom layers. This was indicative of the temperature development within the receiver, with greater temperatures being achieved near the top. This was expected given the heat release profiles illustrated in the previous section.

For the control cases, a constant conductivity value of $0.642\, W/(m\, K)$ was maintained throughout the domain. This value was $7\% - 33\%$ lower than that predicted by the improved Koo & Kleinstreuer correlation as illustrated in Figure 23. These differences were seen to translate to the temperature development within the receiver as illustrated in Figure 24.

[4] Figure's axis orientation similar to that given in Figure 19.

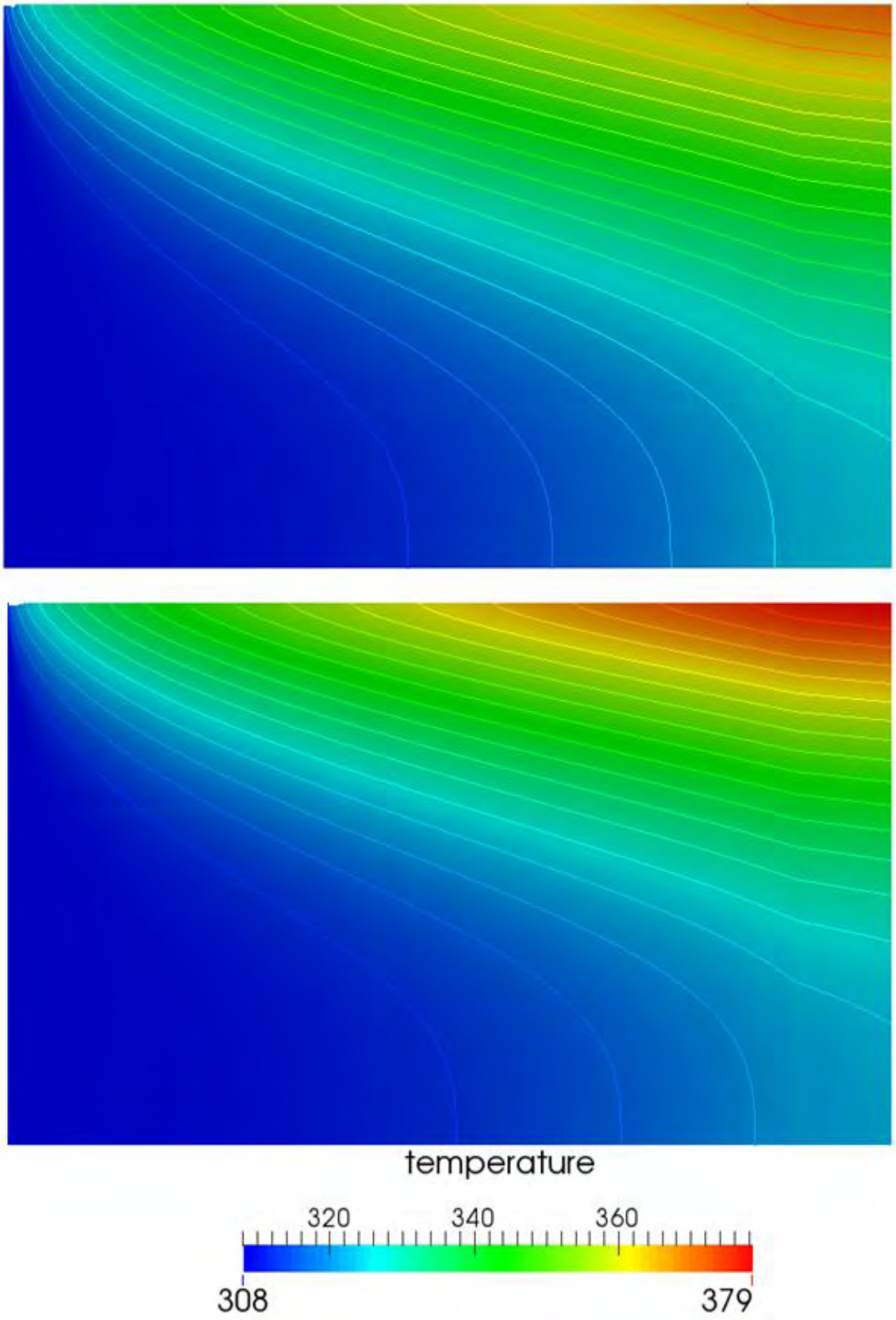

[5]Figure 24: Temperature development within the receiver for varying conductivity (top) versus constant conductivity (bottom), both at a concentration ratio, $C = 150$. Conductivity varies according to the improved Koo & Kleinstreuer correlation for the top case.

[5] Figure's axis orientation similar to that given in Figure 19.

Higher temperatures were obtained for the control cases with constant conductivity as compared to those obtained in the varying conductivity cases. From the sample cases illustrated in Figure 24, temperatures were observed to peak at $378.55\ K$ for the former case against a peak of $370.88\ K$ for the latter case. These peak temperatures were located at the top right corner (outlet).

A second metric, the mean top wall temperature, was also used to confirm this as illustrated in Figure 25. It was observed that the highest mean top wall temperatures were attained for the constant conductivity control cases. Cases with conductivity varying according to the Maxwell correlation predicted temperatures similar to those of the control experiments. Those with conductivity varying according to the improved Koo & Kleinstreuer correlation predicted the lowest temperatures.

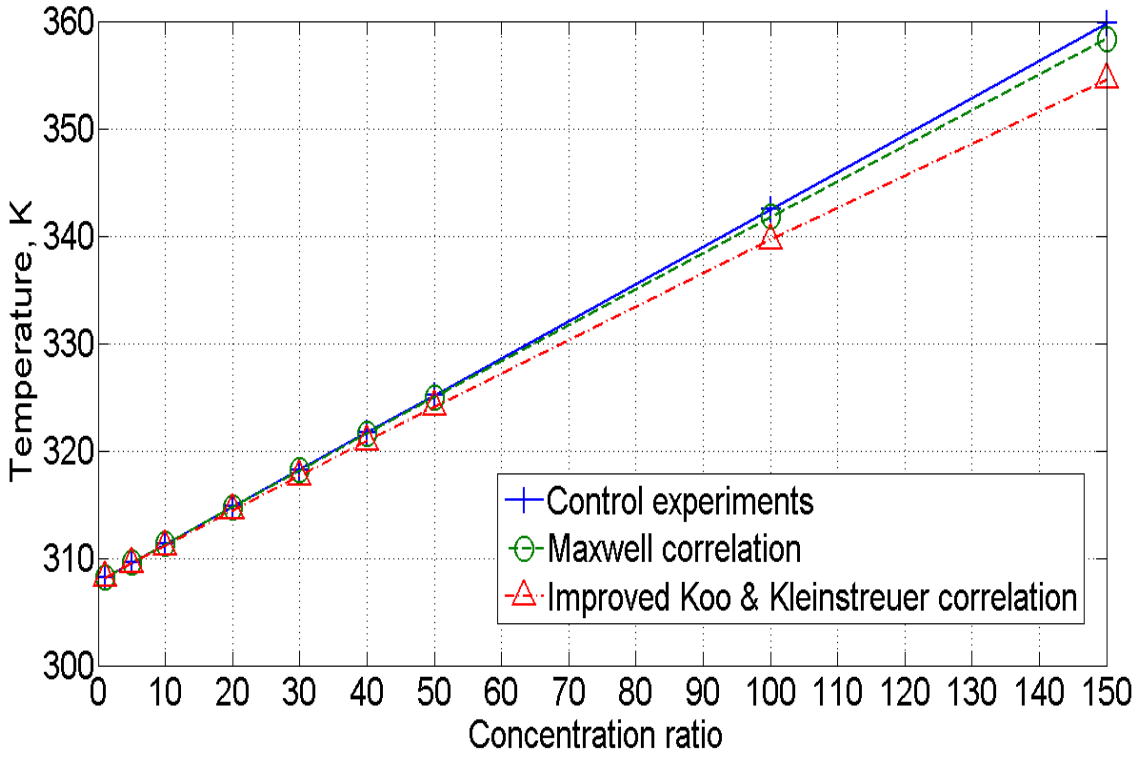

Figure 25: Comparison of mean top wall temperatures for temperature dependent conductivity cases versus the temperature independent control case.

It was noted from the figure above that the difference in mean top wall temperatures was negligible at small concentration ratios ($C < 50$). This difference, however, increased with increasing concentration ratios. At a concentration ratio of 150, absolute mean top wall temperature differences of $1.47\ K$ and $5.22\ K$ were obtained for the cases with the Maxwell and the improved Koo & Kleinstreuer correlations, respectively, over the control case.

A plot of temperature profiles at the receiver's outlet (Figure 26) illustrated that temperature development was more diffuse in the cases with varying conductivity. It was observed that for the control cases, steeper temperature gradients occurred along the height of the receiver. Cases employing the Maxwell correlation for conductivity gave similar temperature profiles whereas those employing the improved Koo & Kleinstreuer correlation gave the least temperature gradients along the receiver's height. In the latter cases, development of lower peak temperatures at the top was accompanied by development of slightly higher temperatures at the bottom.

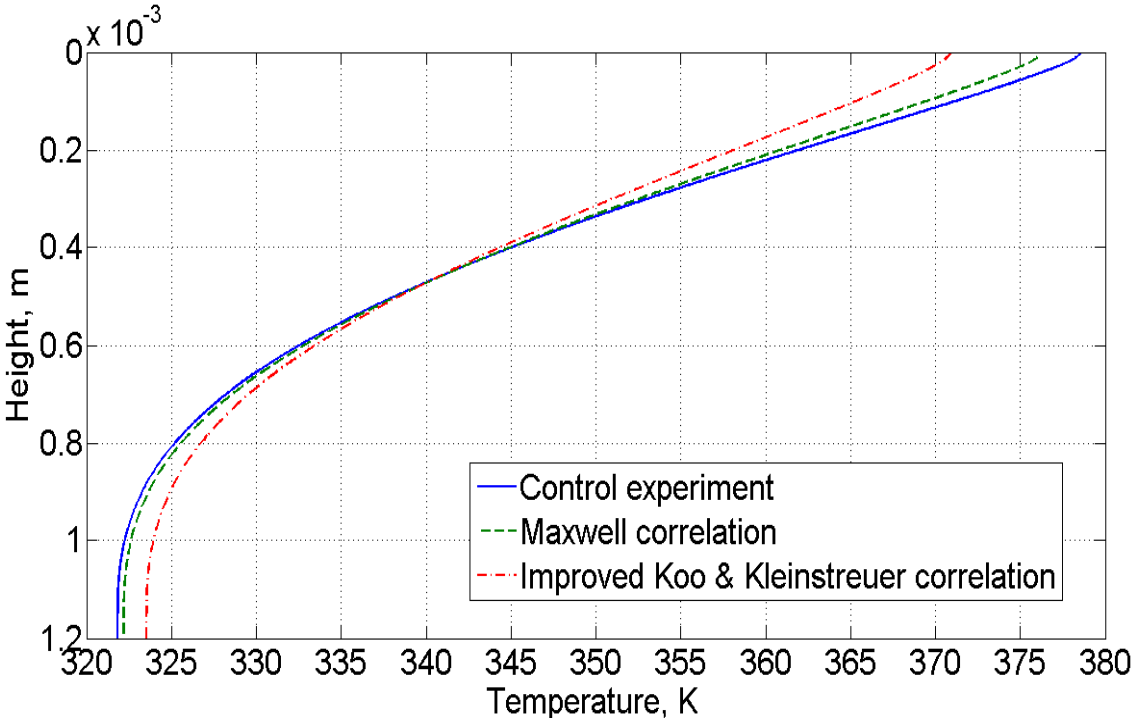

Figure 26: Comparison of outlet temperature profiles for temperature dependent conductivity cases versus the temperature independent control case. Concentration ratio, $C = 150$.

Despite the observed differences in prediction of temperature development within the receiver, it was seen that the mean outlet temperatures and hence efficiencies (equation (1.2)) were largely similar in all cases as illustrated in Figure 27. A maximum absolute difference of 1.34% was observed in the efficiencies of the control case and the varying conductivity case (according to the improved Koo & Kleinstreuer correlation) at a concentration ratio of 150. This translated to an absolute mean outlet temperature difference of $0.53\ K$.

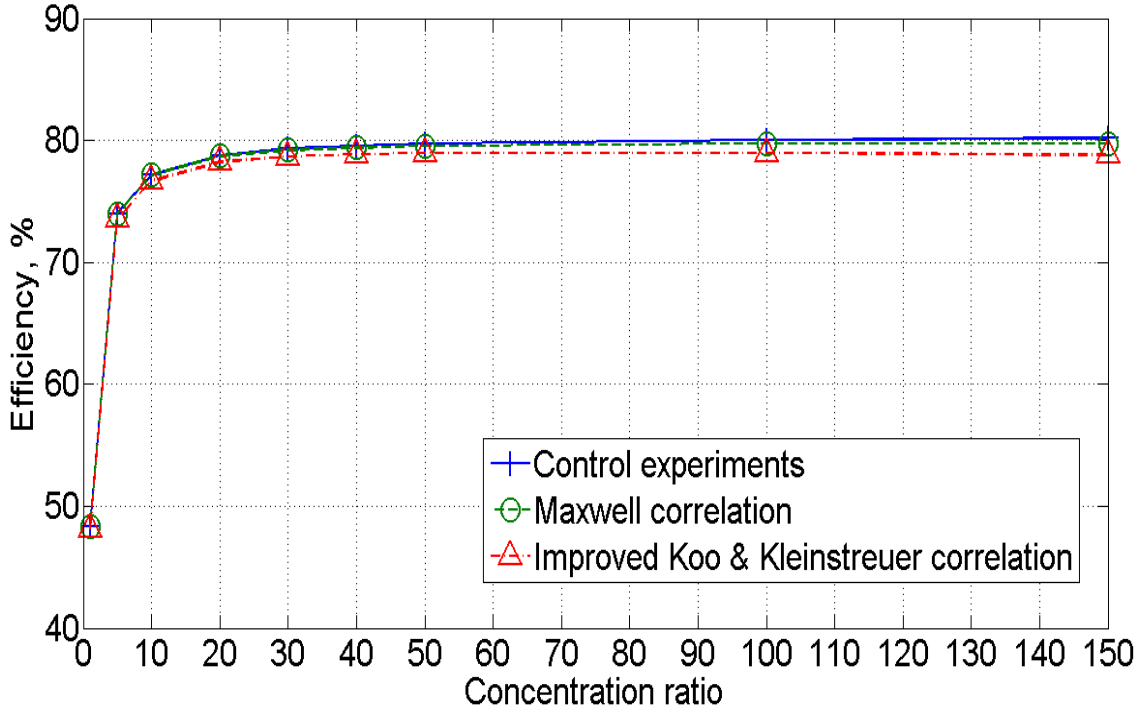

Figure 27: Comparison of receiver efficiencies for temperature dependent conductivity cases versus the temperature independent control cases.

It was reasoned that conductivity in the system served solely to diffuse the amount of energy that had already been absorbed. Thus for low constant thermal conductivity values, the energy that was largely absorbed near the surface was retained near the surface resulting in higher surface temperatures. The presence of varying conductivity allowed for this energy to be more evenly diffused. The Maxwell correlation with its conservative conductivity enhancements (about 3%) resulted in minimum energy diffusion, similar to the constant conductivity cases. The improved Koo & Kleinstreuer correlation with its high conductivity enhancements (about $7\% - 26\%$) resulted in greater energy diffusion resulting in lower peak temperatures at the top and higher temperatures at the bottom.

From the foregoing, it was concluded that thermal conductivity enhancements had no major effect on efficiency. This position was contrary to that proposed by (Otanicar, Phelan et al. 2010a) that thermal conductivity enhancements contributed to increased efficiency in receivers. It was, however, noted that conductivity enhancements affect the development of peak temperatures and temperature gradients along the receiver height with the impact growing with increase in concentration ratio.

5.4 Impact of temperature dependent volumetric specific heat capacity

The volumetric specific heat capacity, a product of density and specific heat capacity, was predicted to decrease with an increase in temperature as illustrated in Figure 17. A sample spatial distribution of the same was obtained as illustrated below:

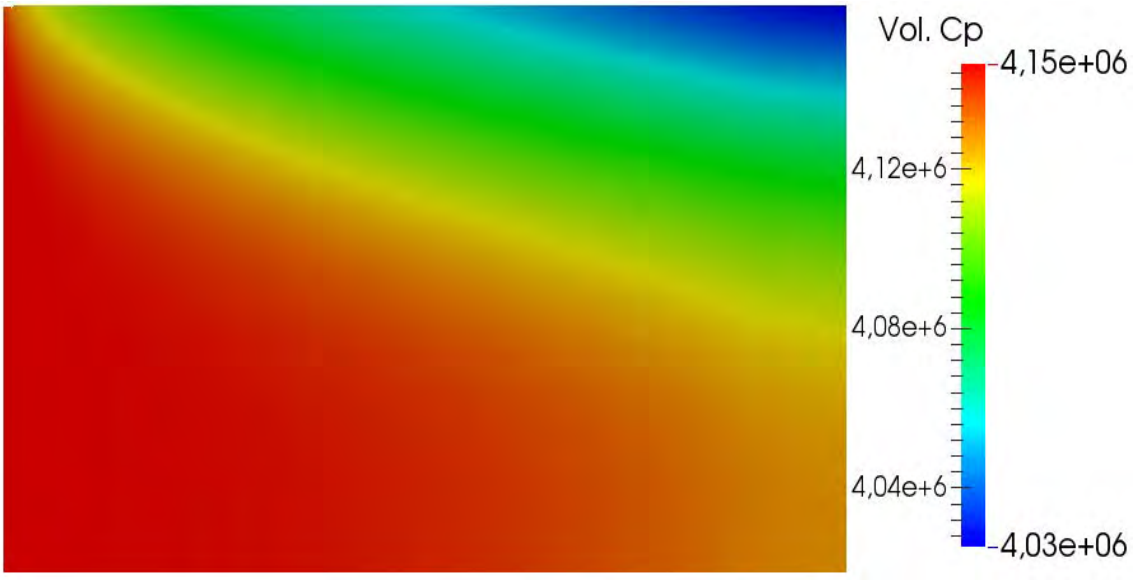

[6]Figure 28: Spatial distribution of volumetric specific heat capacity within the receiver for a concentration ratio, $C = 150$.

Figure 28 showed that the lowest values of volumetric specific heat capacity occurred in the top layers of the receiver, indicative of higher temperatures in the region. These values represented an approximately 3% drop in volumetric specific heat capacity when compared to values at the inlet. Given Figure 28 represented the maximum concentration ratio; the 3% drop thus represented the maximum drop in volumetric specific heat capacity observed.

These small changes translated to temperature development within the receiver that was largely similar to that of the control experiments with constant properties (see Figure 24). Maximum temperature differences were observed at a concentration ratio of 150 with absolute differences in the mean top wall and peak temperatures of $0.42\,K$ and $0.55\,K$ respectively. In terms of efficiency, a maximum difference of about 1% was observed as illustrated in Figure 29.

[6] Figure's axis orientation similar to that given in Figure 19.

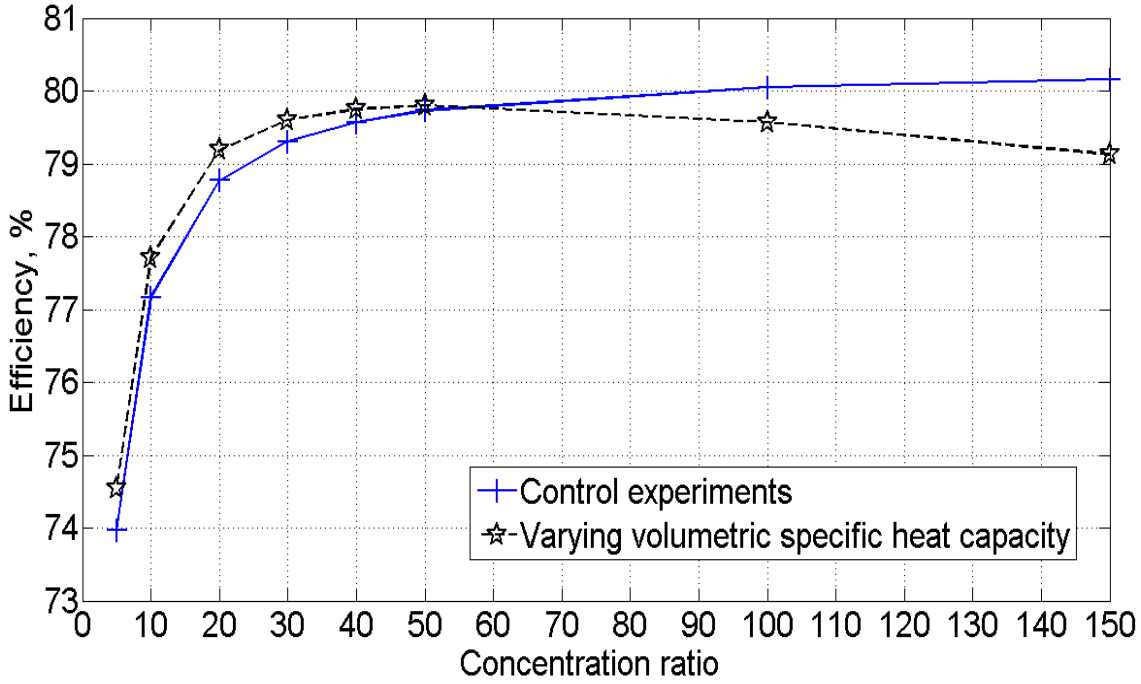

Figure 29: Comparison of receiver efficiencies for temperature dependent volumetric specific heat capacity cases versus the temperature independent control cases.

It was also observed that there was slight flow acceleration towards the outlet of the receiver. The magnitude of this increased with increase in concentration ratio as illustrated in Figure 30. This was reasoned to be the result of density decreasing with increase in temperature.

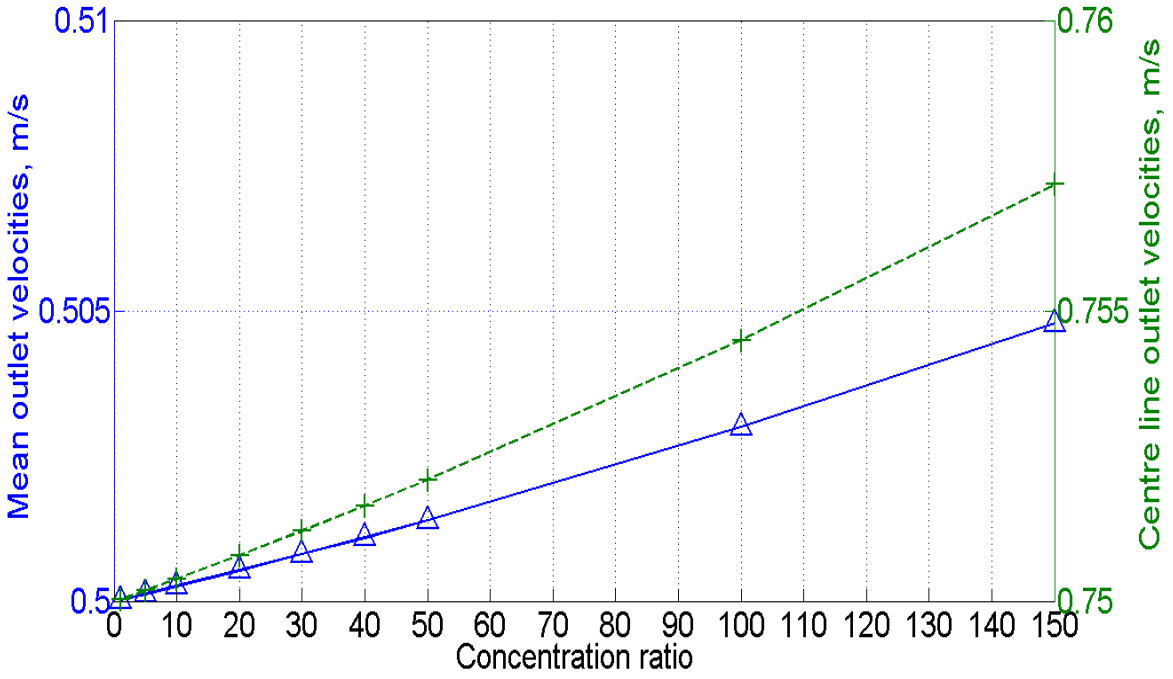

Figure 30: Mean outlet velocity (left) and centre line outlet velocity (right) versus concentration ratios.

Given that flow acceleration results in less residence time for fluid in the receiver thus less time for temperature development (Kaluri, Dattarajan et al. 2012), it was observed that this may explain the efficiency trends observed in Figure 29. The control experiments indicated a decelerating increase in efficiency with increase in concentration ratio beyond $C = 50$. The cases with varying volumetric specific heat capacity showed a definite decrease in efficiency. Though a small difference in efficiency (about 1%) was observed at a concentration ratio of 150, extrapolation of Figure 29 to higher values of concentration ratio (≈ 1000) would result in a growing difference. Thus, it was deemed reasonable that flow acceleration towards the outlet due to decreasing density led to lower outlet temperatures than could be achieved. This resulted in lower efficiencies beyond a critical value of concentration ratio.

5.5 Parametric study

A parametric study was conducted to investigate the effect of parameters such as the inlet temperature, mass flow rate and bottom wall emissivity on the performance of the receiver. Both the conductivity and the volumetric specific heat capacity were varied with temperature. It was necessary to initially establish the performance of the receiver with all thermophysical properties varied as results reported in the previous sections had either of the properties held constant. Efficiency was seen to vary according to Figure 31.

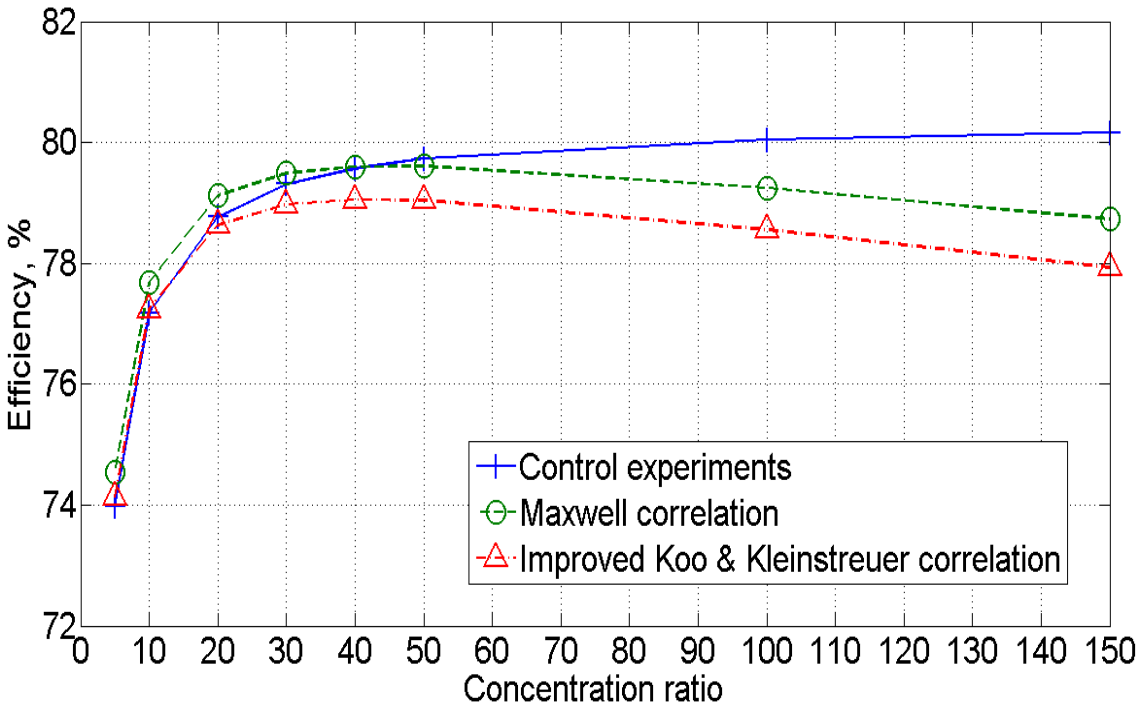

Figure 31: Receiver efficiencies for cases with temperature dependent thermophysical properties including different conductivity correlations versus control experiments.

Figure 31 illustrated that at low concentration ratios (< 50), the use of temperature dependent thermophysical properties predicted efficiencies that were similar to the control cases. Efficiency differences were all below 1%. Similarly, differences in maximum and mean top wall temperatures were small, peaking at about $1.5\ K$ and $1\ K$ respectively.

At larger concentration ratios, a difference in efficiency trends was observed. The control cases predicted a continuous increase in efficiency that peaked at about 80% whereas the cases with temperature dependent properties predicted a decreasing efficiency. A maximum difference in efficiency of 2.2% was observed at a concentration ratio of 150. Differences in maximum and mean top wall temperatures peaked at $8\ K$ and $5.5\ K$ respectively. These differences were expected to grow with increasing concentration ratio.

From the foregoing, it was concluded that at low concentration ratios, it was sufficient to use temperature independent properties set to the inlet temperature. At larger concentration ratios, however, the use of this assumption resulted in an over-prediction of efficiency arising from a failure to capture flow acceleration due to density changes. In addition, temperature development was not aptly predicted due to a failure to capture the diffusive effects of enhanced conductivity. It was thus necessary to use temperature dependent properties.

Khullar, Tyagi et al. (2013) collapsed the two variables investigated above into one, the thermal diffusivity, and illustrated that the receiver efficiency did not vary significantly with changes in the thermal diffusivity of the basefluid, Therminol VP1. Their results were based on evaluating the performance of the receiver with diffusivity set to three different inlet temperatures. This was similar to the control experiments run above and as such they failed to capture flow acceleration and its effects on efficiency.

It was interesting to note that whereas the thermal responses of Therminol VP1 and water were different, the response of efficiency to conductivity (and hence diffusivity) was similar. The conductivity of Therminol VP1 was seen decrease with increase in temperature while that of water increased. Despite this difference, efficiency was found to be largely insensitive to enhanced conductivity. These observations were contrary to an earlier proposition (Otanicar, Phelan et al. 2010a).

5.5.1 Impact of mass flow rate

It was observed that an increase in inlet mass flow rate increased efficiency as illustrated in Figure 32. This increase in efficiency was not, however, due to an increase in mean outlet temperature according to equation (1.2). As observed in Figure 33, an increase in mass flow rate resulted in a decrease in temperatures within the receiver due to less residence time for temperature development. At a concentration ratio of 30, there was a roughly $22\,K$ and $48\,K$ decrease in mean outlet temperatures for an increase in mass flow rates from $0.126\,kg/s$ to $0.629\,kg/s$ and $0.063\,kg/s$ to $0.629\,kg/s$ respectively. Mean top wall temperatures dropped by about $13\,K$ and $27\,K$ respectively. Due to this inverse relation, fewer experiments were carried out at low mass flow rates in keeping with the maximum temperatures allowed for this study.

A positive consequence of the lower temperatures at higher mass flow rates was the lowered convective heat loss from the top wall of the receiver (equation 3.27). This resulted in the higher efficiencies reported in Figure 32.

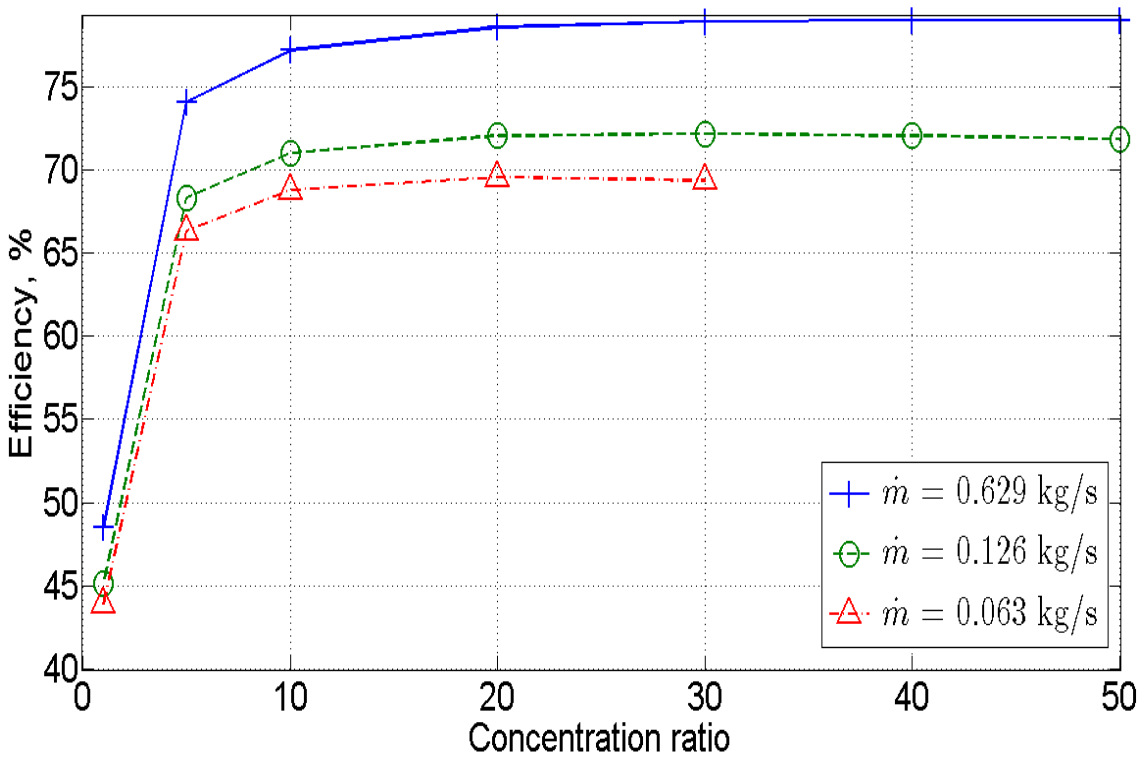

Figure 32: Receiver efficiencies for different inlet mass flow rates. All properties varying with conductivity evaluated according to the improved Koo & Kleinstreuer correlation.

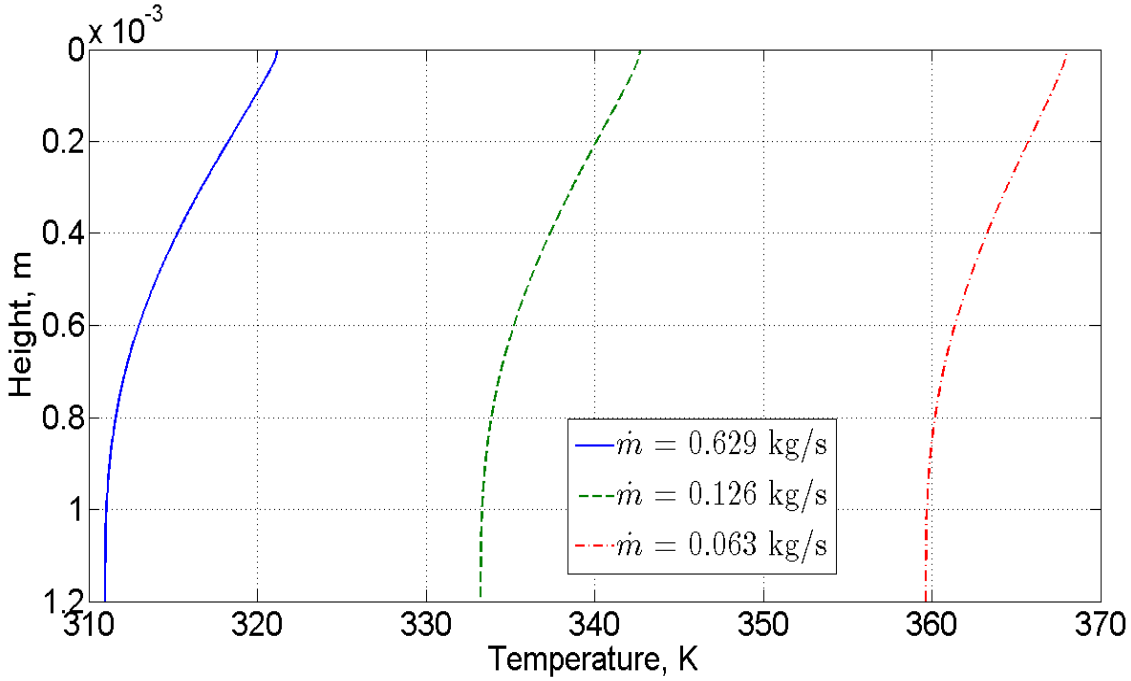

Figure 33: Outlet temperature profiles for different inlet mass flow rates at a concentration ratio of 30. All properties varying with conductivity evaluated according to the improved Koo & Kleinstreuer correlation.

It was also observed that lower mass flow rates resulted in smaller temperature drops along the height of the receiver. This was illustrated in Figure 34, obtained by normalising data from Figure 33. It was deemed that this was largely due to enhanced conductivity arising from higher temperatures at lower mass flow rates.

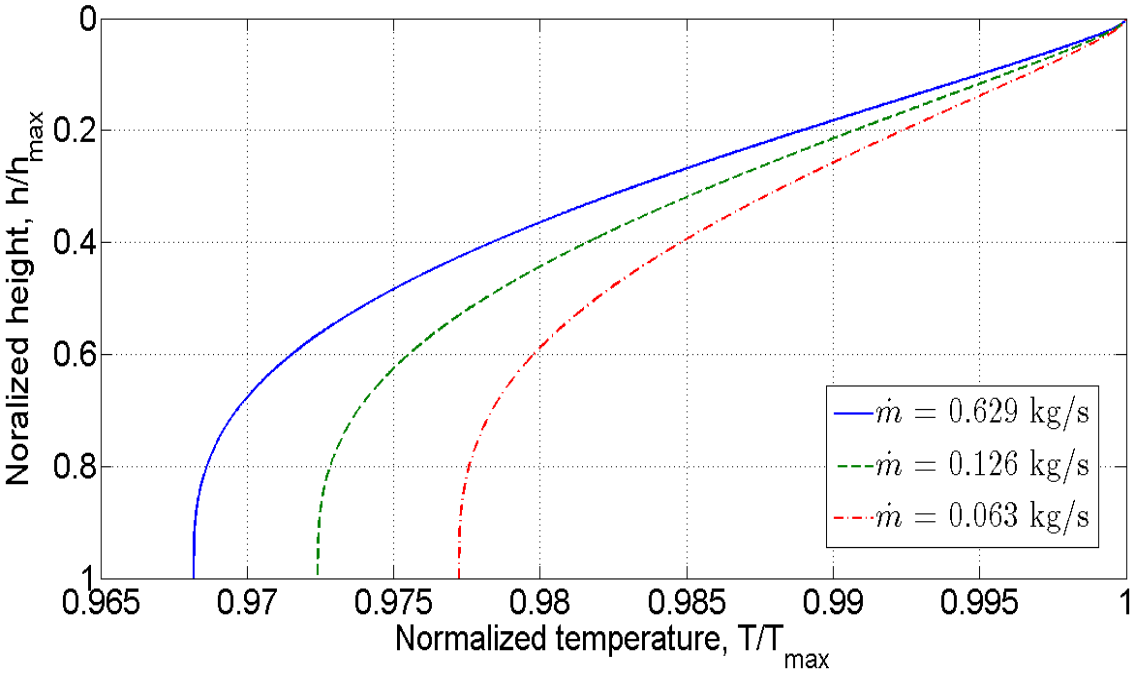

Figure 34: Normalized outlet temperature profiles for different inlet mass flow rates.

5.5.2 Impact of inlet temperature

It was observed that efficiency declined linearly with increase in inlet temperature above ambient temperature. This was illustrated in Figure 35 in which inlet temperature was normalized against incident radiation flux, G. This decrease in efficiency was attributed to an increase in convective heat loss as the inlet temperature was increased since there was a consequent increase in the mean top wall temperature. These results were in agreement with previous findings in literature (Tyagi, Phelan et al. 2009).

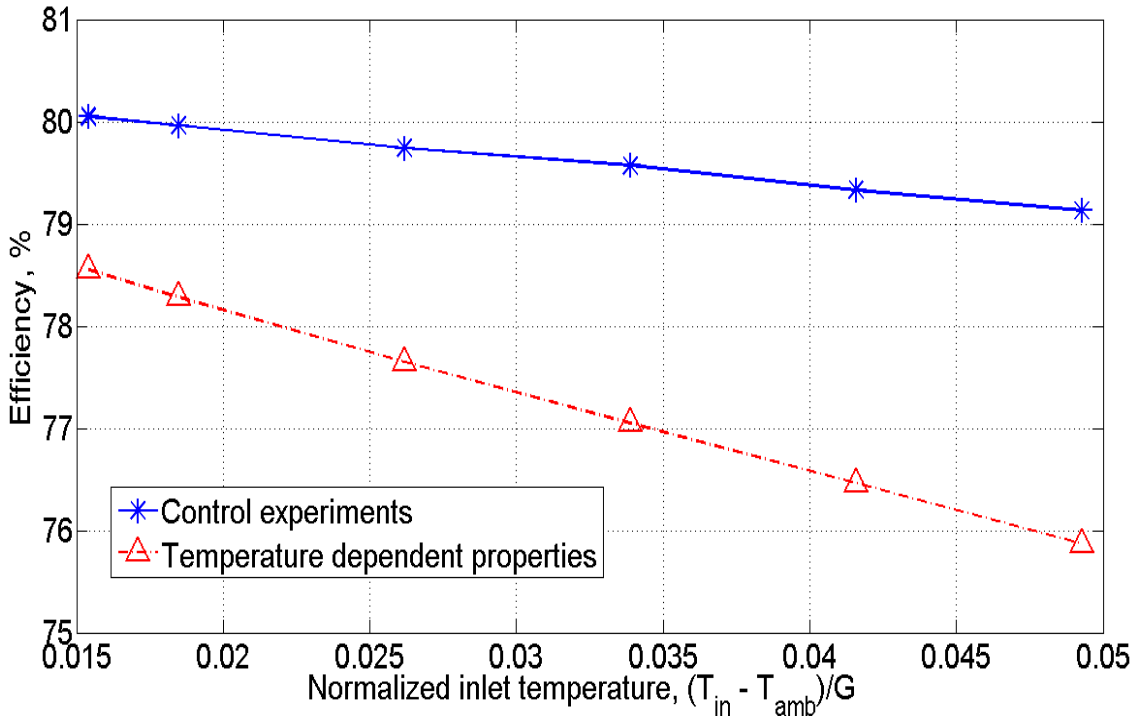

Figure 35: Efficiency as a function of normalized inlet temperature for control cases versus cases with properties varying including conductivity evaluated according to the improved Koo & Kleinstreuer correlation. Concentration ratio, $C = 100$.

It was also observed from the figure above that efficiency declined at a faster rate for cases with temperature dependent thermophysical properties. This was reasoned to be due to the presence of accelerated flow in the latter cases. As previously reported, the presence of accelerated flow resulted in decreasing efficiency. This compounded an already decreasing efficiency caused by increasing inlet temperatures.

5.5.3 Impact of bottom wall emissivity

It was observed that bottom wall emissivity had no impact on efficiency as illustrated in Figure 36. This was deemed to be due to the limited temperature and wavelength ranges of the study. At the temperatures considered, black body emission was seen to peak at long wavelengths ($\approx 10\ \mu m$) which were not considered.

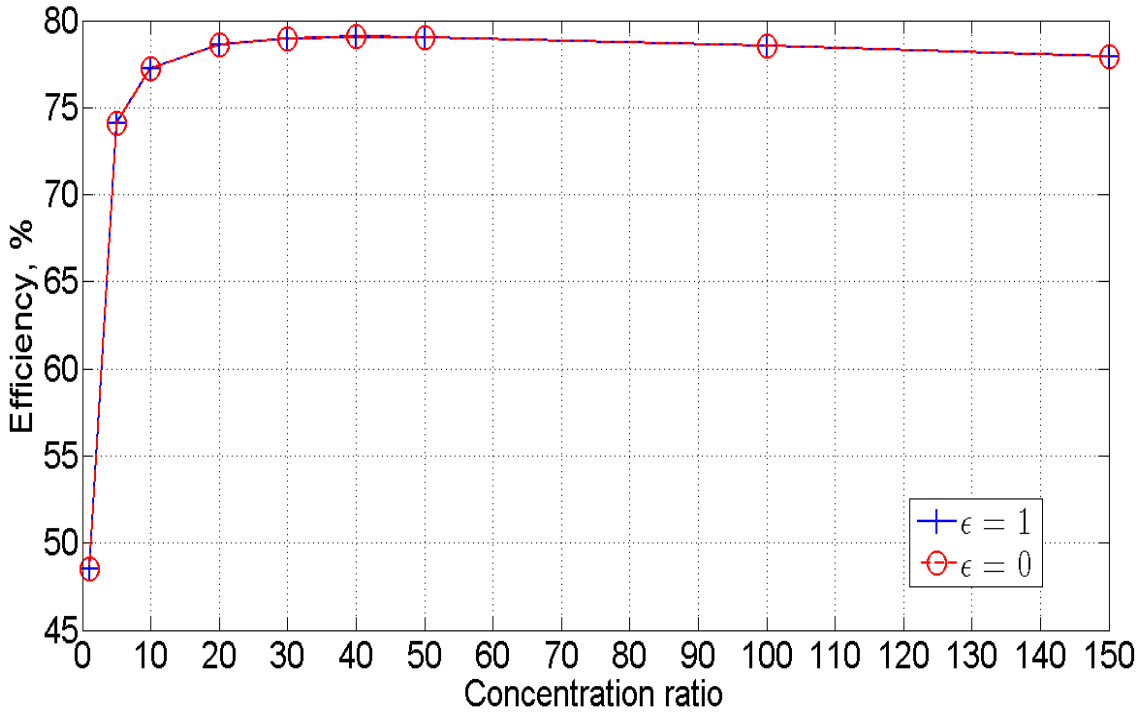

Figure 36: Receiver efficiencies for cases with transparent ($\epsilon = 0$) and perfect absorber ($\epsilon = 1$) bottom boundary conditions. All properties varying with conductivity evaluated according to the improved Koo & Kleinstreuer correlation.

Chapter 6: Conclusion

The objective of this study was to investigate the impact of enhanced thermophysical properties on the performance of a nanofluid-based solar volumetric flow receiver. In particular, focus was on the impact of temperature dependent conductivity and volumetric specific heat capacity. This was done by means of numerically modelling the receiver via the finite volume method and incorporating appropriate nanofluid property models for density, specific heat capacity and conductivity.

Obtaining the necessary models proved to be a challenge given that nanofluids have been characterised for either their radiative properties or their thermophysical properties, but not both. Furthermore, temperature dependence has largely not been studied and where such studies have been performed, limited temperature ranges have been considered. Copper oxide – water nanofluid provided a good candidate for study. However, its models were limited to a wavelength range $0.3 \leq \lambda \leq 1\ \mu m$ and a temperature range $308 \leq T < 380\ K$.

Results obtained were seen to be agreeable with a recent important study. Enhanced conductivity was seen to have an insignificant impact on the receiver's efficiency for the fixed geometry considered. This was because enhanced conductivity simply resulted in better diffusion of the energy absorbed, and efficiency was a measure of this absorbed energy. It was noted that these results, though agreeable, had been derived for different fluids with different thermal responses, namely, copper oxide – water nanofluid whose conductivity increased with increasing temperature, and Therminol VP1 whose conductivity decreased.

The results went further to illustrate the impact of conductivity on temperature development within the receiver for the fixed geometry considered. Enhanced conductivity resulted in the lowering of peak and mean top wall temperatures with maximum differences reported of $7.67\ K$ and $5.22\ K$ respectively. These were between the control case and the case with the improved Koo & Kleinstreuer correlation, both at a concentration ratio of 150. Temperature gradients along the height of the receiver were also seen to be smoother. These results were seen to be significant at higher temperatures. Consequently, consideration of the same would be necessary in the design of high flux receivers that achieve greater temperatures and require geometry optimisation.

The choice of conductivity model was seen to influence the magnitude of the results, though the qualitative aspect remained. The conservative Maxwell model with its approximately 3% enhancement in conductivity was seen to give results similar to the control cases. This was

unlike the non-conservative improved Koo & Kleinstreuer correlation that predicted enhancements as high as 27%. This served to establish the qualitative trend but also illustrated a common difficulty encountered in the study of nanofluids where characterisation data does not always agree. As such, the results could not be generalised for nanofluid-based receivers but were rather viewed as a baseline with a recommendation for case-by-case studies.

Volumetric specific heat capacity was observed to change very slightly, a maximum of 3% at a concentration ratio of 150. Consequently, the impact on both efficiency and temperature development was seen to be minimal. However, the presence of changing density and consequent flow acceleration through the receiver was seen to result in a clearly defined optimum concentration ratio. Beyond this point efficiency decreased with increase in concentration ratio, an observation not captured by the control cases. This was seen to be more of a modelling issue (assumptions employed) than it was due to the use of nanofluids with enhanced properties.

A parametric study performed illustrated that results obtained were agreeable with those reported in literature. An increase in mass flow rate was seen to result in lower residence time for temperature development in the fluid hence lower receiver temperatures. A positive consequence of this was reduced convective heat loss from the top wall and hence higher efficiencies. The opposite was observed for lower mass flow rates.

An increase in inlet temperature was seen to result in a linear decrease in efficiency. This was also linked to an increase in convective heat loss from the top. A study on the impact of the bottom wall emissivity, however, showed no difference in results. This was observed to be due to the limited wavelength and temperature ranges considered.

Various open questions remain, for example, the impact of the temperature dependent viscosity of copper oxide – water nanofluid. Given that a few correlations have been put forward in literature for this property, it is recommended that a similar study be done with viscosity as the objective. From a practical standpoint, such a study would be necessary given that the viscosity of a nanofluid, which is typically higher than the basefluid's, contributes to a need for higher pumping power to circulate the nanofluid.

More generally, it is also recommended that such studies be performed for other nanofluids. In particular, there is a need to examine graphite – water nanofluid which has been previously studied for use in solar thermal harvesting. This would require that its thermophysical properties be firstly characterised.

References

ABDELRAHMAN, M., FUMEAUX, P. and SUTER, P., 1979. Study of solid-gas-suspensions used for direct absorption of concentrated solar radiation. *Solar Energy,* **22**(1), pp. 45-48.

AHRENS, J., GEVECI, B. and LAW, C., 2005. ParaView: An End-User Tool for Large-Data Visualization. In: C.D. HANSEN and C.R. JOHNSON, eds, *The Visualization Handbook.* USA: Academic Press, pp. 717-731.

ANDERSON, J.V., SHORT, W., WENDELIN, T. and WEAVER, N., 1987. *Direct absorption receiver (DAR) systems assessment.* Solar Energy Research Inst., Golden, CO (USA).

ARAI, N., ITAYA, Y. and HASATANI, M., 1984. Development of a "volume heat-trap" type solar collector using a fine-particle semitransparent liquid suspension (FPSS) as a heat vehicle and heat storage medium Unsteady, one-dimensional heat transfer in a horizontal FPSS layer heated by thermal radiation. *Solar Energy,* **32**(1), pp. 49-56.

ASTM, 2012. *Standard Tables for Reference Solar Spectral Irradiances: Direct Normal and Hemispherical on 37° Tilted Surface.* ASTM G173-03. West Conshohocken, PA: ASTM International.

BARBÉS, B., PÁRAMO, R., BLANCO, E. and CASANOVA, C., 2014. Thermal conductivity and specific heat capacity measurements of CuO nanofluids. *Journal of Thermal Analysis and Calorimetry,* **115**(2), pp. 1883-1891.

BERTOCCHI, R., KARNI, J. and KRIBUS, A., 2004. Experimental evaluation of a non-isothermal high temperature solar particle receiver. *Energy,* **29**(5–6), pp. 687-700.

BOHN, M.S., GREEN, H.J., YEAGLE, G., SIEBARTH, J., ASBELL, O.D. and BROWN, C.T., 1986a. *Direct absorption receiver experiments and concept feasibility.* Solar Energy Research Inst., Golden, CO (USA); Georgia Inst. of Tech., Atlanta (USA). Research Inst.

BOHN, M.S. and WANG, K.Y., 1986b. *Experiments and analysis on the molten-salt direct-contact absorption receiver concept.* Solar Energy Research Inst., Golden, CO (USA).

BREWSTER, M.Q., 1992. *Thermal radiative transfer and properties.* USA: John Wiley & Sons Inc.

CHOI, S.U.S., 1995. Enhancing thermal conductivity of fluids with nanoparticles. *ASME-Publications-Fed,* **231**, pp. 99-106.

DARWISH, M.S., 1993. A new high-resolution scheme based on the normalized variable formulation. *Numerical Heat Transfer, Part B Fundamentals,* **24**(3), pp. 353-371.

DUFFIE, J.A. and BECKMAN, W.A., 2013. *Solar engineering of thermal processes.* 4th edn. USA: Wiley.

EASTMAN, J.A., CHOI, S.U.S., LI, S., YU, W. and THOMPSON, L.J., 2001. Anomalously increased effective thermal conductivities of ethylene glycol-based nanofluids containing copper nanoparticles. *Applied Physics Letters,* **78**(6), pp. 718-720.

EASTMAN, J.A., PHILLPOT, S.R., CHOI, S.U.S. and KEBLINSKI, P., 2004. Thermal transport in nanofluids. *Annual Review of Materials Research,* **34**, pp. 219-246.

FAIZAL, M., SAIDUR, R. and MEKHILEF, S., 2013. Potential of size reduction of flat-plate solar collectors when applying MWCNT nanofluid, *IOP Conference Series: Earth and Environmental Science* 2013, IOP Publishing, pp. 012004.

GUENNEBAUD, G. and JACOB, B., 2010. *Eigen v3.* http://eigen.tuxfamily.org/.

HADDAD, Z., ABID, C., OZTOP, H.F. and MATAOUI, A., 2014. A review on how the researchers prepare their nanofluids. *International Journal of Thermal Sciences,* **76**(0), pp. 168-189.

HALE, G.M. and QUERRY, M.R., 1973. Optical constants of water in the 200 nm to 200 μm wavelength region. *Applied Optics,* **12**(3), pp. 555-563.

HE, Q., WANG, S., TONG, M. and LIU, Y., 2012. Experimental study on thermophysical properties of nanofluids as phase-change material (PCM) in low temperature cool storage. *Energy Conversion and Management,* **64**, pp. 199-205.

HORDY, N., RABILLOUD, D., MEUNIER, J. and COULOMBE , S., 2014. High temperature and long-term stability of carbon nanotube nanofluids for direct absorption solar thermal collectors. *Solar Energy,* **105**(0), pp. 82-90.

HULST, H.C. and VAN DE HULST, H.C., 1957. *Light scattering by small particles.* New York, USA: John Wiley & Sons Inc.

HUNT, A.J., 1978. *Small particle heat exchangers.* California Univ., Berkeley (USA). Lawrence Berkeley Lab.

JAVADI, F.S., SAIDUR, R. and KAMALISARVESTANI, M., 2013. Investigating performance improvement of solar collectors by using nanofluids. *Renewable and Sustainable Energy Reviews,* **28**(0), pp. 232-245.

KALOGIROU, S.A., 2004. Solar thermal collectors and applications. *Progress in Energy and Combustion Science,* **30**(3), pp. 231-295.

KALURI, R.S., DATTARAJAN, S. and GANAPATHISUBBU, S., 2012. Numerical Simulations of Direct Absorption of Solar Radiation by a Liquid, *ASES Proc. World Renewable Energy Forum, Denver, Paper* 2012, pp. 1-8.

KALURI, R.S., VIJAYARAGHAVAN, S. and GANAPATHISUBBU, S., 2015. Model Development and Performance Studies of a Concentrating Direct Absorption Solar Collector. *Journal of Solar Energy Engineering,* **137**(2), pp. 021005.

KARAMI, M., RAISEE, M. and DELFANI, S., 2014. Numerical Investigation of Nanofluid-based Solar Collectors. *IOP Conference Series: Materials Science and Engineering,* **64**(1), pp. 012044.

KASAEIAN, A.B., DAVIRAN, S., AZARIAN, R.D. and RASHIDI, A., 2015. Performance evaluation and nanofluid using capability study of a solar parabolic trough collector. *Energy Conversion and Management,* **89**(0), pp. 368-375.

KASAEIAN, A.B., ESHGHI, A.T. and SAMETI, M., 2015. A review on the applications of nanofluids in solar energy systems. *Renewable and Sustainable Energy Reviews,* **43**(0), pp. 584-598.

KHANAFER, K. and VAFAI, K., 2011. A critical synthesis of thermophysical characteristics of nanofluids. *International Journal of Heat and Mass Transfer,* **54**(19–20), pp. 4410-4428.

KHULLAR, V. and TYAGI, H., 2011. Enhancing Optical Efficiency of a Linear Parabolic Solar Collector through Nanofluids. *AIP Conference Proceedings,* **1391**(1), pp. 353-355.

KHULLAR, V., TYAGI, H., PHELAN, P.E., OTANICAR, T.P., SINGH, H. and TAYLOR, R.A., 2013. Solar Energy Harvesting Using Nanofluids-Based Concentrating Solar Collector. *Journal of Nanotechnology in Engineering and Medicine,* **3**(3), pp. 031003-031003.

KOO, J. and KLEINSTREUER, C., 2005. Laminar nanofluid flow in microheat-sinks. *International Journal of Heat and Mass Transfer,* **48**(13), pp. 2652-2661.

KOO, J. and KLEINSTREUER, C., 2004. A new thermal conductivity model for nanofluids. *Journal of Nanoparticle Research,* **6**(6), pp. 577-588.

KUMAR, S. and TIEN, C.L., 1990. Analysis of combined radiation and convection in a particulate-laden liquid film. *Journal of solar energy engineering,* **112**(4), pp. 293-300.

LADJEVARDI, S.M., ASNAGHI, A., IZADKHAST, P.S. and KASHANI, A.H., 2013. Applicability of graphite nanofluids in direct solar energy absorption. *Solar Energy,* **94**(0), pp. 327-334.

LENERT, A., 2010a. *Nanofluid-based receivers for high-temperature, high-flux direct solar collectors.* Masters thesis, Unpublished. Massachusetts Institute of Technology.

LENERT, A. and WANG, E.N., 2012. Optimization of nanofluid volumetric receivers for solar thermal energy conversion. *Solar Energy,* **86**(1), pp. 253-265.

LENERT, A., ZUNIGA, Y.S.P. and WANG, E.N., 2010b. Nanofluid-based absorbers for high temperature direct solar collectors, *14th International Heat Transfer Conference* 2010b, American Society of Mechanical Engineers, pp. 499-508.

LI, C.H. and PETERSON, G.P., 2006. Experimental investigation of temperature and volume fraction variations on the effective thermal conductivity of nanoparticle suspensions (nanofluids). *Journal of Applied Physics,* **99**(8), pp. 084314.

LOMASCOLO, M., COLANGELO, G., MILANESE, M. and DE RISI, A., 2015. Review of heat transfer in nanofluids: Conductive, convective and radiative experimental results. *Renewable and Sustainable Energy Reviews,* **43**(0), pp. 1182-1198.

MACDEVETTE, M., 2013. *Heat transfer analysis of nanofluids and phase change materials.* PhD thesis, Unpublished. Centre De Recerca Matematica.

MAHIAN, O., KIANIFAR, A., KALOGIROU, S.A., POP, I. and WONGWISES, S., 2013. A review of the applications of nanofluids in solar energy. *International Journal of Heat and Mass Transfer,* **57**(2), pp. 582-594.

MENGÜÇ, M.P. and VISKANTA, R., 1983. Comparison of radiative transfer approximations for a highly forward scattering planar medium. *Journal of Quantitative Spectroscopy and Radiative Transfer,* **29**(5), pp. 381-394.

MERCATELLI, L., SANI, E., GIANNINI, A., DI NINNI, P., MARTELLI, F. and ZACCANTI, G., 2012. Carbon nanohorn-based nanofluids: characterization of the spectral scattering albedo. *Nanoscale Research Letters,* **7**(1), pp. 1-5.

MERCATELLI, L., SANI, E., ZACCANTI, G., MARTELLI, F., DI NINNI, P., BARISON, S., PAGURA, C., AGRESTI, F. and JAFRANCESCO, D., 2011. Absorption and scattering properties of carbon nanohorn-based nanofluids for direct sunlight absorbers. *Nanoscale research letters,* **6**(1), pp. 1-9.

MILLER, F.J. and KOENIGSDORFF, R.W., 2000. Thermal modeling of a small-particle solar central receiver. *Journal of solar energy engineering,* **122**(1), pp. 23-29.

MINARDI, J.E. and CHUANG, H.N., 1975. Performance of a “black” liquid flat-plate solar collector. *Solar Energy,* **17**(3), pp. 179-183.

MINTSA, H.A., ROY, G., NGUYEN, C.T. and DOUCET, D., 2009. New temperature dependent thermal conductivity data for water-based nanofluids. *International Journal of Thermal Sciences,* **48**(2), pp. 363-371.

MURSHED, S.M.S., LEONG, K.C. and YANG, C., 2008. Investigations of thermal conductivity and viscosity of nanofluids. *International Journal of Thermal Sciences,* **47**(5), pp. 560-568.

MURSHED, S.M.S., LEONG, K.C. and YANG, C., 2005. Enhanced thermal conductivity of TiO2—water based nanofluids. *International Journal of Thermal Sciences,* **44**(4), pp. 367-373.

NGUYEN, C.T., DESGRANGES, F., ROY, G., GALANIS, N., MARÉ, T., BOUCHER, S. and ANGUE MINTSA, H., 2007. Temperature and particle-size dependent viscosity data for water-based nanofluids – Hysteresis phenomenon. *International Journal of Heat and Fluid Flow,* **28**(6), pp. 1492-1506.

O'HANLEY, H., BUONGIORNO, J., MCKRELL, T. and HU, L., 2012. Measurement and model validation of nanofluid specific heat capacity with differential scanning calorimetry. *Advances in Mechanical Engineering,* **4**, pp. 181079.

OPENMP ARCHITECTURE REVIEW BOARD, 2011. *OpenMP v3.1.* http://openmp.org/wp/.

OTANICAR, T.P., 2011a. Enhancing the heat transfer in energy systems from a volumetric approach, *ASME/JSME 2011 8th Thermal Engineering Joint Conference* 2011a, American Society of Mechanical Engineers, pp. T30074-T30074-6.

OTANICAR, T.P., PHELAN, P.E. and GOLDEN, J.S., 2009b. Optical properties of liquids for direct absorption solar thermal energy systems. *Solar Energy,* **83**(7), pp. 969-977.

OTANICAR, T.P., PHELAN, P.E., PRASHER, R.S., ROSENGARTEN, G. and TAYLOR, R.A., 2010a. Nanofluid-based direct absorption solar collector. *Journal of Renewable and Sustainable Energy,* **2**(3), pp. 033102.

OTANICAR, T.P., PHELAN, P.E., ROSENGARTEN, G. and PRASHER, R., 2009a. Experimental testing and modeling of a micro solar thermal collector with direct absorption nanofluids, *Proceedings of the Inaugural US-EU-China Thermophysics Conference* 2009a, pp. 371-380.

OTANICAR, T.P., PHELAN, P.E., TAYLOR, R.A. and TYAGI, H., 2011. Spatially Varying Extinction Coefficient for Direct Absorption Solar Thermal Collector Optimization. *Journal of Solar Energy Engineering,* **133**(2), pp. 024501-024501.

OTANICAR, T.P., PHELAN, P.E., TAYLOR, R.A. and TYAGI, H., 2010b. Tuning the extinction coefficient for direct absorption solar thermal collector optimization, *ASME 2010 4th International Conference on Energy Sustainability* 2010b, American Society of Mechanical Engineers, pp. 819-824.

OTANICAR, T.P., TAYLOR, R.A., PHELAN, P.E. and PRASHER, R.S., 2009c. Impact of size and scattering mode on the optimal solar absorbing nanofluid, *ASME 2009 3rd International Conference on Energy Sustainability collocated with the Heat Transfer and InterPACK09 Conferences* 2009c, American Society of Mechanical Engineers, pp. 791-796.

OZISIK, M.N., 1973. *Radiative transfer and interactions with conduction and convection.* USA: John Wiley & Sons Inc.

PAK, B.C. and CHO, Y.I., 1998. Hydrodynamic and heat transfer study of dispersed fluids with submicron metallic oxide particles. *Experimental Heat Transfer an International Journal,* **11**(2), pp. 151-170.

PALIK, E.D., 1998. *Handbook of optical constants of solids.* USA: Academic Press.

PANTZALI, M.N., KANARIS, A.G., ANTONIADIS, K.D., MOUZA, A.A. and PARAS, S.V., 2009. Effect of nanofluids on the performance of a miniature plate heat exchanger with modulated surface. *International Journal of Heat and Fluid Flow,* **30**(4), pp. 691-699.

PHILIP, J. and SHIMA, P.D., 2012. Thermal properties of nanofluids. *Advances in Colloid and Interface Science,* **183–184**(0), pp. 30-45.

POPIEL, C.O. and WOJTKOWIAK, J., 1998. Simple formulas for thermophysical properties of liquid water for heat transfer calculations (from 0 C to 150 C). *Heat Transfer Engineering,* **19**(3), pp. 87-101.

SAID, Z., SAIDUR, R. and RAHIM, N.A., 2015. Corrigendum to “Optical properties of metal oxides based nanofluids” [Int Commun Heat Mass 59 (2014) 46–54]. *International Communications in Heat and Mass Transfer,* **62**, pp. 58-59.

SAID, Z., SAIDUR, R. and RAHIM, N.A., 2014. Optical properties of metal oxides based nanofluids. *International Communications in Heat and Mass Transfer,* **59**(0), pp. 46-54.

SAID, Z., SAJID, M.H., SAIDUR, R., KAMALISARVESTANI, M. and RAHIM, N.A., 2013. Radiative properties of nanofluids. *International Communications in Heat and Mass Transfer,* **46**(0), pp. 74-84.

SAJID, M.H., SAIDUR, R., MOHD SABRI, M.F., SAID, Z. and HASSANI, S., 2015. Spotlight on available optical properties and models of nanofluids: A review. *Renewable and Sustainable Energy Reviews,* **43**(0), pp. 750-762.

SANI, E., BARISON, S., PAGURA, C., MERCATELLI, L., SANSONI, P., FONTANI, D., JAFRANCESCO, D. and FRANCINI, F., 2010. Carbon nanohorns-based nanofluids as direct sunlight absorbers. *Optics express,* **18**(5), pp. 5179-5187.

SANI, E. and DELL’ORO, A., 2014. Optical constants of ethylene glycol over an extremely wide spectral range. *Optical Materials,* **37**(0), pp. 36-41.

SHAHRUL, I.M., MAHBUBUL, I.M., KHALEDUZZAMAN, S.S., SAIDUR, R. and SABRI, M.F.M., 2014. A comparative review on the specific heat of nanofluids for energy perspective. *Renewable and Sustainable Energy Reviews,* **38**(0), pp. 88-98.

TAYLOR, R.A., OTANICAR, T.P. and ROSENGARTEN, G., 2012. Nanofluid-based optical filter optimization for PV/T systems. *Light: Science & Applications,* **1**(10), pp. 34.

TAYLOR, R.A., PHELAN, P.E., ADRIAN, R.J., GUNAWAN, A. and OTANICAR, T.P., 2012. Characterization of light-induced, volumetric steam generation in nanofluids. *International Journal of Thermal Sciences,* **56**(0), pp. 1-11.

TAYLOR, R.A., PHELAN, P.E., OTANICAR, T.P., ADRIAN, R. and PRASHER, R., 2011b. Nanofluid optical property characterization: towards efficient direct absorption solar collectors. *Nanoscale Research Letters,* **6**(1), pp. 1-11.

TAYLOR, R.A., PHELAN, P.E., OTANICAR, T.P., TYAGI, H. and TRIMBLE, S., 2010. Applicability of nanofluids in concentrated solar energy harvesting, *ASME 2010 4th International Conference on Energy Sustainability* 2010, American Society of Mechanical Engineers, pp. 825-832.

TAYLOR, R.A., PHELAN, P.E., OTANICAR, T.P., WALKER, C.A., NGUYEN, M., TRIMBLE, S. and PRASHER, R.S., 2011a. Applicability of nanofluids in high flux solar collectors. *Journal of Renewable and Sustainable Energy,* **3**(2), pp. 023104.

THIRUGNANASAMBANDAM, M., INIYAN, S. and GOIC, R., 2010. A review of solar thermal technologies. *Renewable and Sustainable Energy Reviews,* **14**(1), pp. 312-322.

TIEN, C.L., 1988. Thermal radiation in packed and fluidized beds. *ASME J.Heat Transfer,* **110**(4), pp. 1230-1242.

TIWARI, A.K., GHOSH, P. and SARKAR, J., 2013. Solar water heating using nanofluids-a comprehensive overview and environmental impact analysis. *Int J Emerg Technol Adv Eng,* **3**(3), pp. 221-224.

TYAGI, H., PHELAN, P.E. and PRASHER, R.S., 2009. Predicted efficiency of a low-temperature nanofluid-based direct absorption solar collector. *Journal of solar energy engineering,* **131**(4), pp. 041004.

VAJJHA, R.S. and DAS, D.K., 2012. A review and analysis on influence of temperature and concentration of nanofluids on thermophysical properties, heat transfer and pumping power. *International Journal of Heat and Mass Transfer,* **55**(15–16), pp. 4063-4078.

VAJJHA, R.S. and DAS, D.K., 2009c. Experimental determination of thermal conductivity of three nanofluids and development of new correlations. *International Journal of Heat and Mass Transfer,* **52**(21–22), pp. 4675-4682.

VAJJHA, R.S., DAS, D.K. and MAHAGAONKAR, B.M., 2009a. Density measurement of different nanofluids and their comparison with theory. *Petroleum Science and Technology,* **27**(6), pp. 612-624.

VEERARAGAVAN, A., LENERT, A., YILBAS, B., AL-DINI, S. and WANG, E.N., 2012. Analytical model for the design of volumetric solar flow receivers. *International Journal of Heat and Mass Transfer,* **55**(4), pp. 556-564.

VERMA, S.K. and TIWARI, A.K., 2015. Progress of nanofluid application in solar collectors: A review. *Energy Conversion and Management,* **100**(0), pp. 324-346.

VERSTEEG, H.K. and MALALASEKERA, W., 2007. *An introduction to computational fluid dynamics: the finite volume method.* 2nd edn. UK: Pearson Education.

VIJAYARAGHAVAN, S., GANAPATHISUBBU, S. and SANTOSH KUMAR, C., 2013. Performance analysis of a spectrally selective concentrating direct absorption collector. *Solar Energy,* **97**(0), pp. 418-425.

VISKANTA, R., 1966. Radiation transfer and interaction of convection with radiation heat transfer. *Advances in Heat Transfer,* **3**, pp. 175-251.

VISKANTA, R. and TOOR, J.S., 1973. Effect of multiple scattering on radiant energy transfer in waters. *Journal of Geophysical Research,* **78**(18), pp. 3538-3551.

VISKANTA, R. and TOOR, J.S., 1972. Radiant energy transfer in waters. *Water Resources Research,* **8**(3), pp. 595-608.

WANG, X. and MUJUMDAR, A.S., 2007. Heat transfer characteristics of nanofluids: a review. *International Journal of Thermal Sciences,* **46**(1), pp. 1-19.

WU, J.M. and ZHAO, J., 2013. A review of nanofluid heat transfer and critical heat flux enhancement—Research gap to engineering application. *Progress in Nuclear Energy,* **66**(0), pp. 13-24.

WU, Y., ZHOU, L., DU, X. and YANG, Y., 2015. Optical and thermal radiative properties of plasmonic nanofluids containing core–shell composite nanoparticles for efficient photothermal conversion. *International Journal of Heat and Mass Transfer,* **82**(0), pp. 545-554.

XUAN, Y. and ROETZEL, W., 2000. Conceptions for heat transfer correlation of nanofluids. *International Journal of Heat and Mass Transfer,* **43**(19), pp. 3701-3707.

YOUSEFI, T., VEISY, F., SHOJAEIZADEH, E. and ZINADINI, S., 2012b. An experimental investigation on the effect of MWCNT-H2O nanofluid on the efficiency of flat-plate solar collectors. *Experimental Thermal and Fluid Science,* **39**(0), pp. 207-212.

YOUSEFI, T., VEYSI, F., SHOJAEIZADEH, E. and ZINADINI, S., 2012. An experimental investigation on the effect of Al2O3–H2O nanofluid on the efficiency of flat-plate solar collectors. *Renewable Energy,* **39**(1), pp. 293-298.

YU, W. and XIE, H., 2012. A Review on Nanofluids: Preparation, Stability Mechanisms, and Applications. *J.Nanomaterials,* **2012**, pp. 1:1-1:17.

ZHOU, L.P., WANG, B.X., PENG, X.F., DU, X.Z. and YANG, Y.P., 2010. On the specific heat capacity of CuO nanofluid. *Advances in Mechanical Engineering,* **2**, pp. 172085.

ZHOU, S. and NI, R., 2008. Measurement of the specific heat capacity of water-based Al_2O_3 nanofluid. *Applied Physics Letters,* **92**(9), pp. 093123.

ZHU, Q., LI, Y., MU, L. and CUI, Y., 2010. Theoretical Investigation of Radiative Transport and Heat Transfer of Nanofluids in a Direct Solar Absorption Collector, *2010 14th International Heat Transfer Conference* 2010, American Society of Mechanical Engineers, pp. 877-882.

ZHU, Q. and ZHANG, Z.M., 2012. Radiative properties of micro/nanoscale particles in dispersions for photothermal energy conversion. In: W.J. MINKOWYCZ, E.M. SPARROW and J.P. ABRAHAM, eds, *Advances in Numerical Heat Transfer - Nanoparticle Heat Transfer and Fluid Flow.* CRC Press/Taylor & Francis, pp. 143-174.

Appendix

Appendix A: Details of validation case

Table 5: Specifications for validation case (Tyagi, Phelan et al. 2009).

Item	Value
Velocity (plug profile), u	1 m/s
Mass flow rate, $\dot{m}$	1.2 kg/s
Inlet temperature, T_{in}	308 K
Ambient temperature, T_{amb}	298K
Length, L	1 m
Width, W	1 m
Height, H	1.2 mm
Convective heat loss coefficient, h	6.43 W/(m^2 K)
Incident solar flux, G	1000 W/m^2
Glass transmissivity, τ	0.9
Bottom wall emissivity, ϵ	0
Density (ρ) – water at 25°C	997 kg/m^3
Density (ρ) – aluminium at 25°C	2700 kg/m^3
Specific heat capacity (c_p) – water at 25°C	4180 J/(kg K)
Specific heat capacity (c_p) – aluminium at 25°C	900 J/(kg K)
Thermal conductivity (k) – water at 25°C	0.607 W/(m K)
Thermal conductivity (k) – aluminium at 25°C	247 W/(m K)

Thermophysical properties of the nanofluid were taken by applying the parallel mixture rule (equation (3.12)) for density, the thermal equilibrium model (equation (3.15)) for specific heat capacity and the Maxwell model (equation (3.17)) for conductivity. These properties were taken as temperature independent and computed from the values provided in the table above.

Optical properties were obtained from (Brewster 1992) and modelled using the MATLAB® "pchip" function. Radiative properties were obtained using the Rayleigh scattering model. The top incident flux was given by approximating the sun as a blackbody emitter at temperature of 5800K and applying the Planck's blackbody relation.

Appendix B: Faculty Assessment of Ethics form

EBE Faculty: Assessment of Ethics in Research Projects

Any person planning to undertake research in the Faculty of Engineering and the Built Environment at the University of Cape Town is required to complete this form before collecting or analysing data. When completed it should be submitted to the supervisor (where applicable) and from there to the Head of Department. If any of the questions below have been answered YES, and the applicant is NOT a fourth year student, the Head should forward this form for approval by the Faculty EIR committee: submit to Ms Zulpha Geyer (Zulpha.Geyer@uct.ac.za; Chem Eng Building, Ph 021 650 4791). Students must include a copy of the completed form with the thesis when it is submitted for examination.

Name of Principal Researcher/Student: GODFREY KABUNGO GAKINGO

Department: MECHANICAL ENGINEERING

If a Student: Degree: MPHIL IN MECHANICAL ENG.

Supervisor: PROF DAYA REDDY

If a Research Contract indicate source of funding/sponsorship:

Research Project Title: APPLICATION OF FEM TO SOLAR ENERGY

Overview of ethics issues in your research project:

Question 1: Is there a possibility that your research could cause harm to a third party (i.e. a person not involved in your project)?	YES	NO ✓
Question 2: Is your research making use of human subjects as sources of data? If your answer is YES, please complete Addendum 2.	YES	NO ✓
Question 3: Does your research involve the participation of or provision of services to communities? If your answer is YES, please complete Addendum 3.	YES	NO ✓
Question 4: If your research is sponsored, is there any potential for conflicts of interest? If your answer is YES, please complete Addendum 4.	YES	NO ✓

If you have answered YES to any of the above questions, please append a copy of your research proposal, as well as any interview schedules or questionnaires (Addendum 1) and please complete further addenda as appropriate.

I hereby undertake to carry out my research in such a way that

- there is no apparent legal objection to the nature or the method of research; and
- the research will not compromise staff or students or the other responsibilities of the University;
- the stated objective will be achieved, and the findings will have a high degree of validity;
- limitations and alternative interpretations will be considered;
- the findings could be subject to peer review and publicly available; and
- I will comply with the conventions of copyright and avoid any practice that would constitute plagiarism.

Signed by:

	Full name and signature	Date
Principal Researcher/Student:	GODFREY KABUNGO Signed by candidate	29/01/2015

This application is approved by:

Supervisor (if applicable):	Signed by candidate	30/1/15
HOD (or delegated nominee): Final authority for all assessments with NO to all questions and for all undergraduate research.	Signed by candidate	06/02/2015
Chair : Faculty EIR Committee For applicants other than undergraduate students who have answered YES to any of the above questions.		

ADDENDUM 1:
Please append a copy of the research proposal here, as well as any interview schedules or questionnaires:

ADDENDUM 2: To be completed if you answered YES to Question 2:

It is assumed that you have read the UCT Code for Research involving Human Subjects (available at http://web.uct.ac.za/depts/educate/download/uctcodeforresearchinvolvinghumansubjects.pdf) in order to be able to answer the questions in this addendum.

2.1 Does the research discriminate against participation by individuals, or differentiate between participants, on the grounds of gender, race or ethnic group, age range, religion, income, handicap, illness or any similar classification?	YES	NO
2.2 Does the research require the participation of socially or physically vulnerable people (children, aged, disabled, etc) or legally restricted groups?	YES	NO
2.3 Will you not be able to secure the informed consent of all participants in the research? (In the case of children, will you not be able to obtain the consent of their guardians or parents?)	YES	NO
2.4 Will any confidential data be collected or will identifiable records of individuals be kept?	YES	NO
2.5 In reporting on this research is there any possibility that you will not be able to keep the identities of the individuals involved anonymous?	YES	NO
2.6 Are there any foreseeable risks of physical, psychological or social harm to participants that might occur in the course of the research?	YES	NO
2.7 Does the research include making payments or giving gifts to any participants?	YES	NO

If you have answered YES to any of these questions, please describe how you plan to address these issues (append to form):

ADDENDUM 3: To be completed if you answered YES to Question 3:

3.1 Is the community expected to make decisions for, during or based on the research?	YES	NO
3.2 At the end of the research will any economic or social process be terminated or left unsupported, or equipment or facilities used in the research be recovered from the participants or community?	YES	NO
3.3 Will any service be provided at a level below the generally accepted standards?	YES	NO

If you have answered YES to any of these questions, please describe how you plan to address these issues (append to form)

ADDENDUM 4: To be completed if you answered YES to Question 4

4.1 Is there any existing or potential conflict of interest between a research sponsor, academic supervisor, other researchers or participants?	YES	NO
4.2 Will information that reveals the identity of participants be supplied to a research sponsor, other than with the permission of the individuals?	YES	NO
4.3 Does the proposed research potentially conflict with the research of any other individual or group within the University?	YES	NO

If you have answered YES to any of these questions, please describe how you plan to address these issues(append to form)